NASA/CR–2017–219583

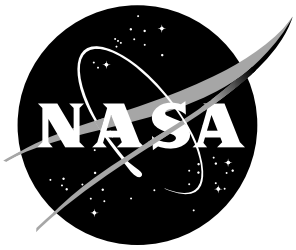

Diagnostic Techniques to Elucidate the Aerodynamic Performance of Acoustic Liners

Jason June
University of Florida, Gainesville, Florida

Brandon Bertolucci
University of Florida, Gainesville, Florida *

Lawrence Ukeiley
University of Florida, Gainesville, Florida

Louis N. Cattafesta, III
University of Florida, Gainesville, Florida †

Mark Sheplak
University of Florida, Gainesville, Florida

July 2017

*Currently at Boeing Commercial Airplane Group, Seattle, Washington
†Currently at Florida State University, Tallahassee, Florida

NASA STI Program. . . in Profile

Since its founding, NASA has been dedicated to the advancement of aeronautics and space science. The NASA scientific and technical information (STI) program plays a key part in helping NASA maintain this important role.

The NASA STI Program operates under the auspices of the Agency Chief Information Officer. It collects, organizes, provides for archiving, and disseminates NASA's STI. The NASA STI Program provides access to the NASA Aeronautics and Space Database and its public interface, the NASA Technical Report Server, thus providing one of the largest collection of aeronautical and space science STI in the world. Results are published in both non-NASA channels and by NASA in the NASA STI Report Series, which includes the following report types:

- TECHNICAL PUBLICATION. Reports of completed research or a major significant phase of research that present the results of NASA programs and include extensive data or theoretical analysis. Includes compilations of significant scientific and technical data and information deemed to be of continuing reference value. NASA counterpart of peer-reviewed formal professional papers, but having less stringent limitations on manuscript length and extent of graphic presentations.
- TECHNICAL MEMORANDUM. Scientific and technical findings that are preliminary or of specialized interest, e.g., quick release reports, working papers, and bibliographies that contain minimal annotation. Does not contain extensive analysis.
- CONTRACTOR REPORT. Scientific and technical findings by NASA-sponsored contractors and grantees.
- CONFERENCE PUBLICATION. Collected papers from scientific and technical conferences, symposia, seminars, or other meetings sponsored or co-sponsored by NASA.
- SPECIAL PUBLICATION. Scientific, technical, or historical information from NASA programs, projects, and missions, often concerned with subjects having substantial public interest.
- TECHNICAL TRANSLATION. English-language translations of foreign scientific and technical material pertinent to NASA's mission.

Specialized services also include organizing and publishing research results, distributing specialized research announcements and feeds, providing information desk and personal search support, and enabling data exchange services.

For more information about the NASA STI Program, see the following:

- Access the NASA STI program home page at `http://www.sti.nasa.gov`
- E-mail your question to `help@sti.nasa.gov`
- Phone the NASA STI Information Desk at 757-864-9658
- Write to:
  NASA STI Information Desk
  Mail Stop 148
  NASA Langley Research Center
  Hampton, VA 23681-2199

NASA/CR–2017–219583

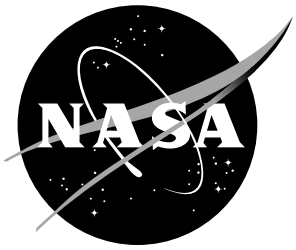

Diagnostic Techniques to Elucidate the Aerodynamic Performance of Acoustic Liners

Jason June
University of Florida, Gainesville, Florida

Brandon Bertolucci
University of Florida, Gainesville, Florida [‡]

Lawrence Ukeiley
University of Florida, Gainesville, Florida

Louis N. Cattafesta, III
University of Florida, Gainesville, Florida [§]

Mark Sheplak
University of Florida, Gainesville, Florida

National Aeronautics and
Space Administration

Langley Research Center
Hampton, Virginia 23681-2199

July 2017

[‡]Currently at Boeing Commercial Airplane Group, Seattle, Washington
[§]Currently at Florida State University, Tallahassee, Florida

Available from:

NASA STI Program / Mail Stop 148
NASA Langley Research Center
Hampton, VA 23681-2199
Fax: 757-864-6500

Abstract

In support of Topic A.2.8 of NASA NRA NNH10ZEA001N, the University of Florida (UF) has investigated the use of flow field optical diagnostic and micromachined sensor-based techniques for assessing the wall shear stress on an acoustic liner. Stereoscopic particle image velocimetry (sPIV) was used to study the velocity field over a liner in the Grazing Flow Impedance Duct (GFID). The results indicate that the use of a control volume based method to determine the wall shear stress is prone to significant error. The skin friction over the liner as measured using velocity curve fitting techniques was shown to be locally reduced behind an orifice, relative to the hard wall case in a streamwise plane centered on the orifice. The capacitive wall shear stress sensor exhibited a linear response for a range of shear stresses over a hard wall. PIV over the liner is consistent with lifting of the near wall turbulent structure as it passes over an orifice, followed by a region of low wall shear stress.

Contents

1 Introduction

Interest in measuring the fluid dynamic impact of acoustic liners has grown over the past several years, especially regarding the contribution of the lined walls on the drag penalty. In an effort to enhance the understanding of the physics of grazing flow over an acoustic liner, the grazing flow impedance duct (GFID), has been built at the University of Florida. The GFID reuses several components of the grazing incidence tube, which was donated to the University of Florida from NASA Langley Research Center. This facility has been redesigned to investigate both the acoustic characteristics of acoustic liners and their influence on the flow field. The following section will first provide a stated list of objectives, and then will introduce the topic of wall shear stress measurement within internal flows, along with the diagnostic techniques used to measure the wall shear stress.

1.1 NRA Milestones

The focus of this work is to develop techniques to determine the wall shear stress on the face of an acoustic liner. This is accomplished through two approaches. A capacitive wall shear stress sensor (CWSSS) is used to provide ac and dc shear stress information at a point stress over an area. Comparison of the values gathered using the CWSSS to those obtained through curve-fit velocity profiles provide a link to a classically used technique.

The milestones of the initially proposed research were written as a way to establish the scope of the research as well as provide target goals for successful resolution of the work. These milestones are presented in Table 1, along with the sections associated with the completion of each milestone. This research has led to successful alteration of the GFID in order to accommodate both acoustic impedance testing and measurement of the velocity field through optical means. Also, the CWSSS technique was matured through improvements in packaging, and benchtop calibration. Measurements in the GFID were then taken using a CWSSS in both a baseline hard wall configuration and embedded in a single degree of freedom acoustic liner with a perforate face sheet. Lastly, extensive particle image velocimetry (PIV) measurements have been taken in order to highlight some of the interesting near wall physics of flow over an acoustic liner. The only milestone that has not been completed successfully is the expansion of the facility capabilities to be able to produce 160 dB sound pressure level (SPL) acoustic excitation. However, the limits of a recently added acoustic driver section have not been tested extensively, and should constitute an improvement over the current limit of 140 dB SPL at a bulk Mach number of 0.3.

Table 1: Milestones.

Task	Milestone	Metrics	Section
Finalize construction of liner flow facility	Contract construction of the near-anechoic termination for decreased reflection coefficient	Minimum flow speed of $M_b = 0.4$ and 140 dB SPL with microphone array and velocity measurement capabilities	2
Baseline flow characterization	Measure the three dimensional velocity flow field for accurate assessment of flow physics including secondary flow pattern and core velocity profiles	Comparison to published work for high Reynolds number channel flow studies. Comparable flow profiles, turbulence levels, and flow speeds	4
Baseline drag penalty and shear stress of perforate liner via indirect velocity profiles	Measure velocity of near wall region prior to, over and downstream of liner for indirect assessment of shear stress induced by benchmark liner installation via 3D LDV velocity profile measurements	Inference of local shear stress via high resolution curve fitting	7
Baseline perforate liner acoustic benchmark testing	Perform baseline acoustic liner impedance eduction over prescribed range of SPL and frequency values to first facility acoustic mode cut-on; compare with published work	Direct comparison of impedance values vs. benchmark perforate liner as function of Mach number, drive frequency, and SPL	5.2
MEMS capacitive shear stress packaging	Small, robust capacitive shear stress sensor plug with on-board mod/de-mod switching for dynamic shear stress measurements	dc to 5 kHz bandwidth, 80 dB dynamic range, pressure rejection, low EMI	3.4.1
MEMS capacitive sensor benchtop characterization	Quantitative, repeatable static and dynamic shear stess measurements in laminar flow cell and acoustic plane wave tube	Direct comparison to exact solution for laminar mean and dynamic flows	3.4.2
MEMS capacitive GFID installation and characterization	Plug mounted, adjacent to resonant liner orifice	Real-time shear stress values compared to indirect velocity profiles	7.2
Facility capability expansion (increase SPL test range)		Increase SPL capabilities to 160 dB	–

Table 1 – continued from previous page.

Task	Milestone	Metrics	Section
Phase-locked, near-orifice resonant liner 3-D velocity measurements (LDV and PIV)	Near orifice 3D velocity measurements to assess velocity and vorticity of flow into and out of resonant liner	Provide phase-locked 3D velocity contours of near orifice physics	6
MEMS capacitive shear stress sensor testing with resonant liner	Real-time shear stress values with high spatial resolution in small, robust plug design	Real-time shear stress values in presence of resonant liner	7.3
Transfer of techniques/technology to NASA	Comparison of shear stress techniques and technologies provided for use in NASA GFIT and CDTR liner flow facilities		All

1.2 Evaluation of Friction Factor in a Duct

Before turning attention to the problem of assessing the skin friction over an acoustic liner, literature in reference to skin friction in a hard walled duct is discussed. The skin friction is known to be a function of the bulk Reynolds number,

$$Re_b = \frac{U_b D_h}{\nu},$$

which is based on the bulk velocity in the duct, U_b, and the hydraulic diameter [1],

$$D_h = \frac{4A}{P},$$

where A is the area of the duct, and P is the wetted perimeter. The skin friction is typically normalized by the dynamic pressure, and this is defined as the coefficient of friction. Alternatively the Darcy friction factor is used, which is four times the coefficient of friction

$$f_D = 4C_f = \frac{8\overline{\tau_w}}{\rho U_b^2} = \frac{8\overline{\tau_w}}{\gamma P_s M_b^2}.$$

The Prandtl equation [2] for the friction factor in a pipe is

$$\frac{1}{\sqrt{f_D}} = 2.0 \log_{10}\left(Re_b\sqrt{f_D}\right) - 0.8. \tag{1}$$

This result has been determined through integration of the log-law radially, as pipe flow does not exhibit a large wake region. Although pipe flow exhibits many differences from duct flow, such as the turbulence structure [3] as well as the presence of secondary flow, there has been interest in the applicability of pipe flow relationships

to the more complex flow in rectangular ducts. The notion of an equivalent Reynolds number for a duct is supported by noting that the integrated log-law profile in a channel flow is of the same algebraic form as the Prandtl equation. As the turbulent case of both types of internal flow has no exact solution that can be compared, relationships from laminar internal flow theory are used, in the hope that they will extend into the turbulent regime. With the above in mind, a brief review of laminar internal flow is given.

For a fully developed laminar or turbulent flow of arbitrary geometry, the perimeter averaged shear stress and axial pressure gradient are related by

$$\overline{\tau_w} = -\frac{D_h}{4}\frac{dp}{dz}. \tag{2}$$

The bulk velocity, which is the integrated average over the duct cross-section, can be derived for various duct geometries, as the Navier-Stokes equations can be solved exactly [1]. This allows for exact determination of the Darcy friction factor in terms of the Reynolds number. For a rectangular duct of height, h, and width w, the bulk velocity is

$$U_b = -\frac{h^2}{12\mu}\frac{dp}{dz}\left[1 - \frac{192h}{\pi^5 w}\sum_{n=1,3,5,\ldots}^{\infty}\frac{\tanh\left(\frac{n\pi w}{2h}\right)}{n^5}\right]. \tag{3}$$

With the definition of the duct aspect ratio $AR = {}^{w}/_{h}$, the Darcy friction factor is

$$f_D = \frac{96}{Re_b\, g(AR)}, \tag{4}$$

where $g(AR)$ is a multiplicative factor that is solely a function of the duct aspect ratio,

$$g(AR) = \left(\frac{AR+1}{AR}\right)^2\left[1 - \frac{192}{\pi AR}\sum_{n=1,3,5,\ldots}^{\infty}\frac{\tanh\left(\frac{n\pi AR}{2}\right)}{n^5}\right]. \tag{5}$$

In the channel flow limit where $AR \to \infty$, the aspect ratio function is unity and the Darcy friction factor has the appropriate value of $f_D = {}^{96}/_{Re_b}$. For a pipe, the Darcy friction factor over the laminar regime is $f_{D,p} = {}^{64}/_{Re_b}$ and modifying the Reynolds number of the duct flow to an equivalent pipe Reynolds number,

$$Re_{b,eq} = \frac{2g(AR)}{3}Re_b \tag{6}$$

allows for use of the equivalent duct Reynolds number in the known relationship for pipe flow. The modified Prandtl equation was first presented by Jones [4] as

$$\frac{1}{\sqrt{f_D}} = 2.0\log_{10}\left(\frac{2g(AR)}{3}Re_b\sqrt{f_D}\right) - 0.8. \tag{7}$$

Despite some of the more dubious assumptions of this curve fit, Jones states that the uncertainty in the fit is approximately five percent when compared to literature. Another assumption that is implicit in the Jones formula is that the log-law constants are the same for a pipe as they are for a channel or duct. However, while the

equivalent Reynolds number concept may be valid in a flow dominated by viscous effects, it would seem unlikely that it is truly capturing the relevant physics and nonlinear inertial effects that occur in a turbulent duct. Brundrett and Baines [5] showed that secondary flow was due to spatial gradients of the Reynolds stresses, which are not present in laminar flow. The secondary flow drives the transport of high momentum core flow into the corners and recirculation of low momentum fluid from the center of the wall toward the core flow. While channel flows still do not exhibit secondary flow, they are within the same family of flows as a square duct. Zanoun [6] suggests that values of $\kappa = 0.37$ and $B = 3.7$ should be used for channel flow, and the log-law integrated equation for the friction factor is

$$\frac{1}{\sqrt{f_D}} = 2.2 \log_{10}\left(g(AR) Re_b \sqrt{f_D}\right) - 1.9656, \tag{8}$$

where the laminar equivalent diameter is used, in an effort to extend the applicability to the square duct. In this case, as the equivalency was carried out between channel flow with a duct flow, the multiplicative two-thirds factor has been removed. Zanoun [7] also suggests a power-law fit that has been adjusted to allow for the laminar equivalent Reynolds number,

$$f_D = 0.3534\big(g(AR) Re_b\big)^{-0.25}. \tag{9}$$

The reliability of using the laminar equivalency is not without question, yet in the absence of a better correlation for square ducts, it will be used in comparison to the hard wall data obtained in this document.

1.3 Literature on Acoustic Liner Drag

The methods of determining the wall shear stress over a liner fall into four categories, momentum integral approaches in large scale wind tunnels [8–10], floating element drag balances [11–13], control volume approaches [14, 15], and boundary layer curve fits or Clauser charts [8].

Each method has uncertainties that make accurate measurement of the skin friction difficult. The momentum integral approach, which requires the integral boundary layer parameters of displacement and momentum thicknesses, suffers from errors due to averaging of the shear stress axially as the flow profile continually develops if the two axial stations are far apart. Conversely, if the velocity measurement locations are close together, the difference in the momentum thickness is smaller, leading to larger estimated error [15]. A correction for the pressure gradient term must also be applied.

Floating element balances also suffer from averaging effects when used in two-dimensional boundary layer flow, along with pressure gradient effects due to finite gap size. Floating elements may also have alignment issues with the wall of the wind tunnel [16].

Control volume approaches have uncertainties due to deviations in the fully developed flow assumption. Boundary layer curve fits attempt to take a measured velocity profile and fit it to an accepted analytical or empirical profile. Examples

of these include the log-law or a linear fit in the viscous sublayer. It is challenging to obtain reliable velocity measurements in the viscous sublayer, due to the spatial limitations of the velocimeter in use. Pitot probes suffer from blockage related effects, hot-wire has heat conduction effects, and optical flow diagnostics such as PIV often suffer from glare. These difficulties often result in the use of curve fits applied to the log-law region. Blackwelder [17], compared the friction velocity determined through the viscous sublayer and log-law regions and found that the viscous sublayer fit was 15% less than the log-law region determined friction velocity.

It is also questionable as to the applicability of the log-law curve fits when they are not applied along the centerline of the duct, due to the presence of secondary flow, or in the presence of suction or blowing at the wall. Just as is the case for rough, solid walls, Kong [11] indicates that the effects of porosity only change the near-wall velocity profile and that the log-law is still valid, albeit shifted so that lower velocities are present in the porous case at the same wall-normal location as the smooth wall case.

In several investigations, there tended to be an association of higher measured skin friction for increasing porosity as well as decreasing hole aspect ratio, the ratio of the thickness of the perforate to the diameter of the orifices [8, 14]. Hwang [13] noted a slight decrease in skin friction when the holes were angled at 15° to the surface compared to a vertical alignment. Others have fit an equivalent roughness to the liner in an attempt to characterize the liner's roughness effects in terms of well-studied sand grain roughness [8, 18]. Kong [11] states that there are distinct differences in the nature of a porous, rough wall from a solid, rough wall. These differences indicate a need for a better understanding of the near-wall physics of acoustic liners in order to better model the effects of porosity and roughness separately. Many larger-scale facilities also have the disadvantage of being unable to investigate the coupling between acoustic excitation and skin friction on an acoustic liner in a controlled fashion. The use of large-scale in this context relates to the dimensions of the facility with respect to the cut on of higher order acoustic modes. Larger tunnels often have physical dimensions too large to guarantee propagation of the plane wave mode alone for the frequencies of interest. Despite this lack of control over the applied acoustic field, noticeable increases in the measured skin friction when broadband excitation was introduced at low velocities have been reported, although the effect was less pronounced with increasing flow speeds [10], or required an increase in the sound pressure level for the same differential in skin friction [9]. This trend has also been noted for tonal excitation [14]. The sum of these past studies is that the friction factor tends to be higher when there is:

- Increased porosity,
- Low hole aspect ratio,
- High SPL excitation, low speed.

It is noted that these effects are widely agreed upon in studies where a momentum integral [9, 10, 18] or control volume [14, 19] approach is used. It is likely that these trends are at least partially due to bias in the measurements due to neglect of the

turbulent momentum flux through the wall, as will be discussed in Section 1.5. Prior to that, details of the velocity profiles used for curve fitting will be discussed.

1.4 Single Profile Velocity Curve Fits

Determination of the wall shear stress through a velocity profile taken at a single axial station is carried out by fitting various portions of the measured velocity to the analytical solution of the mean velocity profile for two-dimensional, wall-bounded flows. The problem of flow over a wall is multiscale, with the definition of inner and outer scales. Very near the wall, in the viscous sublayer, the velocity profile is

$$u^+ = y^+, \tag{10}$$

where $(\quad)^+$ denotes normalization of a variable by the inner scales. The inner velocity scale, or friction velocity is $u_\tau = \sqrt{\frac{\tau_w}{\rho}}$ and the viscous length scale is $\delta_\nu = \frac{\nu}{u_\tau}$. Beyond this region, which persists only until about $y^+ \approx 5$, there is a buffer region where viscous and inertial scales are of mixed importance. This region is marked by significant turbulent production. Farther away from the wall, a log-law region, derived using matched asymptotics, bridges the outer scales with the inner scales. The velocity profile in this region is

$$u^+ = \frac{1}{\kappa} \ln y^+ + B, \tag{11}$$

where κ and B are constants that are universal, at least for each type of boundary layer flow. Spalding [20] proposed a composite velocity profile

$$y^+ = u^+ + e^{-\kappa B}\left[e^{\kappa u^+} - 1 - \kappa u^+ - \frac{\left(\kappa u^+\right)^2}{2} - \frac{\left(\kappa u^+\right)^3}{6}\right]. \tag{12}$$

Use of Spalding's profile allows for inclusion of data over the majority of the duct, except near the centerline where the wake region is present. While there is wide agreement that a log-law exists, there is disagreement as to the exact value of the constants. A review of boundary layer, channel, and duct literature [6] shows variations of κ by as much as 10% in some studies, around the generally accepted value of 0.4. Uncertainty in the exact value of the log-law constants is one of the largest error sources when determining the shear stress in this manner.

1.5 Momentum Integral Approach

In many facilities where the wall shear stress is measured, there is typically not sufficient axial distance to obtain a fully developed profile, and it is more appropriate to use relationships derived for two-dimensional boundary layers. This is especially the case if the aspect ratio of the duct is large, and the boundary layer growth from the far walls is small enough that the central portion of the duct is dominated by effects from the two near walls. For a turbulent, incompressible flow, the mean boundary layer equations reduce to

$$\frac{\partial \langle u \rangle}{\partial x} + \frac{\partial \langle v \rangle}{\partial y} = 0, \tag{13a}$$

and

$$\langle u \rangle \frac{\partial \langle u \rangle}{\partial x} + \langle v \rangle \frac{\partial \langle u \rangle}{\partial y} = U_0 \frac{dU_0}{dx} + \nu \frac{\partial^2 \langle u \rangle}{\partial y^2} - \frac{\partial \langle u'v' \rangle}{\partial y}, \tag{13b}$$

where $\langle \quad \rangle$ denotes an ensemble average, $'$ represents the fluctuating component, and U_0 is the free stream velocity. Multiplication of continuity by $\big(\langle u \rangle - U_0 \big)$ and addition to the axial momentum equation gives

$$\begin{aligned} -\nu \frac{\partial^2 \langle u \rangle}{\partial y^2} = & \frac{\partial}{\partial x} \big[\langle u \rangle U_0 - \langle u \rangle^2 \big] + \big(U_0 - \langle u \rangle \big) \frac{\partial U_0}{\partial x} \\ & + \frac{\partial}{\partial y} \big[\langle v \rangle U_0 - \langle u \rangle \langle v \rangle \big] - \frac{\partial \langle u'v' \rangle}{\partial y}, \end{aligned} \tag{14}$$

which can be integrated across the boundary layer in order to provide an estimate of the wall shear stress. It is useful to present the results in terms of the displacement and momentum thicknesses, respectively,

$$\delta_1 = \int_0^\infty \left(1 - \frac{\langle \rho \rangle}{\rho_0} \frac{\langle u \rangle}{U_0} \right) dy \tag{15a}$$

and

$$\delta_2 = \int_0^\infty \frac{\langle \rho \rangle}{\rho_0} \frac{\langle u \rangle}{U_0} \left(1 - \frac{\langle u \rangle}{U_0} \right) dy, \tag{15b}$$

as well as the definition of the shape factor $\mathbb{H} = \delta_1 / \delta_2$. For the incompressible case assumed here, the density across the boundary layer is equal to the free stream density, and it disappears from Equations 15. The result is further normalized by the square of the free stream velocity to present a coefficient of friction

$$\frac{C_f}{2} = \frac{d\delta_2}{dx} + (2 + \mathbb{H}) \frac{\delta_2}{U_0} \frac{dU_0}{dx} + \frac{\langle u'v' \rangle_w}{U_0^2}. \tag{16}$$

So long as there is no bias flow added through the liner, the mean wall normal velocity at the surface of the porous liner will be zero. However, there will be a finite contribution of momentum flux into the main flow through the Reynolds shear stress, the final term in Equation 16. In literature, references to this effect are scant even though neglecting the Reynolds shear stress term is not inherently justified. Boldman [10] noted that "the holes in the surface plate provide active sites of turbulence production," although no compensation for this effect was included in the momentum integral used. Howerton and Jones [19], using the control volume approach, also stated that the pressure drop cannot be attributed solely to the skin friction due to the effects of the cavity.

The value of the Reynolds shear stress term, averaged in the axial direction, is proportional to the square root of porosity and the value of the the Reynolds shear stress averaged over the area of a single orifice, which may partially explain the reported dependance of measured skin friction drag on the porosity [8, 9].

Further, the momentum integral equation for a compressible boundary layer,

$$\frac{C_f}{2} \approx \frac{d\delta_2}{dx} + \frac{\delta_2}{U_0}\frac{dU_0}{dx}\left(2 + \mathbb{H} - M_0^2\right), \tag{17}$$

presented here for a smooth wall, has an additional term [1,10]. The density change across the boundary layer must also be accounted for in the definition of the displacement and momentum thicknesses. The multitude of potentially confounding effects using the momentum balance method requires that the researcher take great care in order to eliminate perceived changes in the wall shear stress due to other factors.

1.6 Control Volume Approach

The mean axial pressure gradient can be related to the wall shear stress through a control volume analysis. Consider the differential control volume containing the region of fluid within the duct, bounded axially by the upstream and downstream ends of the liner, as shown in Figure 1. The coordinate system in Figure 1 follows the convention used throughout this paper. The change in momentum flux is equal to the balance of the pressure forces, wall shear stress, and turbulent momentum fluxes through the boundaries for a steady, incompressible flow. The differential

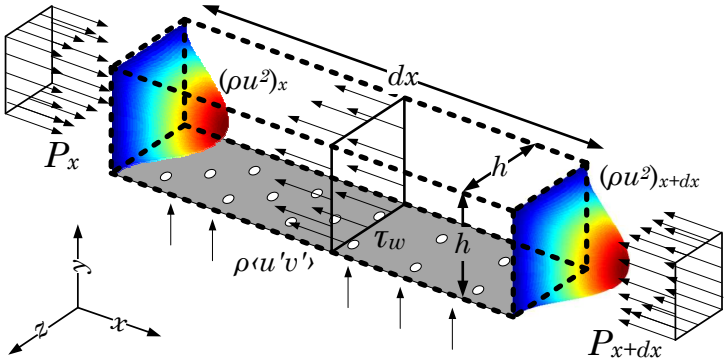

Figure 1. The differential control volume in a duct for determining the wall shear stress.

relationship is

$$-\tau_w\, dx\, dl + P_x dA - P_{x+dx} dA = -(\rho u^2)_x dA + (\rho u^2)_{x+dx} dA - \rho uv\, dx\, dl, \tag{18}$$

where dl is the closed contour tracing the perimeter of the duct. In the limit of $dx \to 0$, this becomes

$$-\tau_w dl + \rho uv\, dl = \frac{dP}{dx} dA + \frac{d}{dx}(\rho u^2) dA. \tag{19}$$

Performing a Reynolds decomposition yields

$$-\langle\tau_w\rangle\, dl = -\rho\left\langle u'v'\right\rangle dl - \rho\langle u\rangle\langle v\rangle\, dl + \frac{d\langle P\rangle}{dx} dA + \frac{d}{dx}\left(\rho\langle u\rangle^2\right) dA, \tag{20}$$

where the term $\rho \langle u \rangle \langle v \rangle dl$ is zero due to the condition that there is no mean flow through the orifices, and the term containing the axial gradient of $\rho \langle u' \rangle^2$ is neglected due to boundary layer scaling considerations. When the equation is integrated over the limits of the duct, the result is

$$\overline{\langle \tau_w \rangle} = \frac{\rho\sigma}{4} \overline{\langle u'v' \rangle}_w - \frac{h}{4} \frac{d \langle P \rangle}{dx} - \frac{1}{4h} \frac{\partial}{\partial x} \int_0^h \int_0^h (\rho u^2) dy\, dz. \tag{21}$$

The $\overline{\langle \quad \rangle}$ denotes a spatial average around the periphery of the duct, and σ is the porosity of the liner. For the wall shear stress, this is the value averaged over the perimeter of the duct. The Reynolds stress flux through the wall is averaged on the basis of a single orifice and multiplied by the porosity. In order to determine a wall shear stress using the pressure drop alone, the assumption of a fully developed flow and negligible momentum flux must be made. The fully developed flow assumption and the contribution of the Reynolds stress will be addressed through the use of particle image velocimetry (PIV) in Section 6.8. Work done by Howerton and Jones [19] does show some evidence to the contrary, as comparisons between a liner with a hole aspect ratio of one and ten show consistently higher pressure drop with the high hole aspect ratio. They also tested various orifice geometries in order to investigate whether the pressure drop could be significantly affected while minimizing the impact on the acoustic performance. The geometry of a spanwise aligned slot was shown to produce a reduction in the pressure drop when compared to the baseline conventional circular orifice geometry. There have been several studies that have used this geometry in order to investigate the effects of steady or periodic blowing to reduce the skin friction [21, 22]. It is likely that part of the reason it has been difficult to comprehend the results of pressure gradient or momentum balance experiments is that their integral nature doesn't require any knowledge of the dynamics of the flow, instead utilizing the relationship between the inputs and outputs of the system. Detailed measurements of the interior domain are necessary to understand the complex interplay between pressure drop contributions from the Reynolds stress, the impact varying the geometry can have on the alignment and strength of vorticity production at the orifice, the subsequent impact of the vorticity on the near-wall structure, and the change in the wall shear stress and boundary layer shape factor due to disruption of the natural flow structure.

Apart from the fully developed assumption, it should be kept in mind that the values of the wall shear stress in this report determined through this procedure are averaged over the wetted area as the pressure gradient is determined through a least-squares fit over the appropriate axial length. For some of the acoustic cases, there may be significant attenuation, and the wall shear stress could vary as a function of axial location.

1.7 Drag Balances and the Capacitive Wall Shear Stress Sensor

Drag balances consist of floating elements carrying the section of the wall that is of interest, and calculating the mean shearing force integrated over the element through means of a strain gauge or other transduction mechanism. Due to the large integrated area of traditional floating elements, spatial averaging effects make

a small floating element desirable. The capacitive wall shear stress sensor (CWSSS) is, in essence, a microscale drag balance. The CWSSS, shown in Figure 2 has a

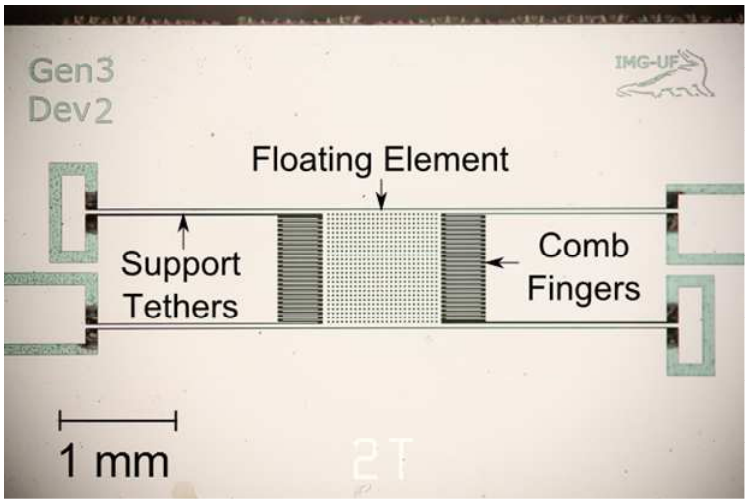

Figure 2. A photograph showing the pertinent geometry of the CWSSS. The floating element is centered in the picture, with the comb fingers placed on both sides and the tethers at each corner of the floating element.

floating element, which is connected to the die through four tethers. A differential scheme is employed between the floating element and the two external electrodes to allow for rejection of common mode deflection [23]. The comb fingers attached to the element also move with the deflecting floating element, changing the gap size between the element and external electrode fingers. This deflection causes a capacitance change that in turn leads to a voltage change. The mean change in the voltage can be related to the wall shear stress through the device's sensitivity. Direct measurement of the wall shear stress has the advantage over indirect measurements of not requiring assumptions about the velocity profile. In comparison to a drag balance, the smaller size of the CWSSS element ($1\,mm \times 1\,mm$) allows for a large reduction in the spatial averaging. Further, the bandwidth of the CWSSS allows for fluctuating information about the wall shear stress to be measured and will lead to a greater understanding of the dynamics of the flow. Further information regarding the dc and ac calibration procedures are provided in Section 3.4.2.

1.8 Report Roadmap

The basic thrusts of this work have been outlined, along with a literature review focused on the problem of estimating the liner skin friction drag. Issues with the current measurement techniques has been discussed as well. Moving forward, the facility used for liner drag measurements will be described in Section 2. The experimental setup will be detailed in Section 3. A characterization of the facility in order to establish confidence in the quality of the fluid dynamic measurements is presented in Section 4. Measurements of the acoustic impedance of two liners at several grazing flow conditions will be detailed in Section 5. In Section 6, the PIV

results are presented, highlighting some differences in the near wall flow structure of a duct with an acoustic liner compared to the hard walled case. Section 7 will present the results of the wall shear stress for two liners carried out through multiple methods and compare them to the hard walled case. Section 8 provides a concise summary of the major findings of this grant.

2 Facility

The Grazing Flow Impedance Duct (GFID) at the University of Florida is a modified version of a previous NASA Langley facility, the Grazing Incidence Tube (GIT). The goals of the modifications were to allow for optical-based fluid dynamic measurements, expansion of the acoustic excitation capabilities, and improvement of the quality of acoustic impedance testing by integrating an anechoic diffuser.

The GFID is a blow-down wind tunnel receiving air from a compressed air source. A representative sketch of the relevant tunnel components is shown in Figure 3. Air

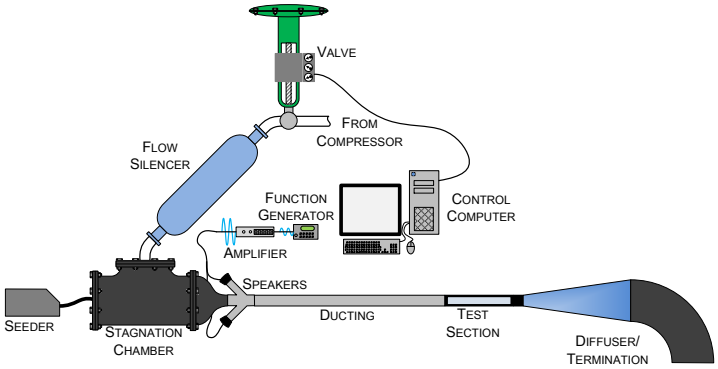

Figure 3. The main components of the GFID are shown.

from the compressor is passed through a valve in order to regulate the mass flow rate into the stagnation chamber. A flow silencer is located prior to the entrance to the stagnation chamber in an effort to reduce the noise of the incoming flow. Within the stagnation chamber, a seeder introduces atomized Di-ethyl-hexyl-sebacate (DEHS) particles, which mix with the flow during PIV testing. After the flow is accelerated through the nozzle, an acoustic section provides excitation. The flow and acoustics propagate in the waveguide ducting before reaching the test section, where optical access and a variety of test plugs and windows allow for a wide array of acoustic and fluid dynamic testing. The test section also allows for installation of the acoustic liners. The cross-section of the tunnel is $50.8\,mm \times 50.8\,mm$.

2.1 Instrumentation and Control

Several transducers are placed in the stagnation chamber in order to record flow conditions. The stagnation pressure, p_0, and stagnation temperature are measured at the aft wall of the stagnation chamber. A differential pressure referenced to atmospheric pressure is measured at the exit of the nozzle using a physical average of four total pressure taps, one placed on the center-span of each side of the duct. The static pressure at the nozzle, p, is recovered through measurement of the atmospheric pressure using a separate transducer. With knowledge of the static and stagnation pressure, the bulk Mach number, M_b, at the nozzle exit can be calculated using the

isentropic relation, Equation 22, and used as a control input,

$$\frac{p}{p_0} = \left(1 + \frac{\gamma - 1}{2} M_b^2\right)^{\frac{-\gamma}{\gamma - 1}}. \tag{22}$$

The tunnel conditions are monitored in LabVIEW, and a proportional-integral-derivative controller is used to alter the stagnation pressure in order to maintain the desired bulk Mach number. The LabVIEW controller issues a voltage, which is used to regulate the pressure in a supply line connected to the control valve. The change in line pressure actuates the control valve supplying high pressure air to the stagnation chamber. For further details, see Bertolucci [24].

2.2 Acoustic Section and Anechoic Diffuser

Two acoustic sections have been designed and built for the GFID, a single driver section and a dual driver section. Figure 4 shows both of the acoustic sections. The single driver section is capable of delivering 140 dB SPL tonal excitation up to 3 kHz at $M_b = 0.26$, which corresponds to a test section Mach number of 0.3. The single driver section mounts the driver directly to the wall of the duct, with

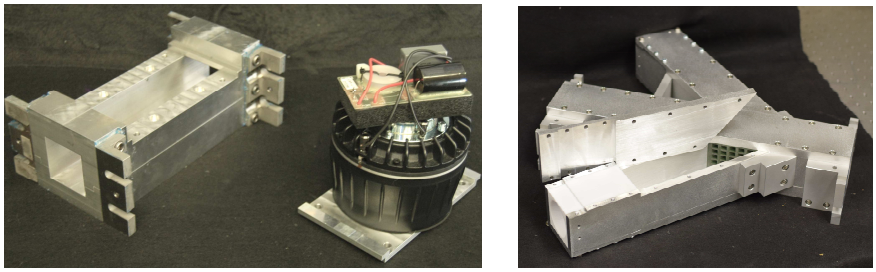

Figure 4. The single (left) and dual driver (right) acoustic sections.

only a thin bulk material and felt metal sheet separating the speaker exit from the flow. The bulk material provides structural support to the felt metal, which reduces the impinging flow perturbations on the speaker while still allowing the acoustic excitation to propagate into the duct with minimal losses.

The dual driver system is slightly different in that the acoustics propagate through side branches prior to joining the main duct. White rapid prototype material, pictured in the lower left of the dual driver assembly in Figure 4, provides a smooth transition from the circular driver exit to the rectangular side branch to reduce impedance mismatches from the change in area. This modular transition allows for future optimization of power transfer out of the speaker and into the duct with minimal impact to the dual driver section. The same type of material interface is used at the junction of the side and main branches to present enough resistance to avoid any Helmholtz resonances in the side branches.

The single driver section was installed during all of the testing contained herein. Although the dual driver section was available for the final round of pressure gradient and CWSSS testing, the PIV data was taken prior to final delivery of the dual driver

section. As the schedule did not permit for additional PIV data to be taken with the dual driver section, it was thus deemed more appropriate to retain the single driver section for all testing to avoid any measurement differences due to changes in measured downstream location originating in the difference in the length of the two acoustic sections.

Two diffusers are available for use during the course of the testing: a hard wall fiberglass diffuser and an anechoic diffuser. The anechoic diffuser is pictured in Figure 5. Both have the same internal geometry, linearly increasing the perimeter of the diffuser with downstream location from the $50.8\,mm \times 50.8\,mm$ cross section at the upstream end to $206\,mm \times 232\,mm$ at the downstream end over a length of $3.05\,m$. The anechoic diffuser surface is a locally reactive liner, with a wire mesh face sheet over honeycomb. The honeycomb depth increases with downstream distance, from $3.18\,mm$ at the upstream end to $154.7\,mm$ at the downstream end. The wire mesh is $1.59\,mm$ thick with a static resistance of $320\,cgs\,Rayl$. Due to the potential for DEHS particles to condense and collect on the wire mesh and change the effectiveness of the anechoic diffuser, the fiberglass diffuser was used for any testing that required flow seeding.

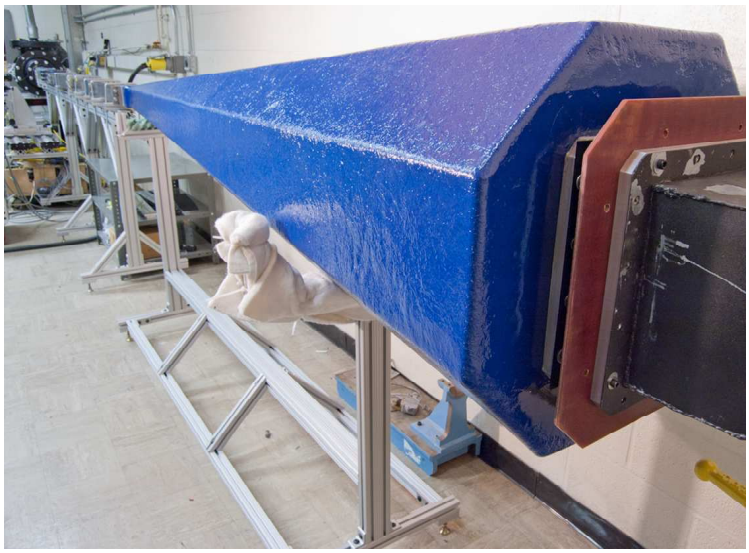

Figure 5. The anechoic diffuser is shown installed on the GFID.

2.3 Test Section Description

As was mentioned in the introduction to this section, the test section was redesigned to allow for fluid dynamic testing as well as acoustic impedance testing. To this end, a test section with modular windows and test plugs was designed and implemented. Three test plugs are available, apart from the blank test plug: a plug for pitot-static measurements, one for acoustic measurements, and an insert for the CWSSS. Figure 6 shows the available test plugs along with the outer plug that provides a common interface with the GFID. The outer plug also has fiducial marks for alignment of the test plugs with the GFID. Three walls are also available: optical quality

polycarbonate and acrylic walls, a linear microphone array, and static pressure port measurement ports. Lastly, back plates were made to accommodate acoustic liners of varying depth, as well as a back plate to allow for feed-through of the CWSSS cabling when it was installed in the liner. The pitot-static test plug is used in Sec-

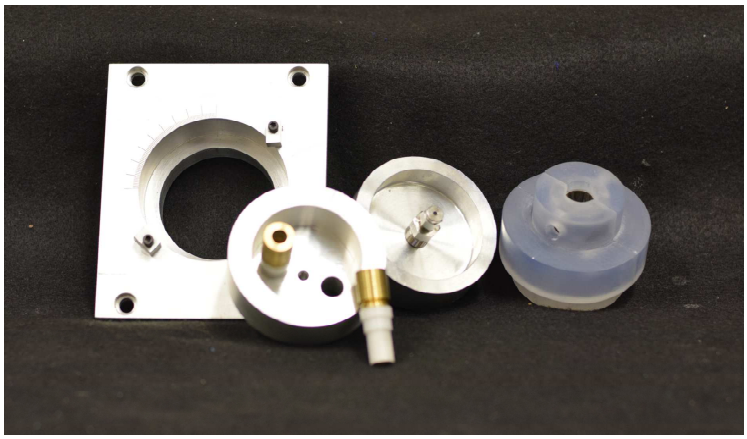

Figure 6. The various test plugs for the GFID are shown. From left to right, the outer plug with flush mount microphone packaging, acoustic plug, pitot plug, and CWSSS plug are shown.

tion 4.3 in order to calibrate the value of the centerline test section Mach number to the corresponding value of the bulk Mach number at the nozzle exit. The acoustic test plug is used to determine the exit impedance that the two diffusers present to propagating acoustics in the GFID, as well as functioning as a reference microphone plug upstream of the liner during acoustic testing.

Figure 7 shows the side walls that are used in the testing. The static pressure

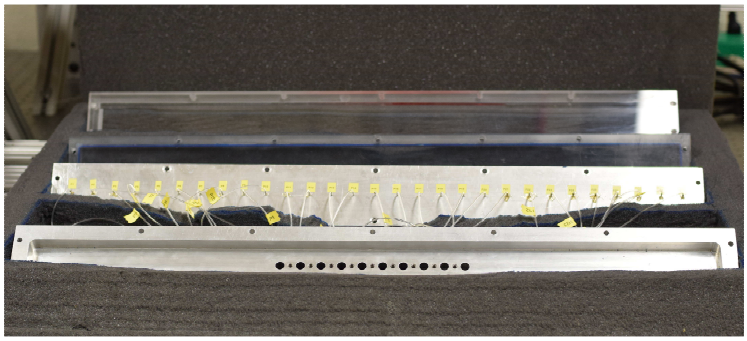

Figure 7. The image shows all of the side walls that are available for use in the GFID. From front to back are the linear microphone array, static pressure tap, and optical quality walls.

port window is an aluminum plate with 29 tubulations which are located on the duct centerline with an axial spacing of 25.4 mm. The holes were counterbored so that when the 0.040 in. tubulations were inserted to the end of the counterbore, the internal diameter of the tubulation and through hole are a continuous 0.032 in..

Care is taken to ensure that the interior surface is free of burrs and that there is no rounding of the edges of the through holes. Two optical quality walls, a Makrolon WG polycarbonate window 28.6 mm thick, and an acrylic window 32 mm thick, were used during PIV measurements.

The linear microphone array window has installation ports for 10 microphones to be placed on the centerline of the duct, with the middle of the array centered aligned axially with the acoustic liner. The spacing between the microphones is 21.6 mm, and the installation ports allow for use of flush mount packaging, on loan from The Boeing Corp, of screenless $1/4\,in.$ microphones. Several microphones were utilized during the course of the acoustic measurements: GRAS 46BD, GRAS 46BG, Brüel & Kjær (B&K) 4939, and a piezoelectric microphone developed in house. The quoted performance of these microphones is provided in Table 2. Williams [25] provides a more detailed description of the performance of the in-house piezoelectric microphone. The dynamic range the GRAS and B&K microphones are specified in dBA for the lower limit, while the lower limit for the UF microphone is the spectral power in a $1\,Hz$ bin centered at $1\,kHz$. All microphones are specified in dB SPL for the upper threshold of the dynamic range. For impedance eduction, the GRAS and B&K microphones are used in the microphone array. However, the UF piezoelectric microphone is used during PIV testing due to the device's relative insensitivity to environmental factors presented by seeding the flow compared to condenser type microphones.

Table 2. Mic Performance Specifications.

Microphone	Bandwidth $[Hz]$	Dynamic Range [dB]	Sensitivity, $[\mu V/Pa]$
GRAS 46BD	4–70E3	44–166	1450
GRAS 46BG	3.15–70E3	60–184	250
B&K 4939	4–100E3	28–164	4000
UF Piezoelectric	69–20E3	40–172	40

3 Experimental Setup

The equipment and procedures used are detailed in the following section. First, information regarding the impedance eduction testing will be presented. Next, the details of the velocity measurements using optical techniques will be reviewed. Following that, some principles of operation for the CWSSS will be given, along with explanation of the calibration procedure. Finally, the process for pressure gradient testing will be given.

3.1 Acoustic Testing

Two acoustic liners, supplied by NASA Langley, were tested in the GFID, denoted as L1 and L2. Both are conventional liners with a perforated face sheet covering honeycomb cells and are terminated by acoustically rigid acrylic surfaces. Both liners have a staggered hole pattern in the perforate. The geometric details of both liners can be found in Table 3. In order to increase the quality of near-wall PIV, liner L2 has an anodized surface. It also has a CWSSS mount for in situ wall shear stress testing. When the shear stress sensor is not in use, a rigid, flush-mounted filler blank is used to plug the hole. The liners L1 and L2 are pictured in Figure 8. Due to the relative compactness of the rigid filler blank compared to the wavelength, it is not expected that the inhomogeneity will alter the acoustic impedance measurement. This has been verified through comparative testing done over the entire liner in the GFID and a uniform portion of the liner in a plane wave tube.

Table 3. Acoustic Liner Geometric Parameters.

Dimension	L1	L2
Length (mm)	415.5	415.5
Width (mm)	63.5	63.5
Thickness (mm)	49.0	36.3
Perforate Thickness (mm)	0.8	1.0
Perforate Hole Diameter(mm)	1.3	2.4
Perforate Open Area (%)	6.3	12.7
Honeycomb Thickness (mm)	35.6	19.0
Acrylic Thickness (mm)	12.7	16.3

The impedance of each liner was measured for two different Mach numbers over a range of frequencies. Plane-wave acoustic excitation, measured to be 130 dB SPL at the reference microphone located $2.25\,D_h$ upstream of the liner, was present for all of the impedance testing. The L1 liner was tested at a bulk Mach number of 0.1 and 0.3, while the L2 liner was tested at a test section centerline Mach number of 0.1 and 0.3. This change in choice of Mach number is reflective of the authors' attempt to be more in line with the more often reported value of centerline test section Mach number in acoustic liner research. The impedance is determined at $500\,Hz$ intervals up to $3\,kHz$, and in $25\,Hz$ intervals near the expected resonant frequency.

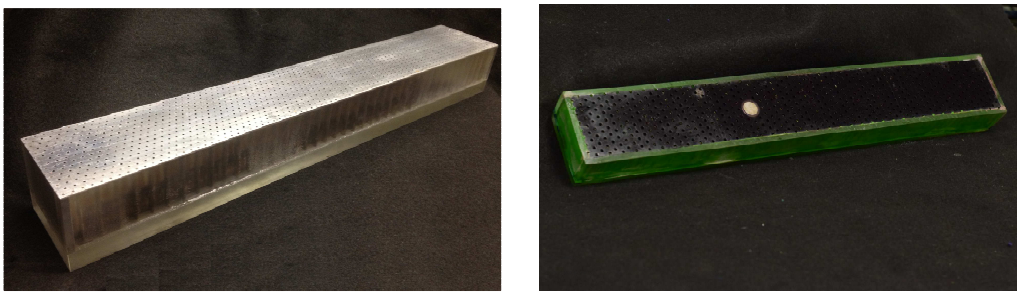

Figure 8. The image shows both the L1 (left) and L2 (right) acoustic liners that were tested. The stainless steel circle along the centerline shows the location of the CWSSS insert.

The acoustic pressure was recorded using a combination of flush-mounted 1/4" microphones. The reference microphone was a GRAS 46BG, while the first six upstream microphones in the array were B&K 4939, and the remaining array microphones were GRAS 46BD. The fluctuating surface pressure was sampled for one minute at 25.6 kHz. The autospectral density at each microphone was computed using `pwelch` in MATLAB using a Hanning window on blocks of 1024 points with 75% overlap. The sound pressure level at each microphone was recovered with the product of the power spectral density, spectral line spacing, and a factor of 1.5 to account for the power lost due to use of the Hanning window. Accounting for the correlation between the overlapped blocks, this results in over 3000 effective averages of the spectrum. The magnitude was further scaled by the coherence between the reference and measurement microphones in order to eliminate added power due to uncorrelated hydrodynamic noise. Although hydrodynamic fluctuations can persist in the streamwise direction, the reference microphone's location on an adjacent wall assures that the hydrodynamic fluctuations are uncorrelated with the measurement microphones as they are separated by a significant spanwise extent. The phase between microphones is estimated by the angle of the cross-spectrum between the measurement and reference microphones.

The microphones were calibrated for magnitude through the use of a Brüel & Kjær 4231 Sound Calibrator with an accuracy of ±0.2 dB SPL [26]. The phase calibration was performed using a plane wave tube with the reference and measurement microphone placed at the end of the duct in a rigid plate. The relative phase of each microphone to the reference microphone was determined through the cross-spectrum. Variations in the phase calibration taken before and after the measurements were limited to ±0.1°.

3.2 Laser Doppler Velocimetry

Some early facility characterization was performed using laser Doppler velocimetry (LDV). The results included here consist of axial velocity measurements with a single probe head, although the system is capable of simultaneous measurement of all three velocity components. A Coherent Innova 90C Ar^+ laser provided continuous wave

light to a Dantec FiberFlow probe head. The probe head also acts as a collector for the backscattered light off the sampled particles. The returned optical signal was then processed using a Dantec BSA to obtain the instantaneous velocity. In order to obtain measurements at various spatial locations, a three axis Parker traverse was used with a step resolution of $3\,\mu m$. The probe volume for the optical setup is an ellipsoid with major axis $360\,\mu m$, oriented in the spanwise direction, and minor axes of $58\,\mu m$, a function of the optical setup.

3.3 Particle Image Velocimetry

Both sPIV and two-component planar PIV were used to analyze the flow over a liner in order to compare the characteristics of the near-wall flow against the baseline case of a fully developed turbulent duct flow for various acoustic conditions. In order to comment on the merit of using wall based sensors to determine the wall shear stress, as well to investigate the impact of placing the hard wall 'island' in the middle of the acoustic liner, several cases will be taken over a hard walled patch (CWSSS insert) placed within the liner perforate. The liners are described in Section 3.1. During acoustic characterization of liner L2, two frequencies of interest were chosen for fluid dynamic testing: the resonant frequency and the frequency of maximum attenuation. Both of these frequencies will change as a function of the centerline Mach number, and are determined from the results of the acoustic testing for the appropriate flow conditions. The resonant frequency was chosen as it is expected to provide the highest amount of jetting in and out of the orifice. The maximum attenuation frequency was chosen based on the results of the liner impedance testing, which showed that there was not a significant amount of attenuation near the resonant frequency. As the liner has a low aspect ratio, much of the resistance component is due to the transferal of acoustic energy into vortical shedding as flow enters and leaves the orifice. Thus, the frequency of maximum attenuation was also targeted as an acoustic forcing condition where significant interaction with the flow through vortex shedding was expected. In total, the baseline hard walled measurement will be compared against four liner cases and three liner patch cases. The liner cases are a baseline case with no acoustic stimulus, a broadband case, and the two tones of interest. The three patch cases are a baseline case, broadband, and a tonal case at a single phase of 90° at the resonant frequency. For the liner cases, the tonal data is taken in eight phase-locked sets spread evenly over the entire period. The patch tonal case is taken at only a single phase, with the assumption that the validity of whether the patch and liner cases are the same can be determined from just one phase. All cases are taken with a nominal centerline Mach number of 0.1. Acoustic excitation is at 140 dB SPL for the tonal cases as well as the broadband signal over the excited frequency range of $500\,Hz$ to $3\,kHz$. The excitation level is higher than that used for the impedance testing, as the goal of the PIV data is to explore the near wall jetting effects, which are pronounced at higher excitation levels. The goal of the impedance testing is to identify the resonant frequency, which is independent of the nonlinear resistance that changes as a function of excitation level.

3.3.1 Equipment and Setup

Several cases are captured using two different PIV configurations. The setup used for all but one case is shown in Figure 9. A Litron Lasers Nano L PIV Nd:YAG laser with a -10 mm cylindrical lens was used to produce a double-pulsed light sheet of 532 nm wavelength. Two cameras are used in a stereo PIV configuration along with

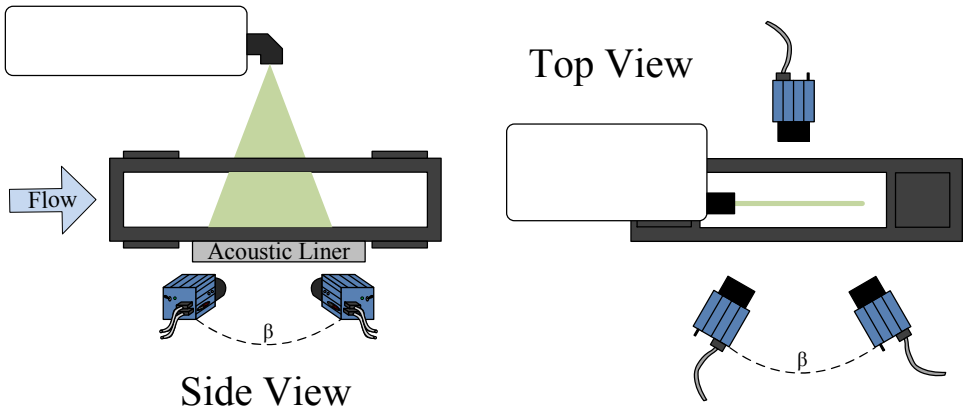

Figure 9. A side and top view of the test section, PIV cameras, and laser are shown.

an additional camera on the opposing side of the tunnel in a two-component setup. This allowed for a stereo view of the near wall region to be taken simultaneously with a two-component view of the half-duct. The stereo camera separation angle, β, is approximately $70° - 80°$, depending on the setup for the particular case. The two stereo cameras are LaVision Imager sCMOS. Scheimpflug attachments are used to tilt the imaging plane so that the entire image is in focus. Nikon macro lenses with a focal length of 200 mm are used, along with $2\times$ teleconverters, with the resulting magnification around 1.7. The aperture is set to either $f/11$ or $f/16$. The two component camera in the setup is a LaVision Imager ProX with a 60 mm lens, with a magnification of 0.4, and at an aperture of $f/4$. The time between snapshots is set to $2\mu s$, which was optimized for the near wall stereo setup. Accordingly, the pixel displacements of particles in the two component setup was smaller due to the increased field of view, although this is offset somewhat by the higher velocity present in the core region of the flow.

The setup for the hard wall two component (HWT) case was slightly different, to investigate some concerns with the quality of the near wall data in the hard wall upstream (HWU) case. This consisted of using a single camera in a two-component setup to measure the near wall velocity field, while two cameras in a side by side two-component setup were used to capture the outer flow. The two side by side fields of view overlapped and were stitched together in order to provide a single larger field of view.

As much of the focus of the PIV was to gain better insight into the near wall physics of flow over a liner, it was necessary to ensure that glare from the light sheet contaminated as little of the field as possible. Application of Dykem steel red layout fluid was found to greatly reduce the intensity of the reflected light. For the cases

taken over the L2 CWSSS insert, 3M Scotchcal^{TM} fluorescent orange film is used. This has the effect of shifting the wavelength of the reflected light, and bandpass filters centered around the laser wavelength to allow for filtering of the reflected light.

In order to accurately determine the velocity of the flow, a mapping of the camera view to the flow coordinates must be made. For sPIV, a two level calibration target is required in order to accurately determine the perspectives of each of the cameras. For areas of interest on the order of a few inches, two level calibration targets are commercially available. However, for small areas of interest, calibration targets must be manufactured to serve the needs of the individual researcher. A custom calibration target was manufactured for the purposes of this research with outer dimensions of 20 mm square. Dots of diameter 0.5 mm were placed 1.75 mm apart in a square pattern. Dots on the second level were put in the same basic pattern, but translated 0.875 mm in both directions, as shown in Figure 10. The channels were milled using conventional processes, and the plate was then anodized. The dots were produced by ablating the oxide layer with an Oxford J-355PS laser micromachining station with a Coherent Talisker Ultra picosecond laser.

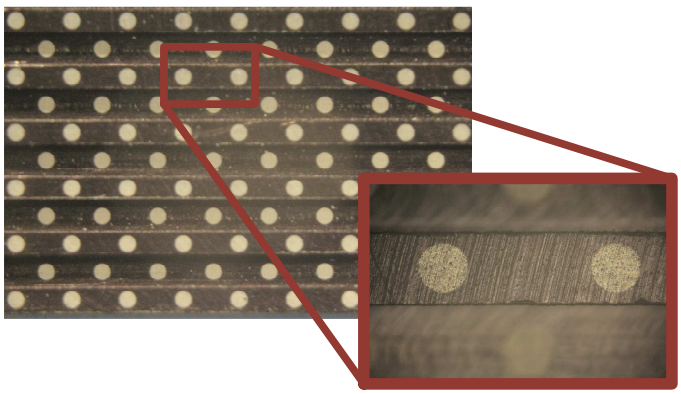

Figure 10. Illustration of the calibration target used for sPIV calibration.

3.3.2 Data Processing

The data processing procedure is outlined within this section and is representative of all data sets. The image capture, processing, and initial vector processing was all done using DaVis 8.3.0 software. The image acquisition rate varied from 7–15Hz, depending on the number and type of cameras used, with two to three thousand images being used for each case. The images were then passed through a Gaussian intensity filter, with a length of 5 snapshots. Background subtraction and particle intensity normalization were also used in preprocessing, and the filter size corresponded to two and four times the average particle size, respectively. The processing consisted of four consecutive passes, with the first two using a $4:1$ elliptical window of size $64 \times 64 px$. The last two passes were performed using an adaptive $32 \times 32 px$ window. Following each of the first three passes, universal outlier detection (UOD) [27], was

used to perform outlier rejection. Any vectors with a correlation peak ratio less than 1.1 were also discarded. The rejected vectors are filled using interpolation, and the field is smoothed using a three window square kernel. Following the final pass, only the UOD and peak ratio filtering were performed on the data to remove the outliers. The threshold for the UOD is set to a normalized residual of 3, with a three window square region used for determination of the residuals. Although the spatial outliers have been removed using UOD on a snapshot basis, it is prudent to further remove any outliers on a point-by-point ensemble in time approach. This was accomplished using multivariate outlier detection (MVOD) [28].

3.3.3 Phase-Locked Measurements

For the tonal acoustic forcing cases, phase-locked measurements are taken at eight evenly spaced intervals across the period of excitation. To avoid having to expose the condenser microphones to seeding, the phase relationship between the axial station of the PIV testing and the function generator output are determined using the axial microphone array. The trigger from the function generator is then used as a reference for the PIV triggering, which is handled in DaVis. The CWSSS insert is located at the same axial station as one of the microphones in the axial array, allowing the use of that microphone's phase to determine the phase lag with the function generator. For the PIV over the L2 liner, the cases were taken at a location slightly more upstream than the patch cases in order to take data over an orifice that was not occluded on the back side by the honeycomb. Thus, the phase was established from linear interpolation of the phases of the two microphones bracketing the L2 PIV station. The phase between the upstream reference microphone was also determined, and is used as a check during PIV acquisition. For any data where the expected phasing between the reference microphone and function generator differs more than 10°, the data is discarded and retaken. These differences in phasing were due to small differences in the air temperature and flow speed between tunnel runs.

3.4 Capacitive Wall Shear Stress Sensor

3.4.1 Packaging

The packaging form factor, as installed into the wind tunnel facility, is 0.5 *in.* in diameter and 2 *in.* in rigid length, with a 2–3 *in.* semirigid backing [29]. Figure 11 shows a representative schematic of the CWSSS packaging. Stainless steel is used as the primary cylindrical housing, with shrink wrap at the base providing strain relief for the coaxial signal cables during handling. Lines of conductive copper tape connect the circuit ground to the housing, helping to insulate the primary interface electronics within. The silicon die itself is embedded into a sensor cap, which is subsequently inserted into a recession at the tube end. In addition to the die, the two main sensor cap components are a milled PCB disk for wirebonding connections and structural support, as well as a laser machined plastic shim cap affixed around the sensor for frontside smoothness. To enable real-time measurement of both mean and dynamic shifts in capacitance, it is necessary to implement an ac-biasing setup. An analog synchronous modulation/demodulation circuit is implemented to enable

both ac and dc measurements [30]. The system applies 180° phase shifted sinusoidal biases to each of the static comb finger elements at 1 MHz. Signal is routed from the center floating element electrode to a buffer amplifier located within the steel housing. Because the amp is colocated within the sensor head, signal attenuation typically associated with high output impedance devices is mitigated. After the signal is received by the modulation circuit, it is passed through a band pass filter and gain stage, reducing coupled EMI at low frequencies and biasing harmonics at high frequencies. A phase-locked switching rectifier followed by additional low pass filters completes the envelope detection demodulation scheme, where output contains only the baseband flow information.

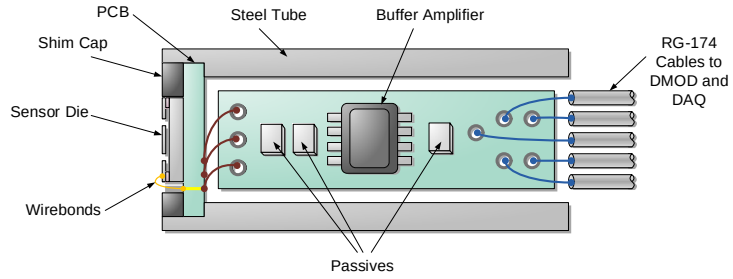

Figure 11. The illustration shows the various components of the CWSSS packaging.

In order to interface with the GFID, a hard wall insert and a liner insert were manufactured. The liner insert is shown in Figure 8, while the hard wall insert is shown in Figure 12. The CWSSS is inserted into the mounting plug, shown in blue

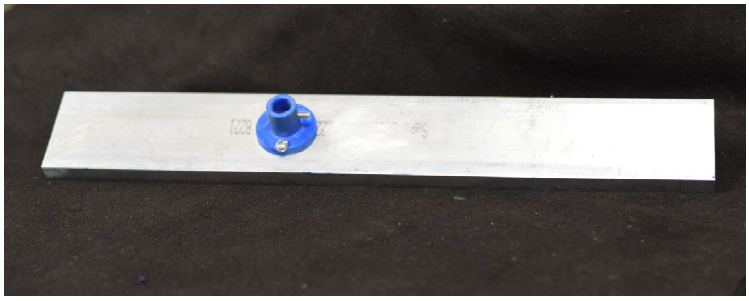

Figure 12. The picture shows the hard wall insert for the CWSSS, along with the mounting plug.

in the figure, and a set screw is used to keep the sensor aligned with the hard wall insert. The mounting plug is made of plastic and provides electrical isolation from the hard wall insert as well as the rest of the GFID when installed. The CWSSS is mounted in a similar fashion in the liner insert.

3.4.2 Calibration

General CWSSS performance, including wall shear stress sensitivity, frequency response function, and pressure rejection, are characterized in an acoustic plane wave

tube (PWT). A Stokes oscillating layer is established from the driven acoustic wave, allowing for controlled input of wall shear stress and pressure depending on sensor positioning [31]. For a PWT with a rigid termination, the pressure field has an exact solution, and the pressure field in the entire tube can be determined from pressure measurements of a single microphone at a known location. Figure 13 shows the setup for the ac calibration procedure.

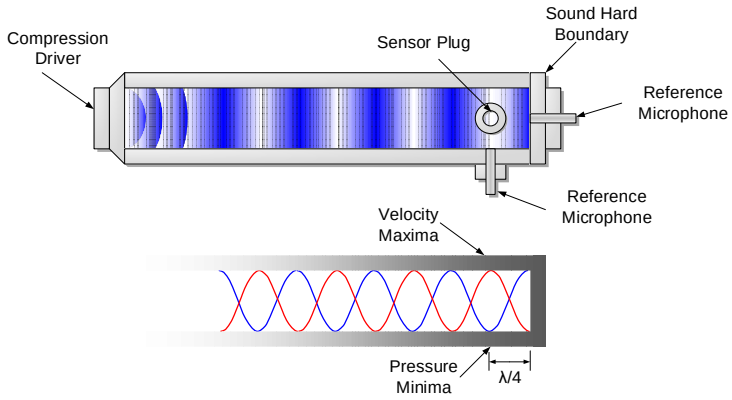

Figure 13. The setup for the ac calibration procedure in the PWT is shown along with a cartoon showing the acoustic pressure and velocity amplitudes as a function of axial distance in the PWT.

From the exact solution of the pressure field, the acoustic velocity field can also be determined, and there is a known rms velocity maximum a quarter of a wavelength from the end of the tube. The CWSSS is placed at this location in order to maximize the input shear stress for a given pressure amplitude. Using the solution to the Stokes problem, the wall shear stress can be determined for a given fluctuating pressure amplitude. By measuring the fluctuating voltage of the CWSSS at the excitation frequency for a range of pressure amplitudes, the dynamic calibration of the sensor can be obtained. A representative ac calibration curve is shown in Figure 14. The onset of linearity for low pressure amplitudes yields the minimum detectable signal, the slope of the line is used to infer the sensitivity, and any deviation from the fitted line at high pressure amplitudes would indicate the onset of nonlinearities. The range of shear stresses between the minimum detectable signal and the onset of nonlinearities is defined as the dynamic range of the sensor. The typical dynamic range of the sensor used in this report is 84 dB at 1 kHz.

In order to determine the bandwidth of the sensor, the ac calibration procedure must be carried out over a range of frequencies in order to estimate the frequency response function (FRF) of the sensor. In order to remain at a velocity maxima, the end plate of the PWT is allowed to move, as shown in Figure 15.

The pressure amplitude is set to a constant value while the frequency is allowed to vary. Figure 16 shows the FRF of a CWSSS along with bands about the sensitivity measured at 1.125 kHz with the fixed end wall. The figure indicates that the bandwidth of the sensor spans from dc to 1.5 kHz.

The dc sensitivity can also be determined using a laminar channel flow cell and

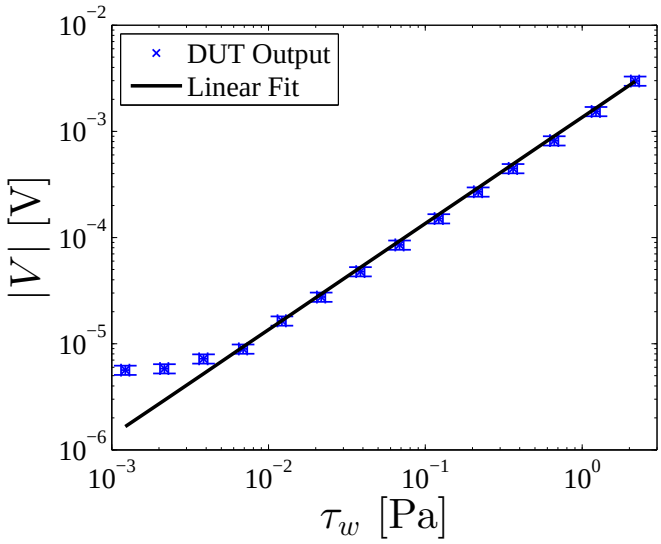

Figure 14. The rms voltage at the excitation frequency of 1.128 kHz as a function of the theoretical shear stress is presented.

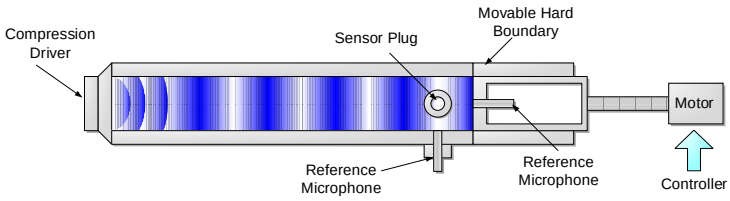

Figure 15. The modified PWT setup is shown, with a moveable end wall. This allows for placement of the pressure node at the sensor location over a wide range of frequencies.

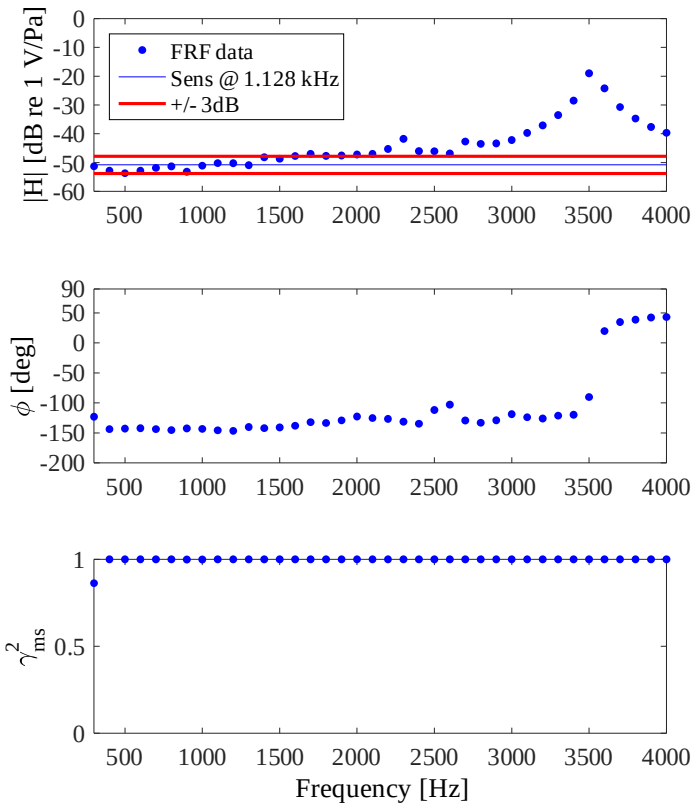

Figure 16. The frequency response function of a representative CWSSS is shown. From top to bottom, the magnitude and phase of the sensor response are shown, along with the ordinary coherence function between sensor output and the input acoustic driver.

the corresponding relationship between the shear stress and the pressure gradient, which is determined from Equation 2. The flow cell setup is pictured in Figure 17. Metered flow is introduced using a mass flow controller, and the flow is allowed to develop naturally over a sufficient distance to be fully developed. The pressure gradient and dc voltage shift of the CWSSS are measured over a range of mass flow rates and compared to the exact Poiseuille solution for laminar channel flow.

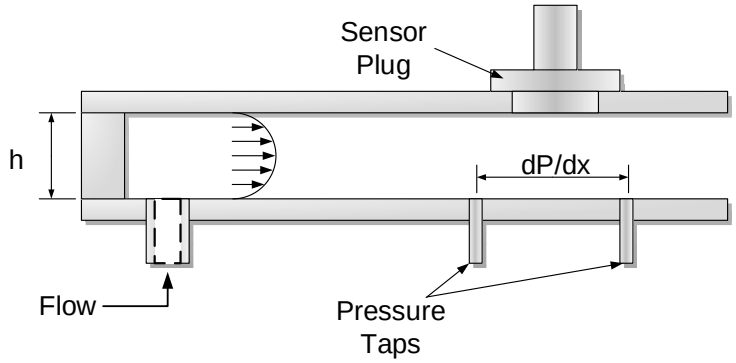

Figure 17. The laminar flow cell setup is shown where the flow is introduced into a thin channel and the pressure gradient is measured for a range of mass flow rates along with the dc voltage shift of the CWSSS. The sketch is not to scale.

A plot showing a dc calibration for a representative CWSSS is shown in Figure 18. The measured sensitivity is 3.44 mV/Pa. The sensor shows a linear response over

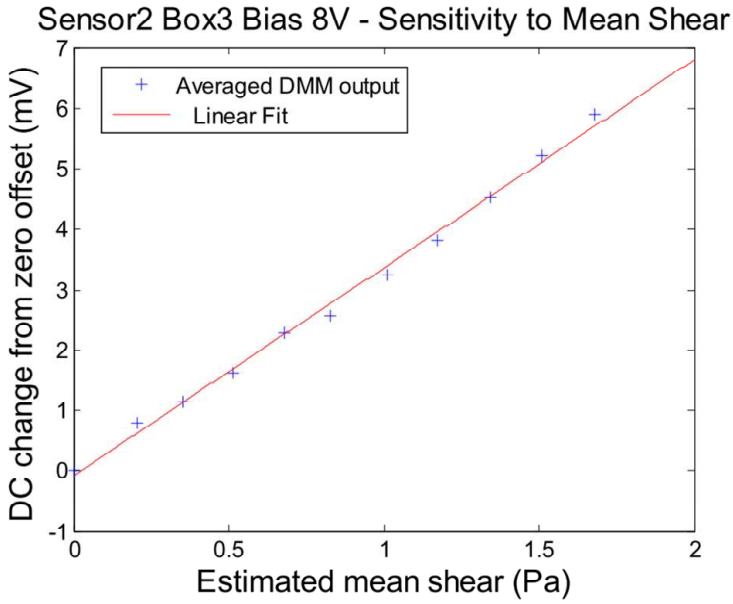

Figure 18. The dc sensitivity measured using the laminar flow cell is ascertained from the linear fit of the voltage change to the wall shear stress.

more than a decade of dc shear stress input, but the dynamic range extends much

further than the limits imposed by use of the laminar flow cell. The typical performance of the CWSSS is characterized by a sensitivity of $3.45\,mV/Pa$, calculated through the ac procedure, corresponding to a minimum detectable signal of 120 Pa, with 72 dB of pressure rejection. Frequency response analysis shows a resonance at $3.5\,kHz$, with a 3 dB flatband extending out to $1.5\,kHz$.

Measurements using the CWSSS in the GFID are taken for both the hard wall case, as well as in situ installation in liner L2. For ac measurements, the same sampling parameters as those for impedance testing are used; the sampling frequency is $25.6\,kHz$ over a period of one minute. For dc measurements, the voltage signal is averaged over two power line cycles, and taken for a period of either three or five minutes.

3.5 Pressure Testing

The axial static pressure in the GFID is measured in 16 locations along the length of the test section by a Pressure Systems 9116 module. Eight channels have a range of $\pm 2490\,Pa$ ($\pm 10\,inH_2O$) while the other eight have a range of $6890\,Pa$ ($\pm 1\,psi$). The measured pressures are differential, referenced to the port located at $x/D_h = 59.4$. All data is taken at $10\,Hz$ to avoid any correlation between consecutive samples. Table 4 outlines the placement of the pressure taps along the sidewall of the test section. The pressure taps over the lined region, 62.3–$70.5\,x/D_h$, are connected to smaller range pressure scanner in order to minimize bias errors. The pressure gradient for the hard wall cases is determined using all sixteen pressure ports, while the lined cases use only the nine pressure ports located over the liner.

Table 4. Pressure Tap Locations.

Tap	x/D_h	Scanner Range (Pa)
P3	60.37	6890
P5	61.37	6890
P6	61.87	6890
P7	62.37	2490
P9	63.37	2490
P11	64.37	2490
P13	65.37	2490
P15	66.37	2490
P17	67.37	2490
P19	68.37	2490
P21	69.37	2490
P23	70.37	6890
P24	70.87	6890
P25	71.37	6890
P27	72.37	6890
P29	73.37	6890

4 Facility Characterization

In order to provide confidence in the facility, several aspects of the flow are compared to other square ducts and channels. First, the developing flow region will be briefly described, and comparison to three other studies will be be provided. Next, the velocity distribution in the fully developed flow region will be compared across lines of symmetry. The procedure used to correlate the bulk nozzle Mach number to the test section centerline Mach number will be explained. After that, the distribution of the mean flow and Reynolds stresses in an axially aligned plane on the centerline will be compared to channel flow at a comparable bulk Reynolds number. Finally, the acoustic performance of the anechoic diffuser will be assessed.

4.1 Developing Flow Measurements

The developing flow region in channels and ducts has been assessed experimentally in many studies, with the main intent of determining a criteria for fully developed flow. One such criteria, based on the control volume approach, indicates that a linear pressure gradient indicates a fully developed flow. However, Melling and Whitelaw [32] note that in the developing region, the pressure gradient can still be nominally linear while the velocity profile is changing. It is this redistribution of the momentum through secondary flow that suggests a measurement based on the velocity profile should be used rather than the pressure gradient. While some authors are proponents of more stringent requirements on a fully developed flow, such as the collapse of up to fourth order statistics or spectral collapse [33], the relatively simple condition of constant centerline velocity is proposed instead in order to get a better estimate than the pressure gradient approach without an extensive measurement campaign.

In the developing region, Anselmet [34] has proposed nondimensional parameters to unify several different studies of flow in channels, pipes, and ducts to capture the development of the boundary layers of U_c/U_b against δ_1/D_h. Rather than measuring the displacement thickness at several axial stations, Anselmet suggests that the relationship $\delta_1 \sim xRe_x^{-1/5}$ should be used to replace the displacement thickness. This is based off the assumption of a one-seventh power law for a flat plate, and it is expected that collapse of the data will only exist in the range of Reynolds numbers where it is applicable. Figure 19 shows the development of the GFID along with two other square duct investigations [32, 35], and slope based on Anselmet's own square duct simulations. The data was collected using single component LDV. The GFID appears to exhibit slightly slower development than the other experimental data, although the error bounds are large enough that the experimental data can be said to agree with the GFID measurements. Following the measurement of the centerline velocity development upstream, measurements were taken periodically in order to establish the fully developed flow region. The ratio of the centerline to bulk velocity for the GFID reaches a constant rate by $58.5\,x/D_h$ [24].

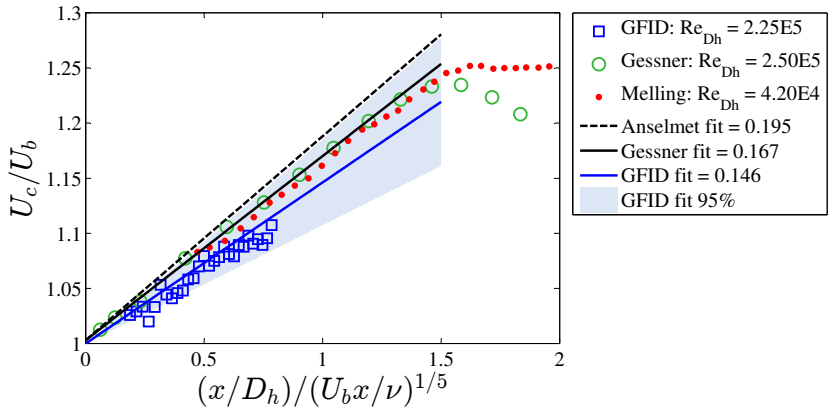

Figure 19. The plot shows the growth of the centerline velocity with increasing axial distance at $Re_b = 2.25E5$, adapted from Bertolucci [24].

4.2 Fully Developed Region Velocity Distribution

The symmetry of the tunnel in the fully developed region is verified through the use of one component LDV. The details of the setup are addressed thoroughly in Bertolucci [24]. A grid of points spaced 2.5 mm apart in both the y and z directions are taken over the central portion of the duct. Figure 20 shows the axial velocity distribution over half of the duct. In order to provide a quantitative measure to the

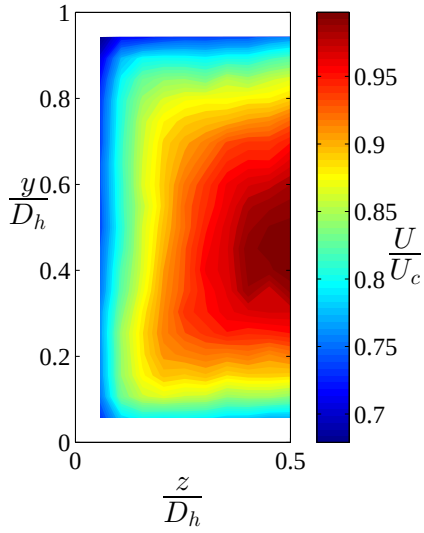

Figure 20. The plot shows the normalized axial velocity over half of the duct for $Re_b = 2.25E5$.

'goodness' of the symmetry, the percent difference in the measured axial velocities with respect to the top–bottom and diagonal symmetry are shown in Figure 21. The majority of locations differ from their respective symmetric points by 5% or less.

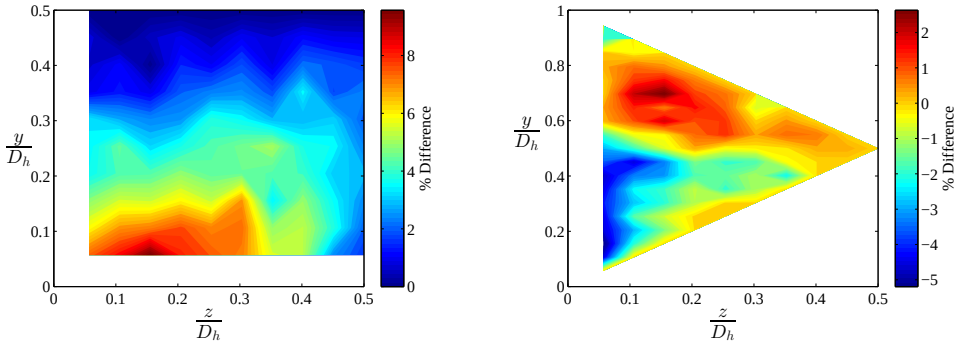

Figure 21. The percent difference in axial velocity when the half duct is checked for top–bottom (left) and diagonal (right) symmetries.

4.3 Pitot Calibration

In order to obtain a correlation in the fully developed region between the centerline velocity, U_c, and the bulk velocity, U_b, a pitot-static tube was placed in the center of the tunnel $60.2\,D_h$ downstream of the nozzle. Based on previous measurements [24], the flow profile at the nozzle is roughly uniform, and the bulk velocity can be assumed to be equal to the velocity determined from isentropic flow equations. The PCA-8-KL probe from United Sensor Corp. presented a blockage of 1.6% to the flow. The sensor has a source of bias error due to the presence of the pitot's stem near the static pressure ports so that the measured dynamic pressure, q, will be approximately 1% lower than the true value [36]. The static and total pressure were measured using a Pressure Systems Model 9116 pressure scanner with a range of $\pm 0.361\,psi$ for low speeds, and $\pm 1\,psi$ at higher speeds. Accuracy of the pressure scanner is quoted as $\pm 0.05\%$ full-scale range [37]. Data was taken over a range of bulk Mach numbers of 0.02-0.3 in steps of 0.005. Five hundred samples were taken at each Mach number, sufficient for convergence of the mean and standard deviation of all measured quantities. The uncertainty in the Mach number is less than one percent for all the points used in the linear fit in both the ordinate and abscissa. Figure 22 is a plot of the centerline test section Mach number as a function of the bulk Mach number. A line is fit over the range $M_b = [0.065\ 0.3]$, with an R^2 value of 0.999, so that

$$M_C = 1.18 M_b - 0.008. \tag{23}$$

As there is a less than 3% difference between the speed of sound at the nozzle and in the test section, the ratio of Mach numbers is equivalent to the velocity ratio to the reported number of significant figures. The near linear relationship is consistent with the behavior of an incompressible turbulent channel flow, as the relationship has only a weak Reynolds number dependency. The slope is also in agreement with other channel flow data as to the ratio of the centerline to bulk velocities in the fully developed region. Comparisons with other square duct experiments have shown that this ratio will vary between 1.1 and 1.2 over the range of Reynolds numbers considered here [34]. At low speeds, the uncertainty in the bulk Mach number is

largely due to bias errors in the static and stagnation pressure transducers.

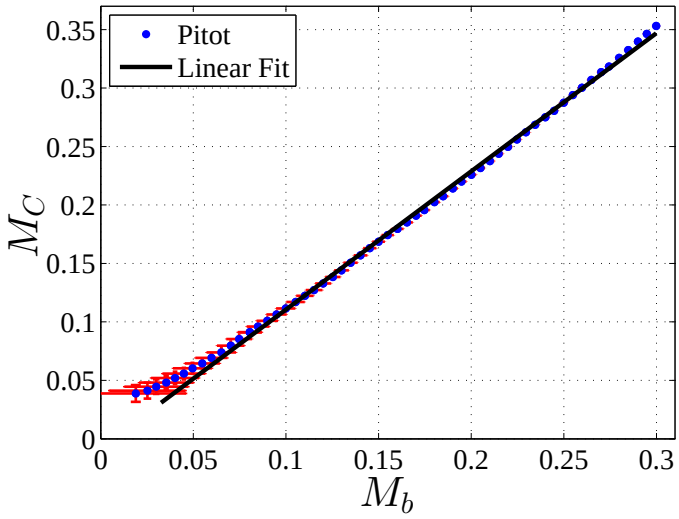

Figure 22. The plot shows a nearly linear relationship between centerline Mach number in the test section as a function of the bulk Mach number.

Knowledge of the centerline and bulk velocity, coupled with a few key assumptions even yields a rudimentary estimate of the shear stress. While this is unlikely to be a viable option for determining the shear stress over an acoustic liner, it nonetheless provides another means of validation of the base flow. For a two dimensional incompressible channel flow, the log-law is valid over a large portion of the channel, and the bulk velocity can be related to the centerline and friction velocities as $\frac{U_0 - U_b}{u_\tau} \approx \frac{1}{\kappa}$ where κ is the von Kármán constant, and the velocity defect at the centerline is assumed to be zero. Pope [38] suggests a relationship between centerline and friction velocity $\frac{U_0}{u_\tau} \approx 5 \log_{10} Re_b$ where Re_b is the Reynolds number based on channel height and bulk velocity. This results in

$$\frac{U_0}{U_b} \approx \frac{5\kappa \log_{10} Re_b}{5\kappa \log_{10} Re_b - 1}. \tag{24}$$

The plot below, Figure 23, shows the velocity ratio as a function of bulk Reynolds number. Zanoun et al. [6] suggest $\kappa = 0.37$ for channel flow at $Re_\tau > 2000$. At low Reynolds numbers, the disagreement is likely due to the flow not being fully developed rather than the slight dependency of κ. At higher Mach numbers, the difference is believed to be attributed to either compressibility effects, wall roughness, or the simplicity of the model.

If it assumed that the measured M_b contains some systematic error, roughness or compressibility, and that the true ratio of bulk to centerline velocity in the test section is given by Equation 24, a corrected bulk Mach number, M_b^* can be recovered by the unweighted least squares fit

$$M_b^* = M_b(0.435 M_b + 0.929) \tag{25}$$

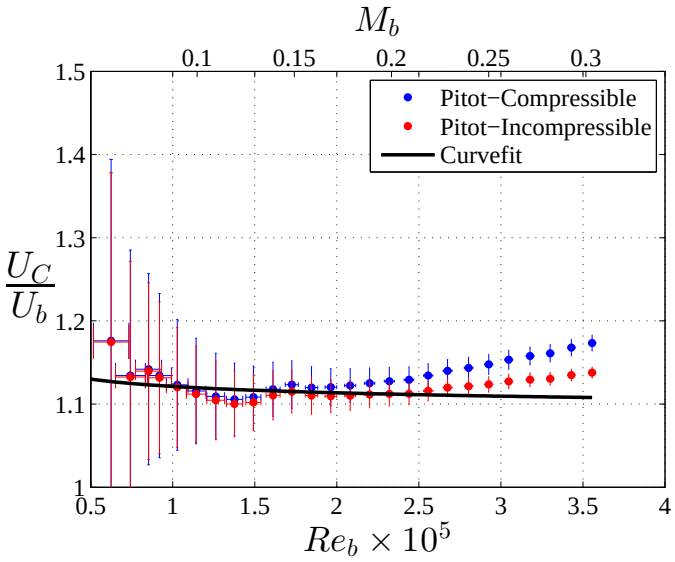

Figure 23. This shows the ratio of the centerline to bulk velocity as a function of the bulk Reynolds number.

over the range of bulk Mach numbers from 0.165 to 0.3 so that the difference in the fitted corrected Mach number differs from the corrected Mach number calculated directly from Equation 24 and the centerline Mach number directly is less than 0.4%.

4.4 Centerline PIV Measurements

A brief look at the PIV results over a hard wall is warranted in an effort to compare general trends of the second order statistics of the data against a study in a channel flow done by Comte-Bellot [39] at $Re_b = 1.2 \times 10^5$. The mean flow will be compared to the log-law in Section 6.2, and this section only compares the Reynolds stress components in a streamwise aligned plane, along with the two point correlation function of the axial velocity fluctuations. The bulk Reynolds number of the data presented here is 1.07×10^5, which corresponds to a centerline Mach number of 0.1, although the friction Reynolds numbers for the two are quite different. For the GFID, the friction Reynolds number is 2300 compared to the channel flow's 5300. The details of the PIV case used for comparison, HWT–S, will be addressed in Section 6.1.

Figure 24 shows a comparison of the axial and wall-normal turbulent stresses along with the turbulent shear stress for the channel flow and the GFID. The GFID statistics for this data set are averaged in time over 2700 snapshots and 250 axial locations. There is general agreement with the trends obtained by Comte-Bellot, although it appears the axial stress is slightly lower for the GFID than the channel flow. This is possibly due to the lack of spatial resolution of the PIV, causing some smoothing of the turbulent fluctuations. The wall normal stress matches quite well across the half duct. Last, the Reynolds shear stress appears to have a more rounded

minima than the channel flow case. It is unclear whether this is due to a bias error, for instance perspective errors from neglecting the out of plane velocity component, or whether this is related to redistribution of the Reynolds stress by the secondary flow.

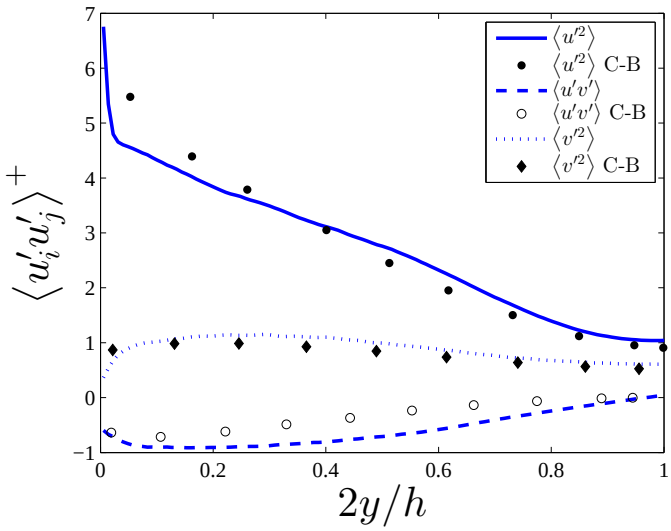

Figure 24. Comparison of the in-plane Reynolds shear stress from the GFID to the work of Comte-Bellot [39].

With regard to the streamwise correlation, the results are presented in terms of the correlation coefficient,

$$\rho_{u,u}(r,y,z) = \frac{\mathcal{R}_{u,u}(r,y,z)}{\sigma_u^2} = \frac{1}{\sigma_u^2}\left\langle u'(x,y,z)u'(x+r,y,z)\right\rangle, \tag{26}$$

where r is the axial separation distance and u' is the fluctuating axial velocity component. Figures 25 and 26 show the correlation coefficient along the centerline of the GFID for various wall normal locations. The channel flow and GFID match up very well over the range of wall normal locations $0.33 \leq 2y/h \leq 0.67$. For the remainder of the duct, the GFID has a longer correlation length near the wall than the channel flow, but a shorter correlation length than the channel near the centerline. The GFID results also appear to have an upward tail at values of separation larger than $2r/h$, which are attributed to the incomplete convergence of the correlation, as there are fewer measurements to average at these spatial separation distances.

The trends of the correlation coefficient as a function of wall normal location are shown in a different format in Figure 27. The correlation length quickly increases to a maximum around 0.05–0.1h, which corresponds roughly to the region where the log-law shows good agreement with the mean axial velocity profile, then slowly decays toward the centerline. This is indicative of the birth of coherent motion near the wall, with subsequent loss of correlation as the structure lifts off the wall and decays. Analysis of the correlations will be addressed further in the later PIV sections.

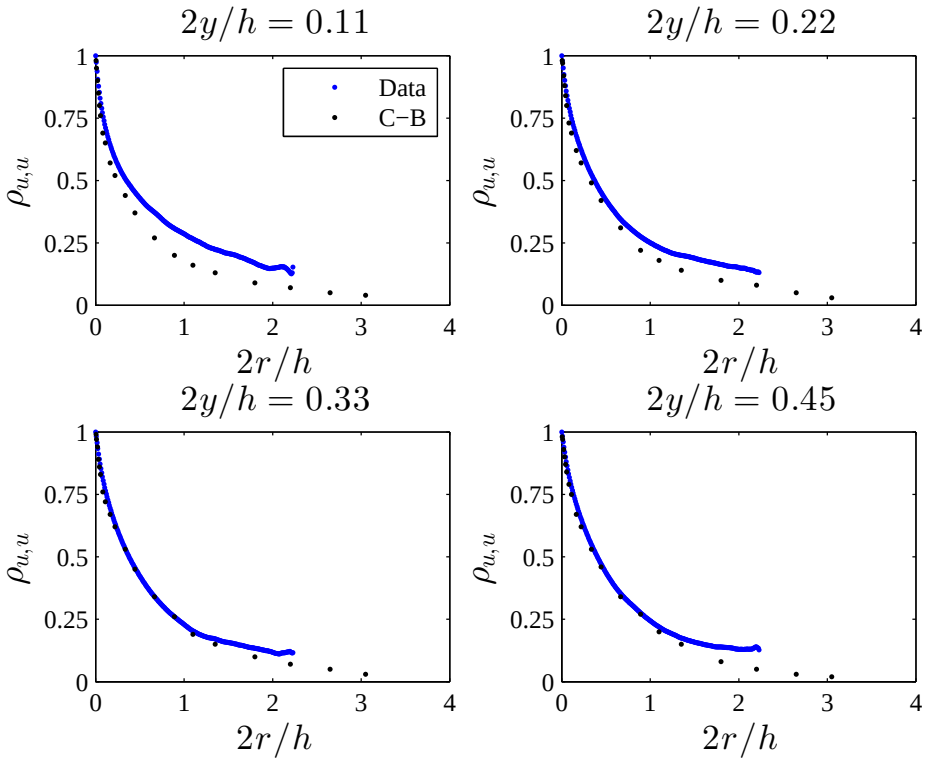

Figure 25. Comparisons of the variation in the wall-normal direction of the correlation coefficient of the axial velocity fluctuations to Comte-Bellot [39].

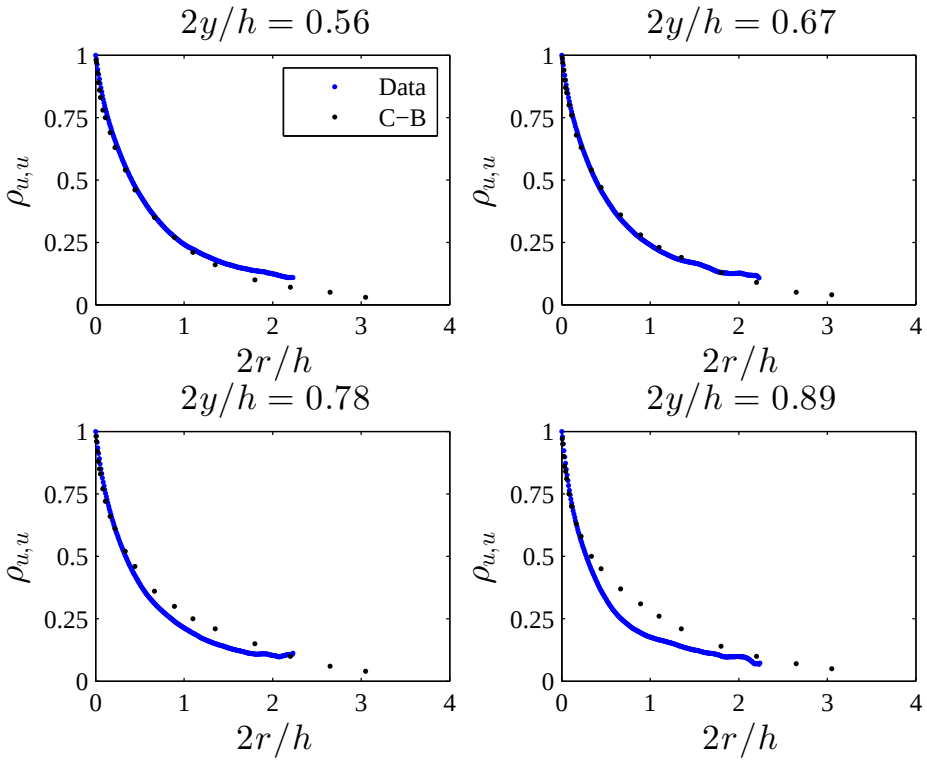

Figure 26. Comparisons of the variation in the wall-normal direction of the correlation coefficient of the axial velocity fluctuations to Comte-Bellot [39].

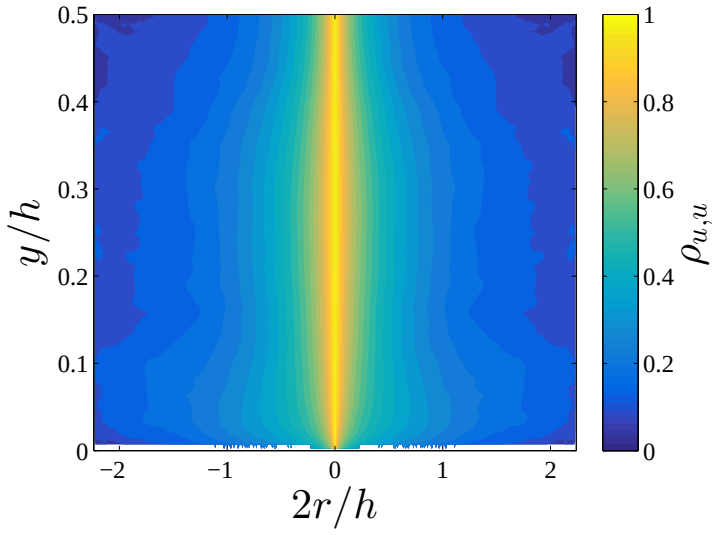

Figure 27. Variation in the wall-normal direction of the correlation coefficient of the axial velocity fluctuations.

4.5 Diffuser Reflection Coefficient

As will be discussed in Section 5.1, the presence of a nonreflecting boundary condition is an assumption utilized in some impedance eduction methods, and so it is necessary to ensure the reflections are low in order to make quality measurements of the impedance. Figure 28 shows the comparison of the reflection coefficient magnitude between the hard walled, fiberglass diffuser to the anechoic termination. The

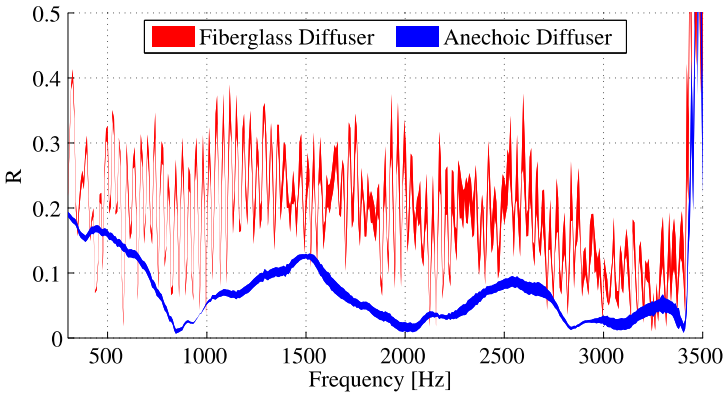

Figure 28. A comparison of the reflection coefficient magnitudes of the fiberglass and anechoic diffusers are shown at quiescent conditions over the usable range of frequencies for plane wave excitation.

reflection coefficient was determined using the two microphone method, using the process described in ASTM Standard E1050-12 [40]. Two microphones, placed in the acoustic plug shown in Figure 6, and mounted in the downstream test port recorded the incident acoustic pressure field. The acoustic test section provided pseudo-random noise from 0.3–3.5 kHz as the excitation source. Further details can be found in Bertolucci [24]. The anechoic diffuser has the expected effect of reducing the amplitude of the reflected acoustics over the entire spectrum. For most of the plane wave region, the reflection coefficient is below 0.1, so that the signal to noise ratio of the incident to reflected pressure amplitude is 20 dB. Significant scatter exists in the results for the fiberglass diffuser, which is likely related to excited structural modes in the diffuser. The thickness of the fiberglass is only 4.5 mm, which evidently is not enough to sufficiently dampen the response. This could be improved in the future by adding additional layers of fiberglass.

5 Liner Acoustic Measurements

This section provides an overview of acoustic liners, the necessary framework to test the impedance of acoustic liners in grazing flow, and the results of impedance testing performed on two test liners. Acoustic liners are characterized by their normal specific impedance, the ratio between the acoustic pressure and local particle velocity. This is typically normalized by the characteristic impedance of the medium [41], $\rho_0 c_0$, so that

$$\zeta(f) = \frac{p}{v\rho_0 c_0} = \theta + \jmath\chi. \tag{27}$$

In general, ζ is complex valued with the real part or resistance denoted by θ, and the imaginary part or reactance, χ. The acoustic liners studied herein are Helmholtz resonator arrays. A Helmholtz resonator is simply a small opening or neck exposed to the flow at the orifice, with a cavity behind the neck. Figure 29 shows a typical resonator with a face sheet thickness, t, orifice diameter, $\mathcal{D}$, and cavity height, $\mathcal{H}$. A lumped element model can be used to predict the frequency dependence of the

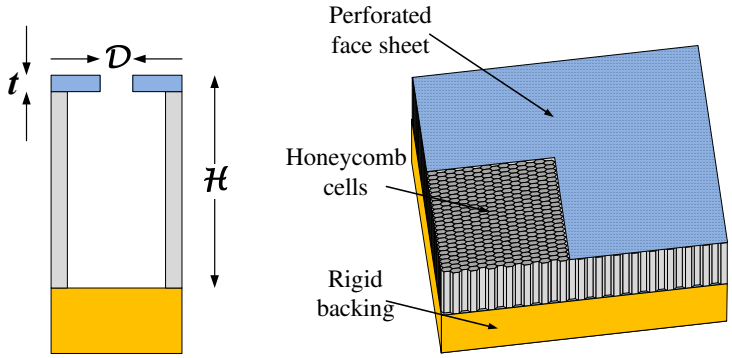

Figure 29. The picture to the left shows the cross-section of a single Helmholtz resonator, while the cartoon on the right shows an array of resonators or acoustic liner.

acoustic liner, such as the two-parameter model [41,42]. The resistance is composed of three terms: flow losses through the channel in the neck, dump losses due to vorticity production, and the interaction between the turbulent boundary layer and the resonator. The resistance depends on a discharge coefficient, C_D, loss coefficients K_i and K_e, and the ratio of open area of the orifices to total area, σ. The reactance has only two terms: the mass of fluid oscillating in the neck, and the reactance of a transmission line with one end closed. The reactance corresponding to the back cavity manifests primarily as a compliance as the fluid in the cavity is compressed and expanded. The neck reactance is a function of the perforate thickness as well as an additional fictional length known as an end correction, ϵ. This compensates for the radiation impedance into the flow outside of the resonator. The lumped impedance as a function of frequency [41] is

$$\begin{aligned}\zeta(f) =& \left[\frac{32\mu t}{\rho_0 c_0 \sigma C_D \mathcal{D}^2} + \frac{K_i + K_e}{2c_0(\sigma C_D)^2} v_{rms} + \frac{M_C}{3\sigma}\right] \\ &+ \jmath\left[-\cot\left(\frac{2\pi f \mathcal{H}}{c_0}\right) + \frac{2\pi f(t + \epsilon\mathcal{D})}{\sigma C_D}\right],\end{aligned} \tag{28}$$

where the end correction is

$$\epsilon = \frac{0.85(1 - \sqrt{\sigma})}{1 + 305M_C^3}. \tag{29}$$

This model will be used to validate the impedance measurements of two acoustic liners in Section 5.2.

The normalized specific acoustic impedance is useful in duct acoustics as it is an intrinsic property of the liner and is implemented as a boundary condition when solving for acoustic propagation in a duct. With respect to the liner's interaction with the flow, it is anticipated that the effect will be enhanced near the liner's resonance, when the velocity at the orifice should be maximized for a given pressure input.

5.1 Methodology

The convected wave equation in rectangular coordinates for uniform flow in a square duct is

$$\frac{\partial^2 P}{\partial z^2} + \frac{\partial^2 P}{\partial y^2} + \left(k - M\frac{\partial}{\partial x}\right)^2 P - \frac{\partial^2 P}{\partial x^2} = 0, \tag{30}$$

where the x, y, and z directions correspond to the axial, transverse, and spanwise coordinates of the duct, respectively. For the case at hand, the duct has three sound-hard walls and a single finite impedance boundary on the bottom of the duct. The sound-hard walls constitute homogeneous Neumann pressure boundary conditions in the wall normal direction, while the impedance boundary condition is mixed, and is a statement of continuity of particle displacement at the wall. The source is located upstream, and the nonreflecting boundary condition limits the wave propagation to the downstream direction alone, so the pressure field has an axial dependance of the form $e^{-\jmath k_x x}$. The axial wavenumber for a given mode is related to the spanwise, transverse, and free-space wavenumbers through the dispersion relationship

$$k_y^2 = (k - k_x M)^2 - k_x^2 - k_z^2. \tag{31}$$

In the homogenous spanwise direction, the wavenumber is constrained to $k_z = \frac{\pi n}{h}$, where n is an integer. Provided the excitation frequency is below the cut-on of the first higher order mode, the acoustic pressure will be constant in the spanwise direction and k_z disappears from Equation 31. The aforementioned impedance boundary condition,

$$k_y \tan(k_y h) = \frac{\jmath k}{\zeta}\left(1 - M\frac{k_x}{k}\right)^2, \tag{32}$$

provides the link between the liner impedance and the wavenumber components.

With this equation, if the axial wavenumber can be determined, the unknown impedance can be educed. Due to the complex exponential dependency of the pressure in the axial direction, the real and imaginary components of the axial wavenumber are

$$\mathbb{R}(k_x) = \frac{d\phi}{dx} \tag{33a}$$

and

$$\mathbb{I}(k_x) = \frac{1}{20\log_{10}(e)}\frac{dP_{SPL}}{dx}, \tag{33b}$$

where ϕ is the phase of the acoustic wave relative to a single axial location and P_{SPL} is the pressure amplitude in dB SPL. Thus, the impedance can be determined in the presence of a single dominant mode using an axial microphone array to capture the pressure amplitude and phase decay. This procedure is aptly named the single mode method (SMM). However, there are several limitations to the procedure outlined above. Notably, a gross simplification of the flow to that of a uniform distribution limits the applicability to low Mach numbers, where the effects of shear are limited. Further, there must be only a single dominant mode over the acoustic liner in order to reliably determine the axial wavenumber. Finally, the problem is outlined for a nonreflecting semi-infinte duct, meaning an anechoic diffuser is needed to prevent strong reflections.

In order to relax the restriction of a single mode, the KT-Prony method [43] can be used to identify multiple axial wavenumbers that may be superimposed using the same amount of information needed for the single mode method. The pressures at each axial location, p_n, are a summation of the contributions of M axial modes so that

$$p_n = \sum_{i=1}^{M} B_i e^{-\jmath k_{x,i} dx\, n} = \sum_{i=1}^{M} B_i z_i^n. \tag{34}$$

The exponentials have residues B_i and complex wavenumbers $k_{x,i}$, and the pressures are measured with equal spacing, dx. These exponentials can be compactly represented as complex poles, z_i and their residues. A characteristic polynomial, $f(q)$, having roots at each z_i can be constructed as

$$f(q) = \prod_{i=1}^{M}(q - z_i) = \sum_{i=0}^{M} \gamma_i q^i. \tag{35}$$

From the constraints on the polynomial from Equation 35, γ_M is defined as unity. $N - M$ linearly independent equations can be built from the polynomial in order to estimate the M coefficients,

$$\sum_{i=0}^{M} B_i z_i^t f(z_i) = 0, \quad t \in [0, 1, \ldots, N - M - 1]. \tag{36}$$

This series of equations can be written in terms of the known pressures and the coefficients of the polynomial. After solving the system of equations, a complex

root solver is used to determine the poles. In turn, the poles are transformed into the axial wavenumbers as

$$k_{x,i} = \frac{\jmath \ln z_i}{dx}. \tag{37}$$

The impedance can then be recovered using Equations 31 and 32. The susceptibility of Prony's method to noise has been widely documented. However, the KT-Prony method reduces the effects of noise by performing the singular value decomposition on the pressure matrix used to solve for the polynomial coefficients. This improves the scaling of the problem by removing the smallest singular values, which are most associated with measurement noise.

5.2 Results

The testing procedure, outlined in Section 3.1, covers all of the data acquisition and input uncertainties in the measurements used in the eduction of the acoustic impedance but did not address the parameters for the KT-Prony method or the approach for obtaining the uncertainty in the impedance. For the KT-Prony algorithm, the SVD threshold for removing small singular values was set to be -15 dB with respect to the largest singular value. The assumed number of poles was set to be 5.

In order to estimate the uncertainty in the liner impedance, Monte Carlo simulations were carried out until the liner impedance population was converged. It was found that 20,000 samples was more than sufficient to achieve convergence of the mean and standard deviation of the impedance populations. The perturbed inputs were the sound pressure level and relative phase of each microphone, with uniformly distributed systematic errors of ± 0.2 dB and $\pm 0.1°$, respectively. The Mach number and speed of sound are considered constant due to the low amount of variation in the sampled values. The error bounds shown in the following plots are 95% coverage intervals, which due to the Gaussian nature of the impedance distribution, are simply ± 1.96 standard deviations about the mean value.

5.2.1 L1 Results

Liner L1 is tested at quiescent conditions as well as $M_b = [0.1,\ 0.3,\ 0.5]$. The computed impedance for these conditions are presented in Figure 30. General trends to be gathered from these plots are the poor performance at low frequencies, lower resistance than the model with flow, and relatively good agreement of the model and measured reactance. The larger error bars at low frequency are due to the low levels of attenuation away from resonance. The disagreement of the measured resistance with the model is likely due to the differences in the many empirical constants used in the model. The coefficient of discharge, as well as the loss coefficients are dependent on the hole geometry. The values of $C_D = 0.76$ and $K_i + K_e = 1$ are used in this paper. The grazing flow correction, the third term in Equation 28 and denominator of Equation 29, is based on empirical modeling by Rice [44]. Predictions of the resonant frequency are within $100\,Hz$ of the two parameter model. The KT-Prony method performs better than the SMM in several cases, especially at low frequencies.

It does however usually have a larger coverage interval than the SMM. At $M_b = 0.5$, the breakdown of the plug flow assumption at higher Mach numbers occurs.

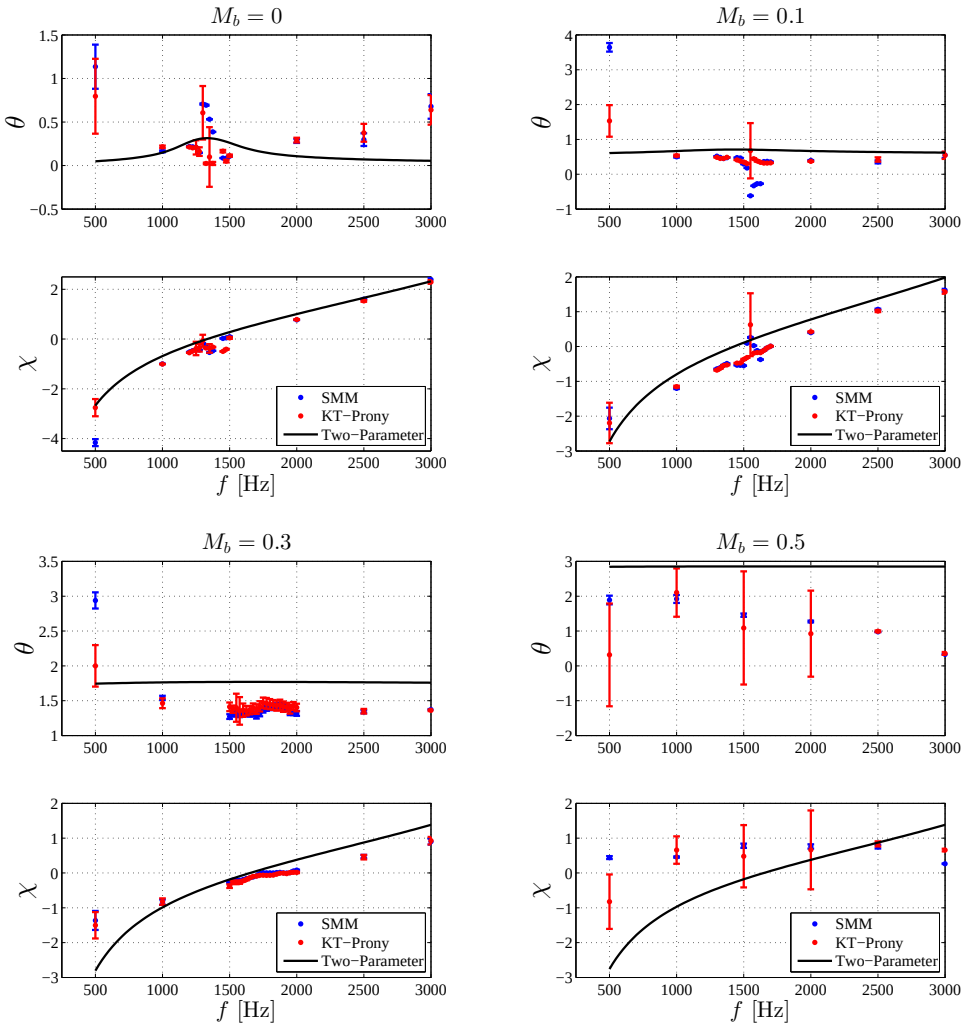

Figure 30. The resistance and reactance of the L1 liner are presented at several Mach numbers. The top left and right are at quiescent conditions, and a bulk Mach number of 0.1, respectively. The bottom left and bottom right plots correspond to bulk Mach numbers of 0.3 and 0.5.

Table 5. L1 Resonance.

M_b	Predicted $[Hz]$	Measured $[Hz]$
0	1330	1450
0.1	1430	1675
0.3	1650	1800
0.5	0.8	–

5.2.2 L2 Results

The L2 liner was tested at quiescent conditions as well as test section centerline Mach numbers of 0.1 and 0.3. This corresponds to a bulk Mach number of 0.091 and 0.26 measured at the nozzle exit. The results are displayed in Figure 31. Unexpectedly, the majority of the resistance values for the $M_b = 0.1$ case are smaller than their quiescent counterparts. Further, there is a noticeable shift of approximately $500\,Hz$ of the reactance between the model and measurements. Also, the frequency corresponding to the maximum attenuation at $M_C = 0.1$ is $2175\,Hz$ more closely matches the modeled resonant frequency than the measured value of $2700\,Hz$ where there is much less attenuation. These effects have been noted in a similar liner at a separate facility [42]. That liner has a porosity of 13%, face sheet thickness of $0.81\,mm$, hole diameter of $2.36\,mm$, and honeycomb depth of $38.1\,mm$. It has been postulated that the poor agreement at the lower Mach numbers is at least partially due to the point that the liner has a low resistance, and low attenuation across the spectrum. This is especially visible at the low and high frequencies. When the resistance increases at $M_b = 0.3$, the measurements and model improved markedly.

Table 6. L2 Resonance

M_C	Predicted $[Hz]$	Measured $[Hz]$
0	2200	2725
0.1	2280	2700
0.3	2900	3300

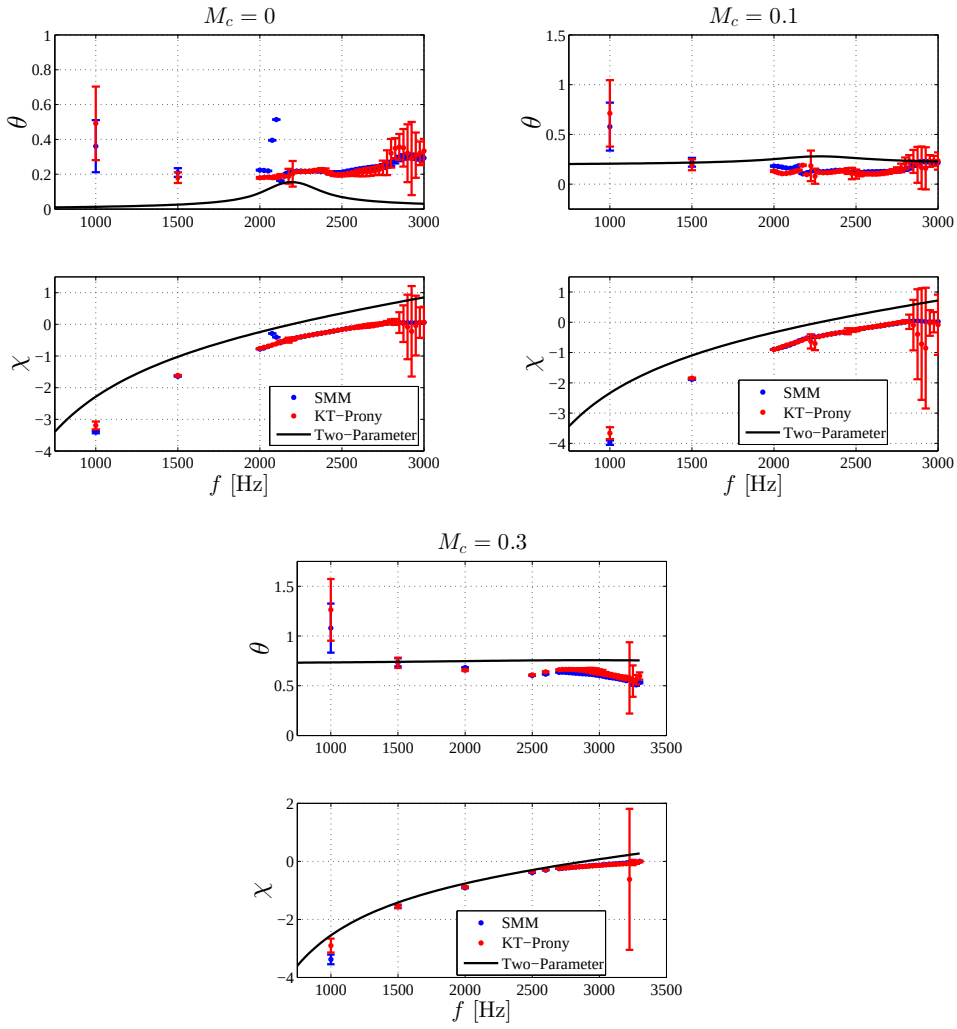

Figure 31. The resistance and reactance of the L2 liner are presented at several Mach numbers. The top left and right are at quiescent conditions, and a centerline Mach number of 0.1, respectively. The bottom plot corresponds to a centerline Mach number of 0.3.

6 PIV Data

The main effort of the PIV measurements is to gain a better understanding of the near-wall behavior of the flow over an acoustic liner. In order to do so, it was desired that sufficient spatial resolution in the boundary layer could be attained, and that acoustic excitation should have a nontrivial effect on the flow. Both of these conditions led to the restriction of low Mach number, and a majority of the measurements were focused around $M_C = 0.1$.

6.1 Case Descriptions

Table 7 outlines some of the pertinent information for each of the cases. The spatial resolution l^+ is normalized by wall units. In the liner cases, this is normalized by the hard wall friction velocity rather than the value for the specific liner case. For the hard wall cases, the integral parameters were determined by obtaining an average profile by homogeneity in the axial direction and integrating Equations 15. For the lined cases, the integral parameters were obtained from a single profile taken at $x/D_h = 65.1$, which is the nearest orifice upstream of the location of the CWSSS patch. Due to the asymmetry of the liner CWSSS insert, there were two choices of axial station to compare results. It should be made clear that for the cases over the liner, the patch was in the downstream configuration, so that it would not impact the measurements being taken in the upstream location. The upstream location was chosen for the cases taken over the patch due to concerns that the sound pressure level might be too low at the downstream end to have an impact on the mean flow, especially for the maximum attenuation cases.

The purpose of the CWSSS patch cases are twofold; they are used to provide directly comparable measurements to the CWSSS, and are also used to provide an estimate to the error due to measuring the liner shear stress over a hard wall patch rather than directly over the liner. Accordingly, the profiles used for calculating the integral parameters, as well as the plots to follow for the patch cases are taken at $x/D_h = 65.328$, which corresponds to the location of the CWSSS floating element. The patch resonance case is only a single phase, corresponding to 90°, with the goal being to show the relative accuracy for each type of acoustic forcing rather than to detail the behavior of the flow over the hard wall patch as a function of phase. In all acoustic forcing cases, the SPL of the tone or OASPL over the broadband input range at the reference microphone is 140 $\pm$1 dB. For the attenuation cases, the reference microphone consistently lagged its calibrated expected phase of 7°, while the resonance cases only exhibited a lag of 2°. This was due to slight changes in the speed of sound and flow speed.

Table 7 shows that for hard wall cases, the shape factor is marginally lower than each of the liner cases, indicating that the hard wall profile is 'fuller' than the liner profiles. The random uncertainty in the axial velocity was calculated for a hard wall case and resonance case using the method described in Wieneke [45]. The uncertainty increased nearer to the wall for both cases, and the resonance case had a slightly higher range of values than the hard wall case. The random uncertainty in the mean axial velocity values over the entire field were less than

Table 7. PIV Case Information.

Name	Descriptor	l^+	$\delta_1[mm]$	$\delta_2[mm]$	$\mathbb{H}$	Location $\left(\frac{x}{D_h}\right)$
Hard Wall, Upstream	HWU	11	3.28	2.44	1.34	65.04–65.22
	HWU–2C	52				64.97–65.68
Hard Wall, Downstream	HWD	11	3.19	2.41	1.32	67.41–67.58
	HWD–2C	55				67.26–67.98
Hard Wall, Upstream, 2–C	HWT	10	3.21	2.41	1.33	65.03–65.20
	HWT–S	41				64.92–66.04
Liner L2, Baseline	L2B	11	3.25	2.37	1.37	65.02–65.20
	L2B–2C	49				64.96–65.67
Liner L2, Broadband	L2BB	12	3.61	2.53	1.43	65.02–65.20
	L2BB–2C	53				64.96–65.67
Liner L2, Resonance	L2R	10	3.59	2.47	1.46	65.02–65.20
	L2R–2C	43				64.96–65.66
Liner L2, Attenuation	L2A	12	3.40	2.42	1.40	65.02–65.21
	L2A–2C	54				64.96–65.66
Patch L2, Baseline	P2B	12	3.23	2.40	1.35	65.24–65.41
	P2B–2C	53				64.96–65.65
Patch L2, Broadband	P2BB	12	3.57	2.54	1.40	65.24–65.41
	P2B–2C	54				64.96–65.65
Patch L2, Resonance	P2R	12	3.74	2.56	1.45	65.24–65.41
	P2R–2C	54				64.96–65.41

$0.5\,{}^{m}/_{s}$, corresponding to an uncertainty in the shape factor of about ± 0.03. The resonance case has the highest shape factor of the liner cases, indicating that effects of periodic blowing and suction at the wall are influencing a larger region of the boundary layer than the other cases.

6.2 Hard Wall Baseline Case

Three hard wall cases are compared, with the HWU and HWT cases at the axial station $65.1\,x/D_h$, and the HWD case at $67.5\,x/D_h$. The upstream and downstream velocity profiles are used to further show that the flow is nominally fully developed, as well as to provide a baseline for comparison to the hard wall cases. The HWT case is taken in order to check some of the trends seen in the HWU case in the buffer region, as well as to provide an expanded streamwise extent to capture the decay of the streamwise correlation function, which was shown in Section 4.4.

The mean axial centerline velocity for the three cases is presented in Figure 32. Small differences in the tunnel conditions lead to a range of friction Reynolds numbers of 2300–2400. The friction velocity was determined using a least squares curve fit to the Spalding profile [20]. Good collapse of the mean centerline profile is seen between the upstream and downstream station, as well as with the log-law. Some scatter is present in the buffer region, which is more sensitive to measurement errors. Specifically, the deviation of the HWT–S results in the buffer region are related to uncertainty in the pixel displacement which is small near the wall for the stitched

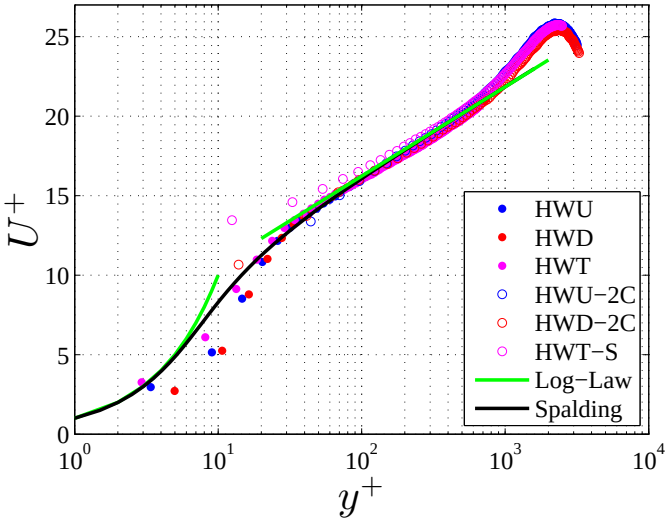

Figure 32. The velocity profiles along the centerline of the two axial stations are presented for comparison. The green line nearest the wall is the linear velocity profile expected in the viscous sublayer, while the outer line is the log-law.

setup. The primary intention of this setup was to capture the velocity field in the bulk flow region, where the displacement is larger.

The Reynolds stress components normalized by the square of the friction velocity and averaged over the domain are shown in Figures 33, 34, and 35. The collapse of the axial Reynolds stress is not as good as for the mean flow. The downstream location has a lower peak magnitude around, $y^+ = 15$, than the two data sets taken at the upstream station. This may indicate that the flow is not strictly fully developed, in that the higher order statistics have not yet converged in the streamwise direction. Doherty et al. [33] indicate that this does not occur until 80 D_h, and their data show the variance is higher at lower values of x/D_h, except near to the beginning of the duct where the boundary layers have not yet converged. This is in agreement with the higher values of streamwise Reynolds normal stress seen at the upstream location. The effects of the spatial resolution can be seen near the outer region of the HWU–2C and HWD–2C data sets. This manifests through the appearance of an outer peak, as noted by Hutchins et al. [46]. The effects are not visible on the HWT–S case, which has a marginally better spatial resolution.

From the axial momentum equation under the assumption of fully-developed two-dimensional flow, the behavior of the Reynolds shear stress in the log-law region [47] is

$$-\left\langle u'v'\right\rangle^+ = 1 - \frac{y^+}{Re_\tau} - \frac{1}{\kappa y^+}. \tag{38}$$

This allows for a quick verification that both the peak location and value are near the expected values. The analysis indicates that a minimum value of $\langle u'v'\rangle^+ \approx -0.93$ should occur at $y^+ \approx 75$. The minimum values of the data are between $-0.66 > \langle u'v'\rangle_p^+ > -0.89$ at a location of $350 < y_p^+ < 600$. The difference in

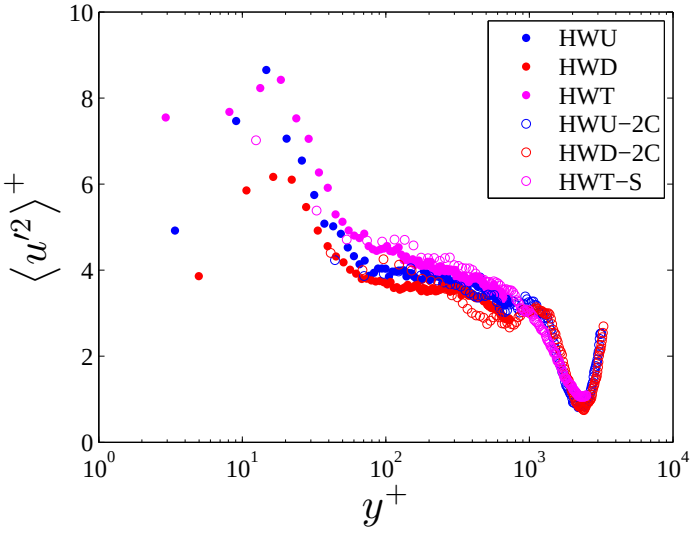

Figure 33. The axial normal Reynolds stress is shown for the three hard wall cases.

the expected peak location is likely due to finite Reynolds number effects [48] or secondary flow effects. There is an issue with capturing the expected near-wall wall-normal Reynolds stress for the HWU case, which was a part of the rationale behind the change in setup for the HWT setup. From the improvement in the resulting Reynolds stress distribution, it is apparent the deviation was due to an issue in the HWU stereo setup. Overall, the HWT and HWD wall-normal Reynolds stresses follow the expected trends, increasing in magnitude at a slower rate with wall normal position than the other Reynolds stress components, and peaking at a value of unity.

The behavior of the hard wall cases shows that while the mean statistics are converged, there is still some slight development occurring in the higher order statistics. It is important then to compare profiles in the liner case that have been taken at the same axial station.

6.3 Liner Baseline Case Single Point Statistics

This section presents the results for the liner baseline case. All of the liner plots of single profiles are extracted at the same axial station as the upstream hard wall data at 65.1 x/D_h, approximately half an orifice diameter downstream of a liner perforation. The mean velocity profile at this location, compared to the hard wall data is shown in Figure 36. Differences in the friction velocities of the two cases lead to the presentation of the baseline case in terms of two scalings, which are based on its own friction velocity and that of the hard wall case. The suffix of HW has been added to those cases that are normalized by the hard wall friction velocity. With respect to the L2B case, the inner region remains relatively similar to the HWT case, but the slope of the log layer is slightly higher. This is similar to the behavior of a porous wall with continuous blowing, as indicated by Stevenson [49]. However,

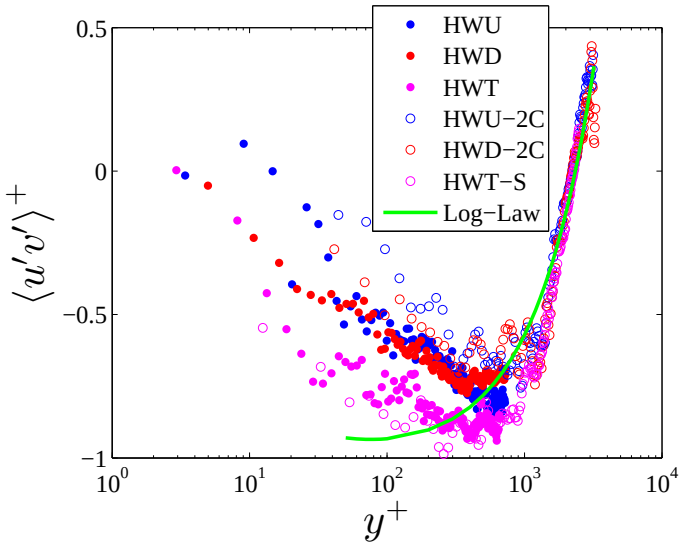

Figure 34. The in-plane Reynolds shear stress is shown for the three hard wall cases.

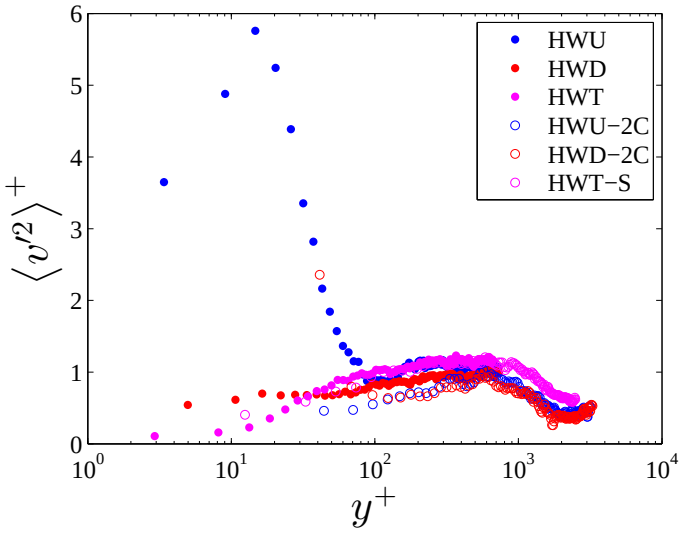

Figure 35. The wall-normal Reynolds stress is shown for the three hard wall cases.

when there is no forcing at the wall, the modification to the log-law proposed by Stevenson is zero and the profile should collapse to the log-law for a hard wall. The difference in the profile is believed to be due to natural excitation of flow in and out of the orifice by the grazing flow. When the baseline case is normalized by the hard wall friction velocity, a slight velocity deficit from the log law is present until $y^+ \approx 400$, which leads to the higher shape factor values shown in Table 7.

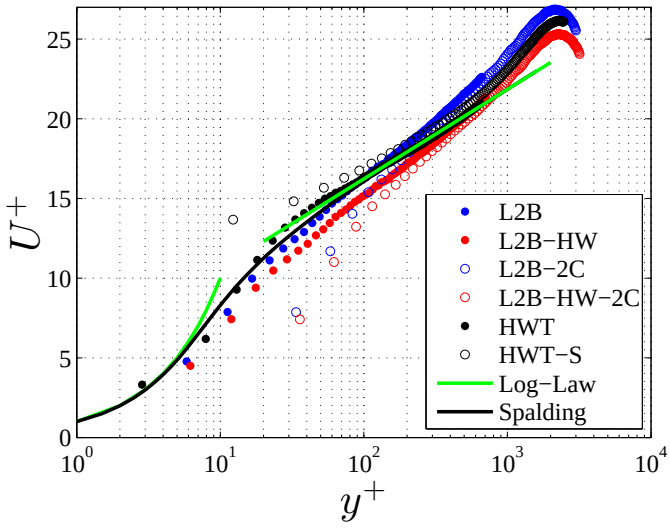

Figure 36. A comparison of the baseline liner case (L2B) to the hard wall case (HWT) and theory-based curve fits. The green line nearest the wall is the linear velocity profile expected in the viscous sublayer, while the outer line is the log-law. The black line represents the composite Spalding profile.

For the remaining plots of any liner and patch cases, the wall normalization is by the hard wall friction velocity values, unless stated otherwise. Accordingly, the HW suffix is dropped from the plots for convenience. In Figures 37 and 38, there is general agreement with the hard wall case. There is a slight increase of the axial Reynolds stress in the L2B case over the HWT case at $y^+ \approx 200$, as well as some increased scatter in the Reynolds shear stress.

In Figure 39, the wall normal Reynolds stress for both cases is shown and a peak is present in the liner baseline case, as well as a general increase over the hard wall case near the wall. It is believed that the increased values of the wall normal Reynolds stress are related to turbulent fluctuations out of the orifice. The fluctuations into the flow tend to lift the low momentum fluid upward. Downstream of the orifice, the wall boundary is solid, removing the source of continued upward motion so that the dominant transport mechanism is streamwise convection. A plot of the wall normal stress over the entire domain, Figure 40, suggests that the peak does not continually move farther from the wall, but rather stays constant in magnitude and distance from the wall in the regions before and after the orifice. The low momentum fluid brought to this point is then convected downstream and mixed with the high momentum fluid above it. The mixing process diffuses the

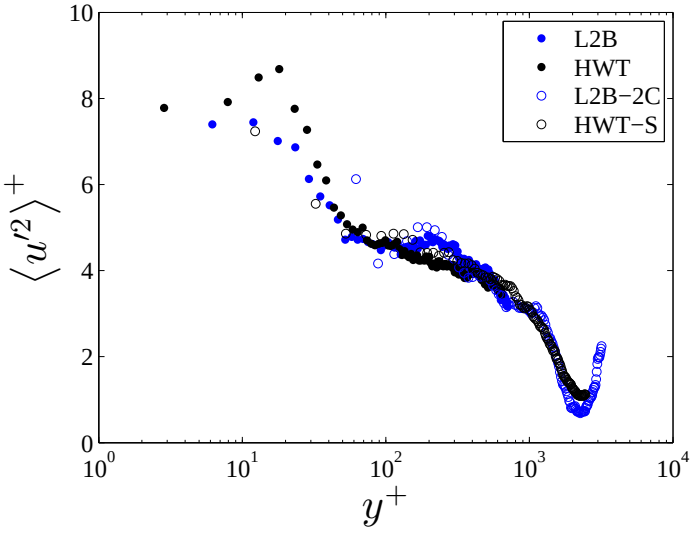

Figure 37. A comparison of the axial Reynolds stress for the baseline liner case to the hard wall case.

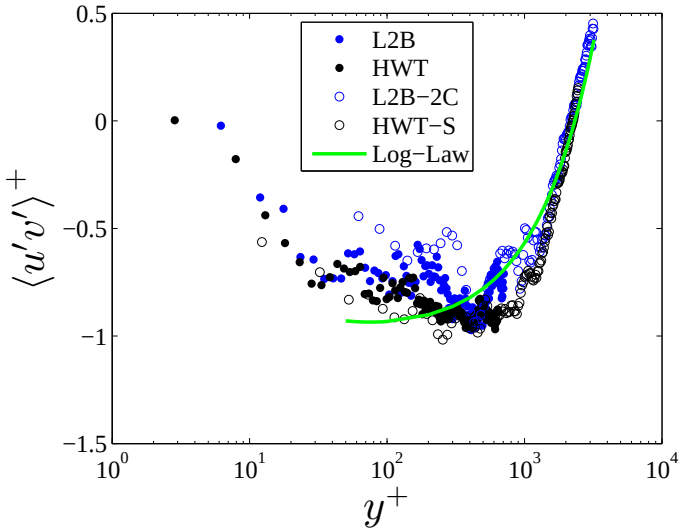

Figure 38. A comparison of the Reynolds shear stress for the baseline liner case to the hard wall case.

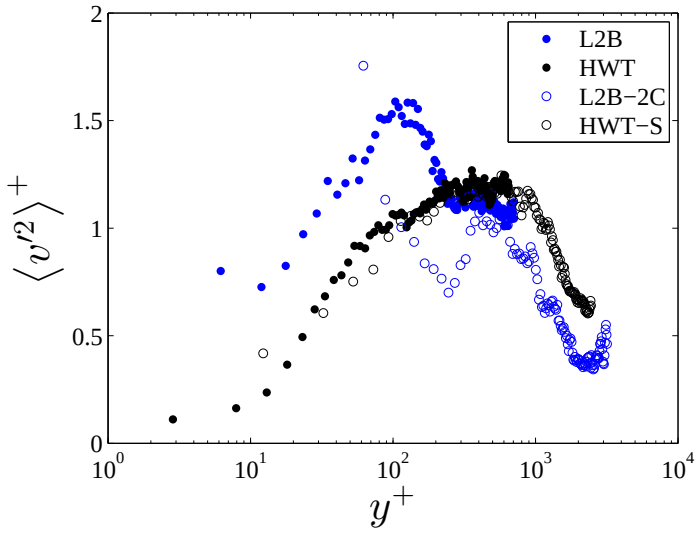

Figure 39. A comparison of the wall-normal Reynolds stress for the baseline liner case to the hard wall case.

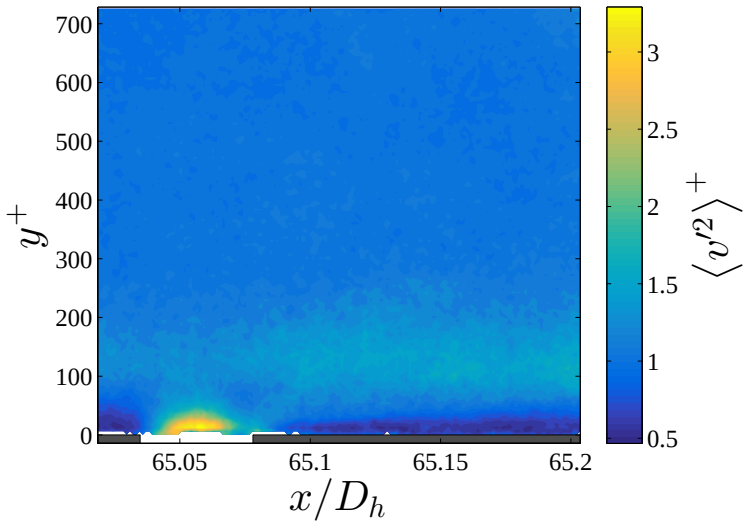

Figure 40. The wall-normal Reynolds stress for the baseline liner case is shown for the entire domain. A layer of high stress is visible across the domain.

momentum of the fluid at a slower rate than it is convected downstream, elongating the region of high stress in the axial direction.

6.4 Liner Broadband Case Single Point Statistics

This section addresses the statistics of the broadband case, beginning with a comparison of the mean velocity profile, shown in Figure 41. This shows a larger velocity deficit than the baseline case. The slope of the broadband case in the outer region is also slightly higher than the baseline case.

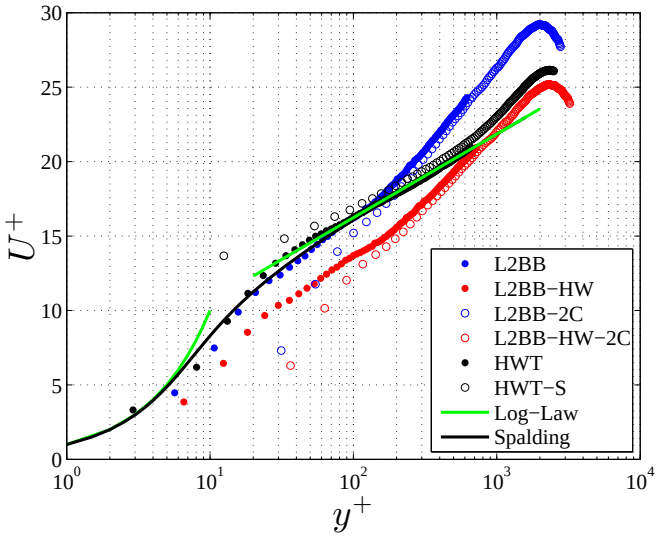

Figure 41. A comparison of the broadband liner case (L2BB) to the hard wall case (HWT) and theory-based curve fits. The green line nearest the wall is the linear velocity profile expected in the viscous sublayer, while the outer line is the log-law. The black line represents the composite Spalding profile.

The Reynolds stresses for the broadband case, seen in Figures 42, 43, and 44, show the same relative trends as the baseline case, except that the differences with the hard wall case are much more exaggerated. The location of the peak in the wall normal stress for this case has moved slightly farther from the wall, and the range of wall normal locations has broadened.

6.5 Attenuation Case Single Point Statistics

Phase-locked PIV for eight cases were collected with acoustic forcing at the frequency of maximum attenuation for the liner, with each case spaced 45° apart. The frequency of maximum attenuation was chosen from the fluctuating pressure data from the impedance eduction experiment at the same Mach number, with the attenuation being the difference in sound pressure level at the upstream and downstream end of the microphone array. The phases were chosen to correspond with the period of the acoustic pressure at the axial station of the orifice. However, due to the finite

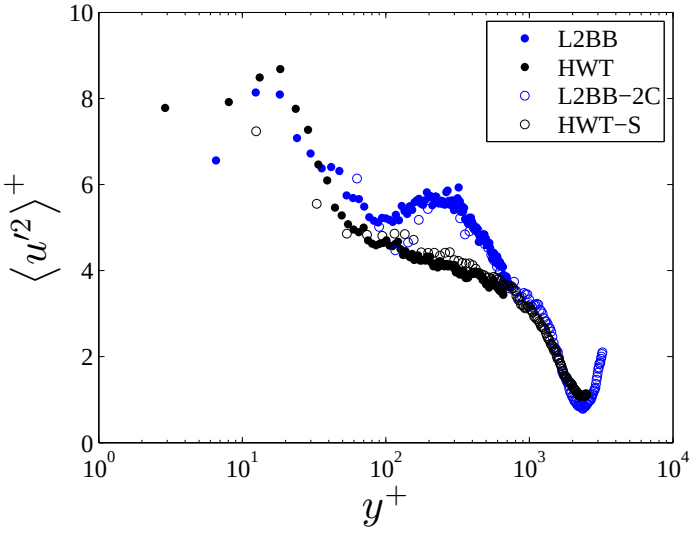

Figure 42. A comparison of the axial Reynolds stress for the broadband liner case to the hard wall case.

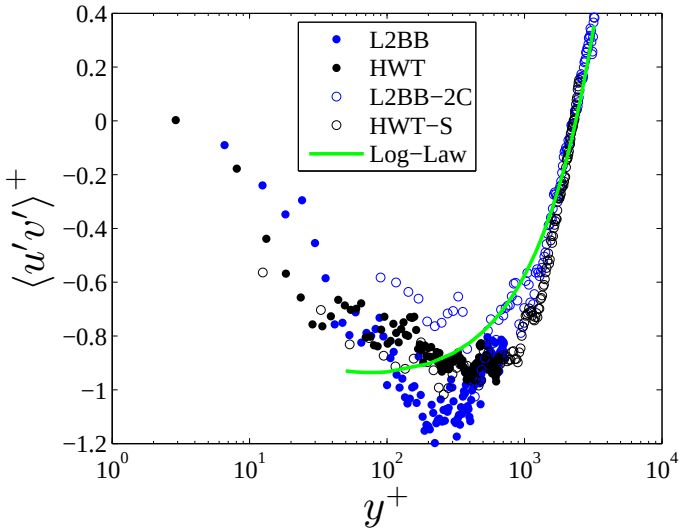

Figure 43. A comparison of the Reynolds shear stress for the broadband liner case to the hard wall case.

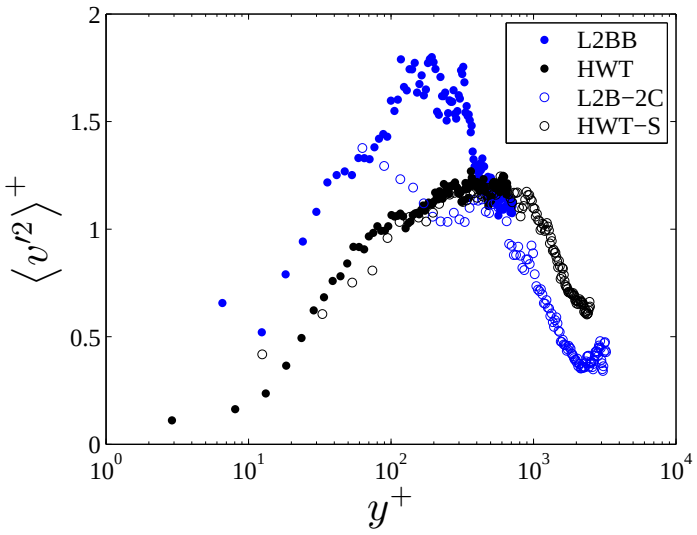

Figure 44. A comparison of the wall-normal Reynolds stress for the broadband liner case to the hard wall case.

component of reactance at the tested frequency, the velocity in and out of the orifice is not in phase with the pressure. Knowledge of the resistance and reactance at the desired frequency, obtained in Section 5.2, allows for determination of the phasing between the pressure and velocity. The impedance eduction results indicate that the velocity should lead pressure by $72° \pm 1°$ at $2175\,Hz$. For a flow with a periodic fluctuating component, a triple decomposition is performed so that, for instance, the measured axial velocity u is

$$u = \overline{u} + u' = \overline{u} + \tilde{u} + u''. \tag{39}$$

The periodic fluctuating component is $\tilde{u}$, while the uncorrelated velocity fluctuations are u''. Together, these two make up the total contribution to the fluctuations from the mean velocity. For the case at hand, the acoustic forcing is sinusoidal, and the periodic fluctuating component, for the moment, is assumed to be so as well. When the phase averages are used to determine the ensemble averaged rms fluctuations, there is a bias introduced in the measurement if the phase averages used are not in even increments, or are not aligned with the start of the acoustic forcing period. As the phases are not aligned with the velocity at the orifice, the shifted phases will lead to an increase in the rms averaged periodic fluctuating component.

The periodic fluctuating velocity component is plotted in Figure 45. The streamwise spacing of adjacent orifices is about $4.5\,\mathcal{D}$. It shows the expected phase lead of the velocity compared to the pressure, with the maximum outflow from the orifice occurring for the $\phi = 0°$ case. However, the maximum outflow does not correspond to the $\phi = 180°$ case. Two possible explanations are presented. The first is that the physics are only weakly influenced by the acoustics at this particular frequency, and the phase dependency is simply noise. The magnitude of the velocity in and out of the orifice is not much larger than the broadband or baseline cases. However,

the second explanation is that the jetting is dominated by the first harmonic of the attenuation frequency. The first harmonic at the reference microphone has a magnitude of 120 dB. While this is not nearly as strong of an amplitude, it is twice the frequency. Dependance of the reduction in wall shear stress on the wall normalized excitation frequency, $f^+ = f\nu/u_\tau^2$ has been shown to increase with increasing f^+ for periodic blowing [50]. It is possible then that the orifice show a preference to this harmonic frequency due to receptivity to higher f^+, or perhaps to the impedance presented to the orifice by the harmonic. This could be verified in the future by insertion of a microphone in the wall of the cavity behind the orifice.

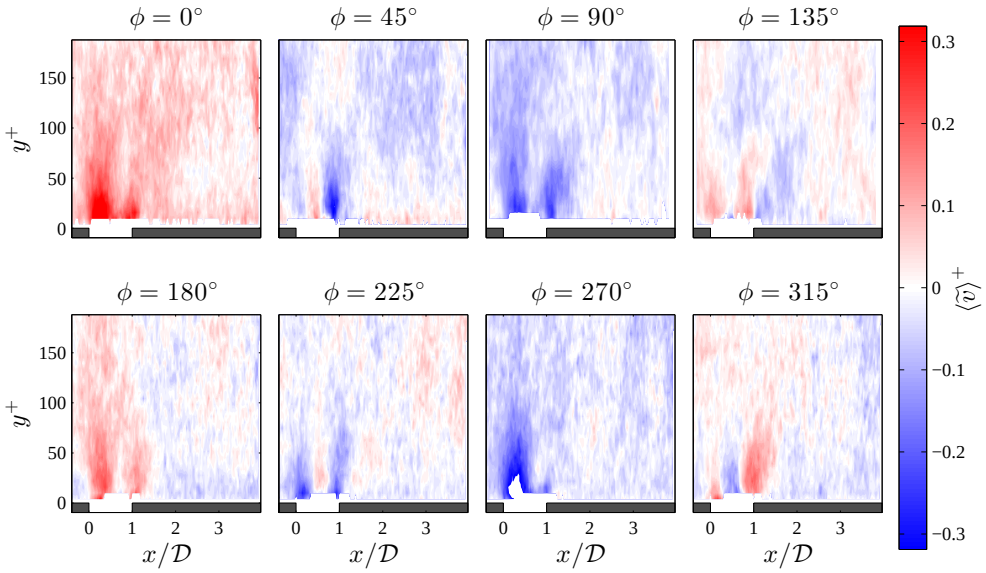

Figure 45. The phase averaged fluctuating wall-normal velocity for the attenuation cases, normalized by hard wall friction velocity, is shown for each phase.

The mean axial velocity averaged across all phases for the attenuation case is depicted in Figure 46. The shape of the attenuation case profile is very similar to the broadband case in both the size of the velocity deficit and slope. The Reynolds stresses, Figure 47, are likewise similar to the broadband case, except that the peak in $\langle v'^2 \rangle^+$ reaches a higher value of around 2.5 compared to the broadband case which is about 1.8.

When the mean axial velocity profile is plotted for each of the eight phases, Figure 48, the profile is seen to be invariant to the phase. This is echoed by the Reynolds stress profiles plotted for each phase in Figure 49 which overlay one another to a large degree, except for slight differences near the wall of a few phase cases.

6.6 Resonance Case Single Point Statistics

Next, the phase-locked resonance cases are analyzed. First, a comparison of the time averaged mean resonance case is compared to the hard wall and log law in Figure 50. A large deficit is seen in the resonance case, with the mean profile affected all the way

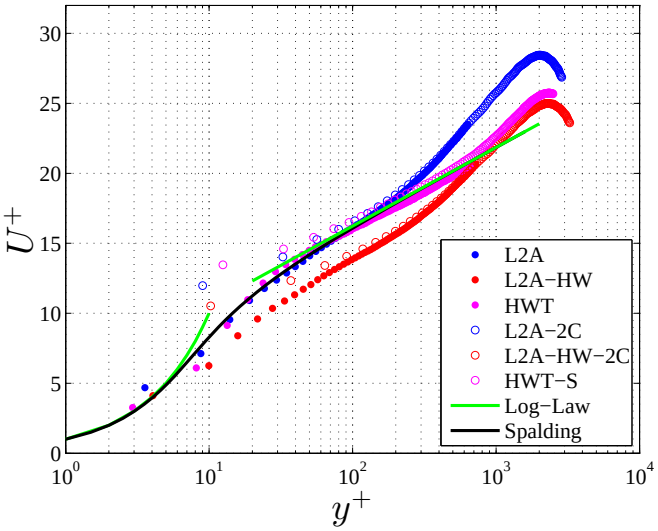

Figure 46. The attenuation case, with hard wall and local friction velocity scaling, is compared to the hard wall case and theory-based curve fits. The green line nearest the wall is the linear velocity profile expected in the viscous sublayer, while the outer line is the log-law. The black line represents the composite Spalding profile.

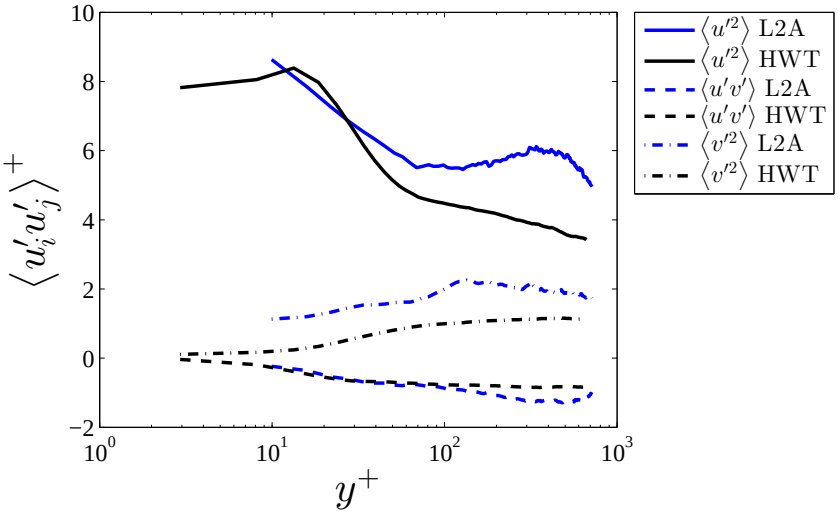

Figure 47. The attenuation case, scaled by the hard wall friction velocity, is compared to the hard wall case.

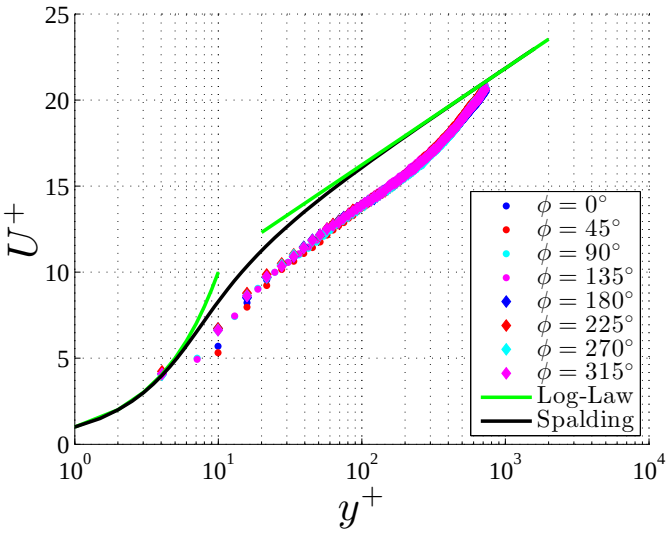

Figure 48. The mean profile for attenuation cases, normalized by the hard wall friction velocity, on a phase averaged basis are compared to a log law profile for reference. The green line nearest the wall is the linear velocity profile expected in the viscous sublayer, while the outer line is the log-law. The black line represents the composite Spalding profile.

to the outer wake region. The slope of the profile is also higher than the baseline, broadband, and attenuation cases, which implies a higher blowing velocity at the wall. With regard to the average Reynolds stresses, there is a dramatic increase in the wall normal stress across the entire inner and log layer. Figure 51, shows that the entire boundary layer exhibits levels in excess of the maxima of the hard wall case. Consistent with the other cases, there is a peaking of the shear stress and streamwise normal stress farther from the wall than the wall normal peak.

Next, a comparison is taken at the same axial location for each phase separately in Figure 52. Differences arise in the inner region until $y^+ \approx 100$, which corresponds to the peak location of wall-normal Reynolds stress shown in Figure 53. The phase cases during the ingestion half of the cycle, especially for the $\phi = 180°$ and $\phi = 225°$ cases, have depressed streamwise velocities near the wall. This is believed to be caused as the boundary layer is lifted upward during ejection pushing low momentum fluid farther away from the wall. This low momentum fluid is convected downstream to the axial station where the profiles are taken during the suction portion of the cycle, resulting in the reduced mean phase averaged axial velocities. This fluid that is pushed away from the wall also appears to manifest in the Reynolds stress plots. There is reduced streamwise Reynolds stress in the near wall region for the suction phases, and the wall-normal Reynolds stress is elevated near the wall as the region of high stress present over the orifice during ejection is convected downstream to the profile location during the suction cycle. This argument only takes into account the behavior of the velocity field along the centerline, and it is cautioned that although the explanation given is a strong candidate, it is likely that the three-dimensionality

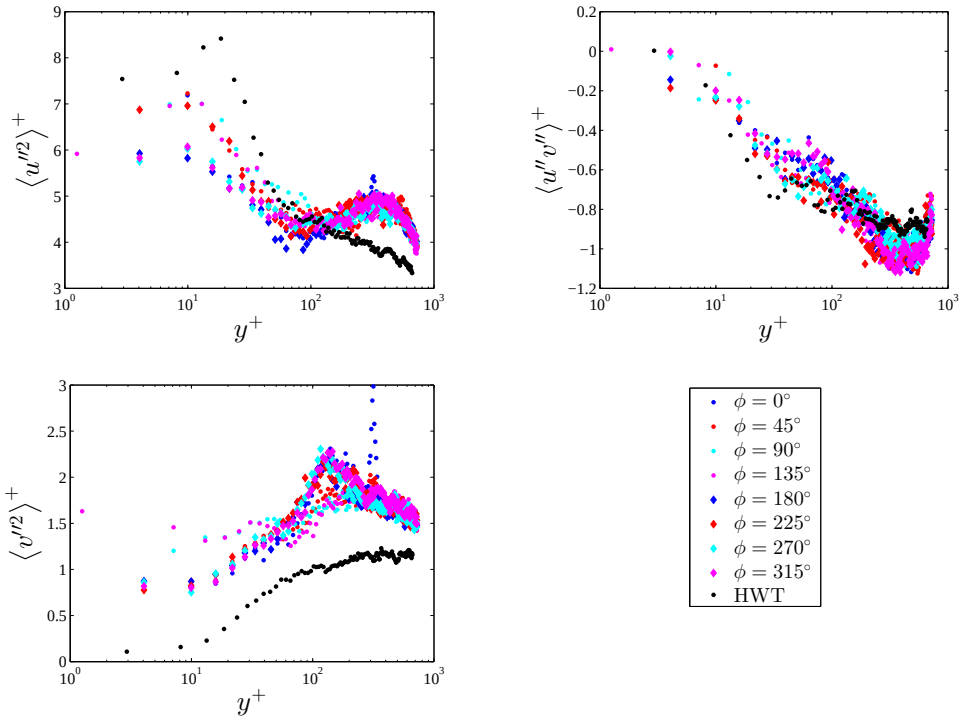

Figure 49. Reynolds stresses for the attenuation cases are shown at the axial station approximately one half hole diameter downstream, normalized by the hard wall friction velocity. The top left is the axial normal stress, top right is the in-plane shear stress, and bottom left is the wall-normal normal stress.

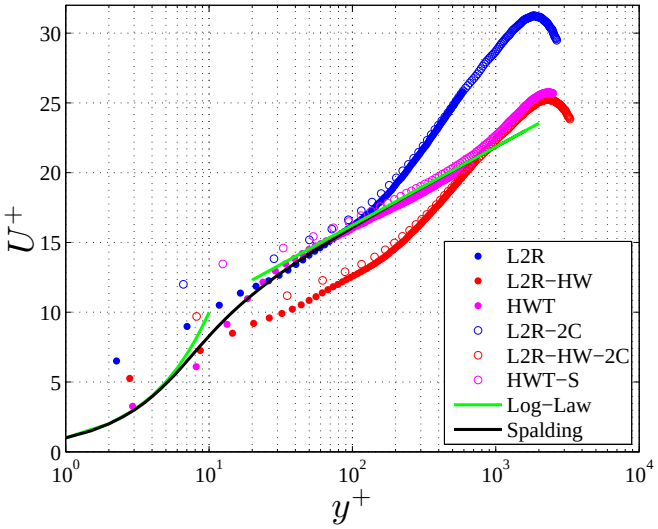

Figure 50. The resonance case, with hard wall and local friction velocity scaling, is compared to the hard wall case and theory-based curve fits. The green line nearest the wall is the linear velocity profile expected in the viscous sublayer, while the outer line is the log-law. The black line represents the composite Spalding profile.

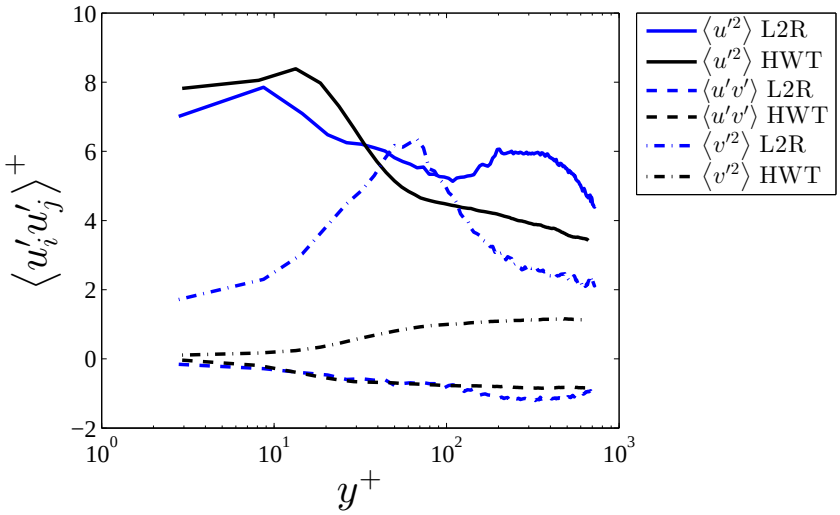

Figure 51. The resonance case, scaled by the hard wall friction velocity, is compared to the hard wall case.

of the flow behind an orifice, as well as effects from neighboring orifices play a role in the true physics.

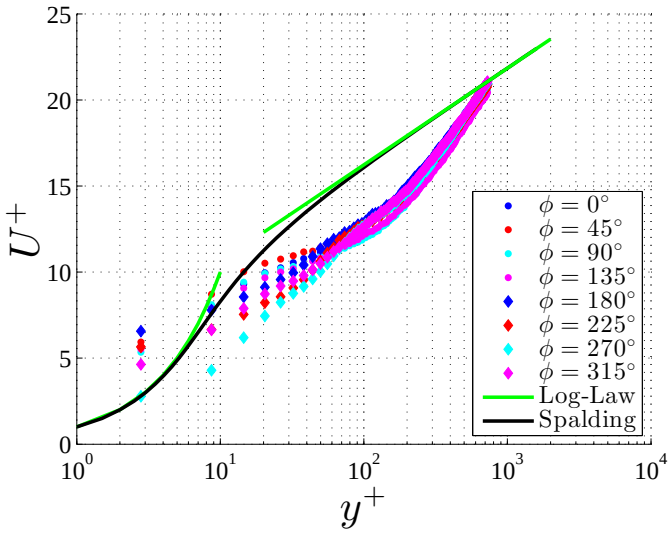

Figure 52. The mean profile for resonance cases, normalized by the hard wall friction velocity, on a phase averaged basis are compared to a log law profile for reference. The green line nearest the wall is the linear velocity profile expected in the viscous sublayer, while the outer line is the log-law. The black line represents the composite Spalding profile.

Figure 54 shows the periodic component of the wall normal velocity. These profiles show a much different shape than the uniform forcing used in simulations [21]. There is reasonable antisymmetry to the velocity profile at the opposing phase, with the suction as large in magnitude as the injection. The reader should be reminded of the disparity of the scales in the phase plots to follow. The field of view in the wall normal direction is roughly a quarter of the field of view in the axial direction. There is apparent stretching in the wall normal direction which is a product of the figure scaling, rather than the physics of the flow.

Plots of the Reynolds stress at each phase shown in Figure 55 also exhibit some periodicity, with the regions of strong Reynolds stress corresponding to regions of low Reynolds stress for the opposing phase. The Reynolds shear stress as a function of phase, presented in Figure 56 has a different behavior. There is a region of positive turbulent shear stress above the orifice at zero phase, which appears to convect upward to $y^+ \approx 100$ before dissipating. This region of positive turbulent shear stress aligns well with the axial locations where the periodic wall normal component switches sign.

The wall normal stress, in Figure 57, shows a consistent streak of high stress across the entire domain which is broken down only near the orifice. The layer is centered over $y^+ \approx 75$, except for the $\phi = 180°$ and $\phi = 225°$ cases.

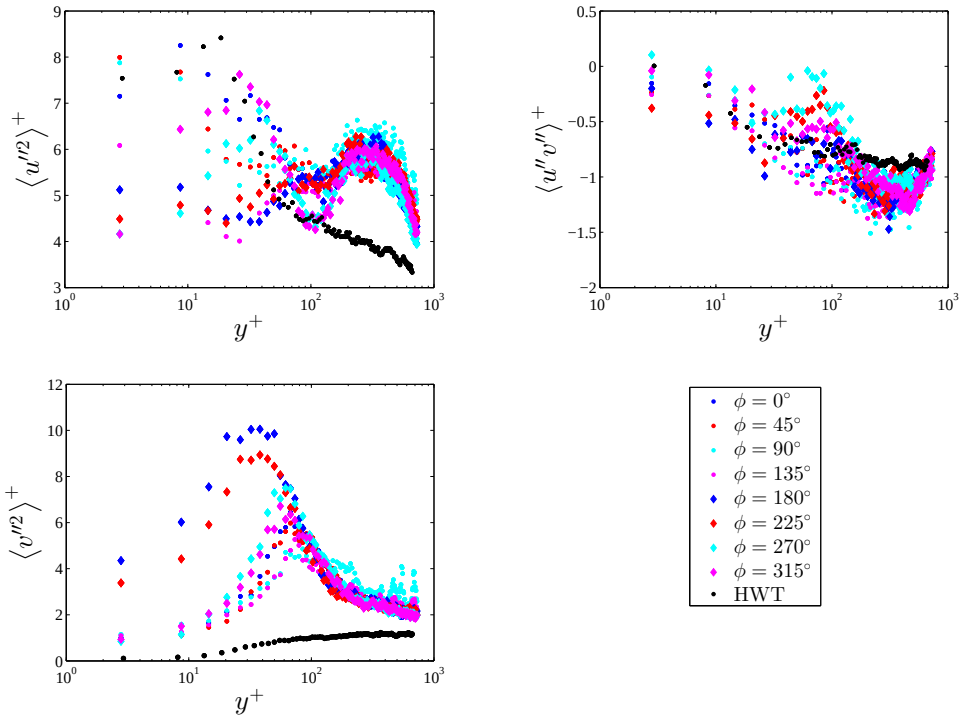

Figure 53. Reynolds stresses for the resonance cases are shown at the axial station approximately one half hole diameter downstream, normalized by the hard wall friction velocity. The top left is the axial normal stress, top right is the in-plane shear stress, and bottom left is the wall-normal normal stress.

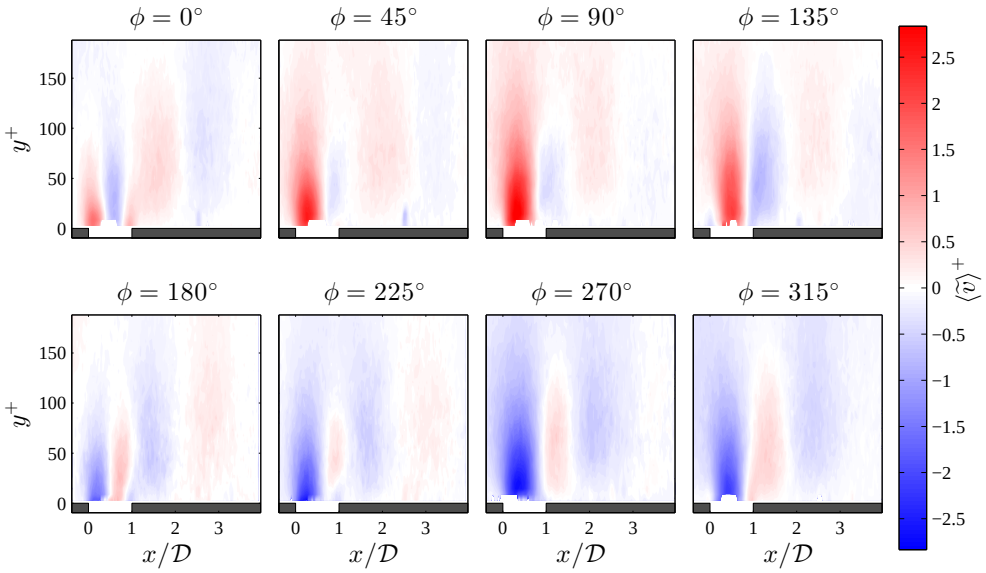

Figure 54. The phase averaged fluctuating wall-normal velocity, normalized by hard wall friction velocity, is shown for each phase.

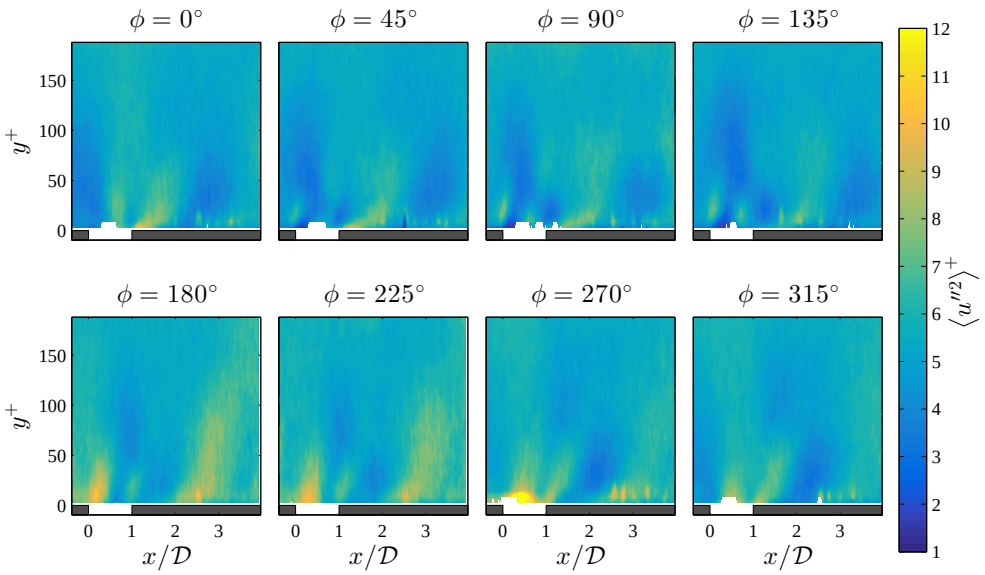

Figure 55. The streamwise Reynolds normal stress for the resonance cases, normalized by hard wall friction velocity, on a phase averaged basis are compared to the hard wall case.

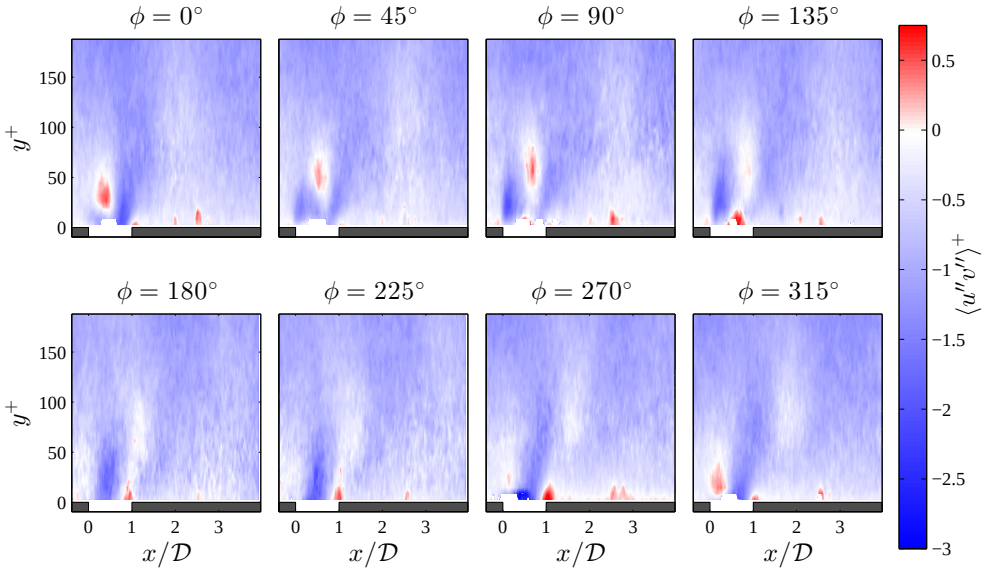

Figure 56. The in-plane Reynolds shear stress for the resonance cases, normalized by hard wall friction velocity, on a phase averaged basis are compared to the hard wall case.

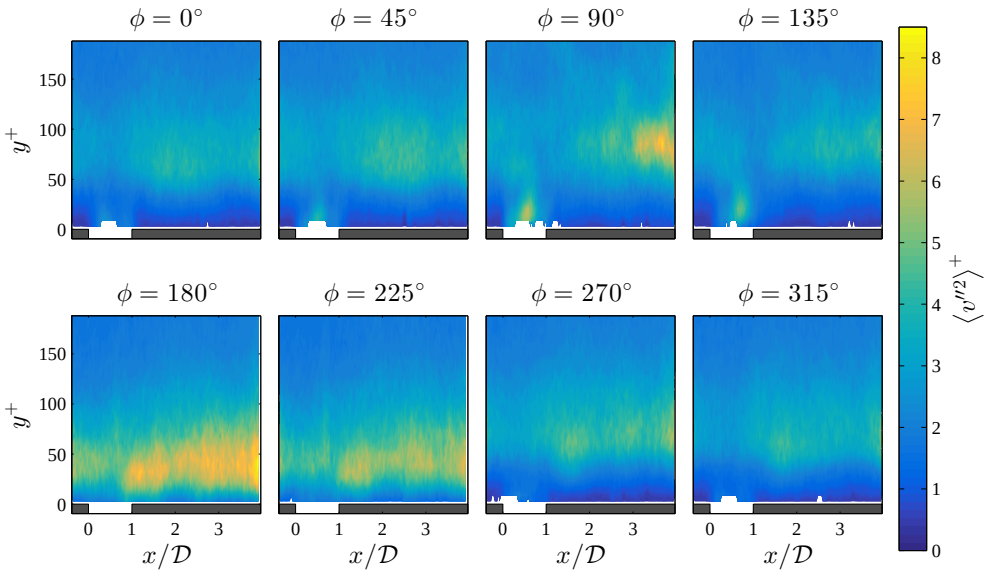

Figure 57. The wall-normal Reynolds normal stress for the resonance cases, normalized by hard wall friction velocity, on a phase averaged basis are compared to the hard wall case.

6.7 Patch Single Point Statistics

The patch cases are proposed to provide guidance on how intrusive the measurement of the wall shear stress via the CWSSS would be. Three cases are chosen, each with a different type of acoustic forcing. The comparison of the mean profile over the sensor patch for the baseline case is compared to the liner baseline case in Figure 58. While there is collapse of the two profiles for $y^+ > 30$, near the wall there is some disagreement, which indicates that the measured wall shear stress will be different for the two cases. However, this only results in a difference of 2% between the two cases. This is partially due to the procedure to curve-fit, which uses several points in the region where the velocity profiles overlap. Unfortunately, there is insufficient spatial resolution to obtain multiple points is the viscous sublayer.

Figure 59 shows similar results for the broadband case. The differences between the two profiles only extend up to the buffer region. The difference in the measured wall shear stress is 6% for the broadband case, slightly higher than that of the baseline case. The results for the resonance case follow the same basic trends as the other cases and the associated figures are omitted for brevity. The development of the wall shear stress over the field of view for the patch cases show a steady rise in the friction velocity. Figure 60 shows the development of the friction velocity over the patch. The friction velocity, even by the end of the field of view only increases by 5% over the value determined for the L2BB case. This level of agreement shows that reasonable estimates of the wall shear stress can be achieved using a shear stress sensor with this size package. This is advantageous because single point measurements using a wall shear stress sensor could allow for quick measurement of a sample under a variety of conditions, eliminating the need for boundary layer

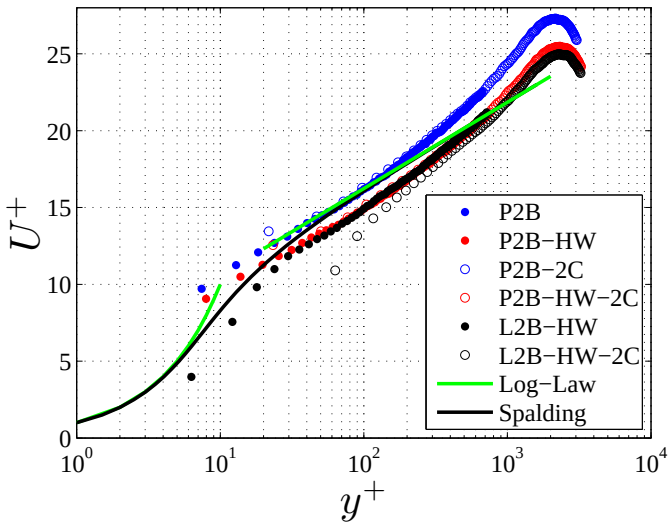

Figure 58. The baseline case for the liner and patch are compared, along with the Spalding profile and log law for reference to the hard wall condition. The green line nearest the wall is the linear velocity profile expected in the viscous sublayer, while the outer line is the log-law. The black line represents the composite Spalding profile.

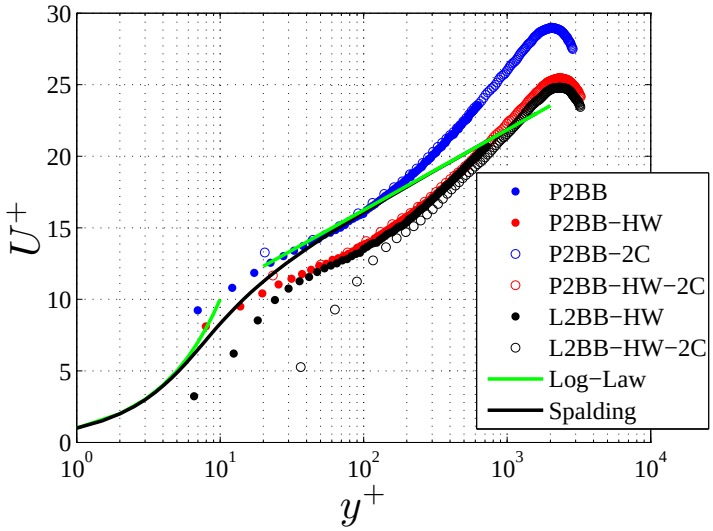

Figure 59. The broadband case for the liner and patch are compared, along with the Spalding profile and log law for reference to the hard wall condition. The green line nearest the wall is the linear velocity profile expected in the viscous sublayer, while the outer line is the log-law. The black line represents the composite Spalding profile.

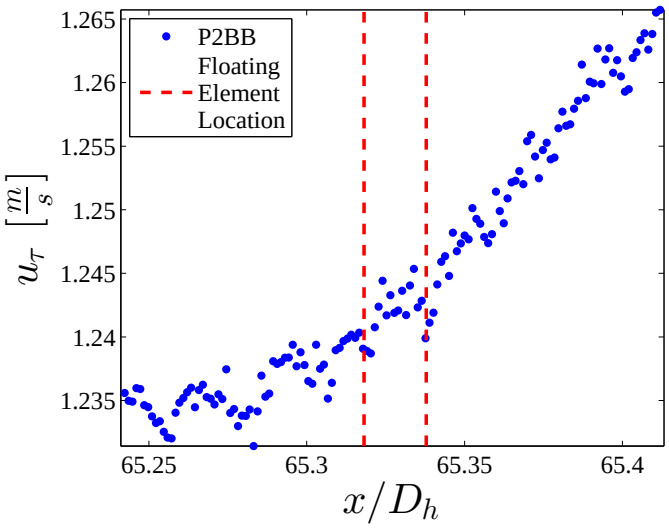

Figure 60. The friction velocity calculated at each axial station in the broadband patch case is shown, along with the bounds of the sensor floating element.

traverses and the additional modeling uncertainties that come along with indirect wall shear stress measurement.

6.8 Pressure Gradient and Control Volume Method Concerns

In order to estimate the wall shear stress using the axial pressure gradient, assumptions of a fully developed flow and negligible momentum flux through the orifices are made. This section addresses those assumptions by analysis of the L2R case in order to indicate whether such assumptions are justifiable. Literature on measuring the contribution through the orifices is quite limited, apart for Kong [11], who measured the wall-normal fluctuations using a hot-wire placed 1.59 mm behind the surface of a perforate liner with no acoustic forcing. He noted the rms fluctuations were a near constant 0.4% of the free stream velocity up to 58 m/s. While this value is relatively small, the liner had a low porosity of approximately 4% and a high hole aspect ratio of 4.4. The case at hand centers on a liner with a aspect ratio of 0.4 and a porosity of 12.7%, and is therefore expected to have a stronger effect.

Here we return to Equation 21 in an effort to quantify some of the error sources for the particular case of resonance over the liner at a centerline Mach number of 0.1. The first term to be estimated is the turbulent momentum flux through the wall. The bias error originating from this term in the shear stress determined through the pressure gradient is normalized by the wall shear stress,

$$\epsilon_{u,v} = \frac{\rho\sigma}{4\overline{\tau_w}}\overline{\langle u'v'\rangle_w} = \frac{\sigma}{4}\overline{\langle u'v'\rangle_w^+} \tag{40}$$

Figure 61 shows the Reynolds shear stress field over the orifice. Averaging the streamwise locations nearest to the wall over the orifice yields an approximate value

for the average momentum flux through the wall, $\overline{\langle u'v' \rangle_w^+} = -2.5$. This results in a subsequent error of $\epsilon_{u,v} \approx -0.08$. The magnitude is measured at $y^+ \approx 10$, which should not differ much from the value at the orifice exit. It should also be noted that the values here are referenced to the calculated HWT case friction velocity, which has been shown to be higher than the measured value for the L2R case.

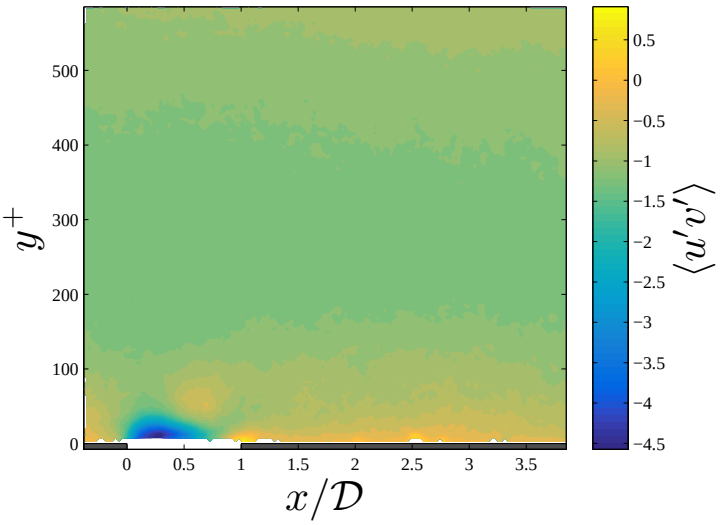

Figure 61. The in plane Reynolds shear stress for the resonance case is pictured, showing the net contribution of energy to the grazing flow from the orifice.

Next, attention is turned to the assumption of a fully developed flow. The bias error from the mean axial momentum flux, normalized by the wall shear stress is

$$\epsilon_{u^2} = -\frac{1}{4h}\frac{\partial}{\partial x}\int_0^h \int_0^h (u^+)^2 dy\, dz. \tag{41}$$

Figure 62 shows the normalized mean axial momentum flux integrated across the half duct. From the plot, it can be seen that the centerline momentum flux has a region of growth for the L2R case until about $65.4 D_h$ where it appears to asymptote. Several simplifications will be made in order to estimate ϵ_{u^2}. Since the liner is only on a single wall, it could be argued that the unlined half of the duct will be identical in axial momentum flux to the hard wall. Further, the value of the integrated flux is assumed constant in the spanwise direction. Finally, the axial derivative will be approximated by the difference of the outflow to inflow momentum flux divided by the length of the liner, L. The incoming momentum flux is assumed to be the same as the hard wall value, and the outflow is assumed to be the asymptotic value of the L2R–2C case. This results in the error estimation of

$$\epsilon_{u^2} \approx -\frac{1}{4L}\left[\int_0^{h/2} (u^+)^2_{x+L} dy - \int_0^{h/2} (u^+)^2_x dy\right]. \tag{42}$$

Estimation of the error in the wall shear stress measurement due to the development of the velocity profile leads to $\epsilon_{u^2} \approx -0.48$. A similar analysis has been

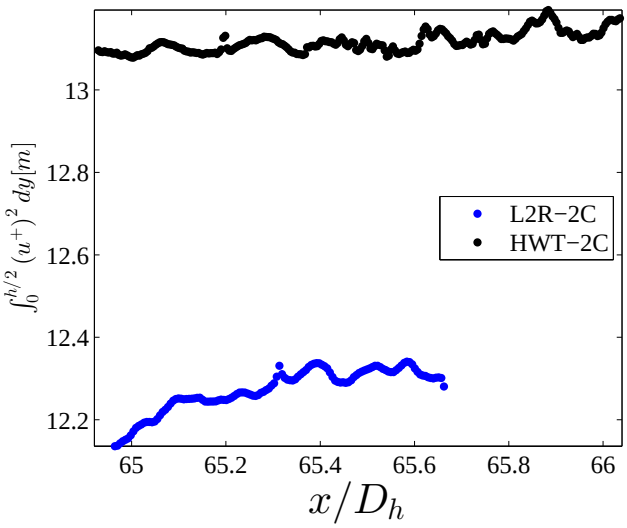

Figure 62. The normalized, integrated axial momentum flux is shown for the liner resonance case as well as the hard wall. The axial extent of the L2R–2C case is less than that of the HWT–2C due to differences in camera setup.

performed on the integrated axial Reynolds stress, which was removed from Equation 21 on boundary layer equation scaling grounds. The difference due to the development of the axial Reynolds stress is much smaller, with a maximum value of about 2.5%. However, the field of view of the L2R–2C case does not extend to a sufficient axial distance to reach a constant value. As it is monotonically increasing to the hard wall value, it is expected that this is a negligible source of error.

Summing the errors due to the development of the velocity profile over the liner and the momentum addition from the turbulent stress through the liner shows that in this case, the wall shear stress determined by the pressure gradient is expected to be about 54% larger than the true wall shear stress. This result indicates the absolute necessity of evaluating the incoming and outgoing momentum flux, even when the flow is fully developed for the hard wall case. It is possible that this error estimate is greatly exaggerated for the micro-perforate type of acoustic liners as the mechanism of acoustic dissipation can largely be attributed to viscous channel losses rather than generation of vortical structures via fluid jetting [9].

6.9 Correlations

The spatial correlations at two wall-normal locations are chosen to be compared to the liner data at resonance, corresponding to $y^+ \approx 30$ and $y^+ \approx 250$. The point at the edge of the buffer region is chosen due to the expected effects of the orifice in the near-wall region. The log-layer point is chosen based on Figure 24 since this region has the largest axial region of high correlation.

Figure 63 shows the correlation between the axial velocity fluctuation at a point near the wall and a point in the log region with all of the other points in the field

at zero time delay. The correlated region is elongated in the axial direction and inclined at an angle of 10°–12°.

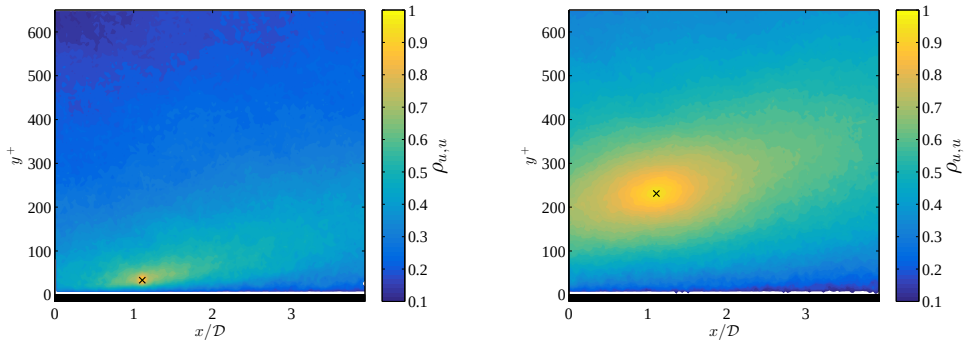

Figure 63. A comparison of $\rho_{u,u}$ at the near-wall (left) and log region (right) points are shown for the hard wall case.

Figure 64 shows the correlation between the axial velocity fluctuations at the selected points to the wall-normal velocity fluctuations at every point in the field. Although the region of strong correlation is greatly increased in the log region compared to near the wall, the maximum correlation magnitude of approximately 0.4 appears to be relatively independent of the wall-normal location.

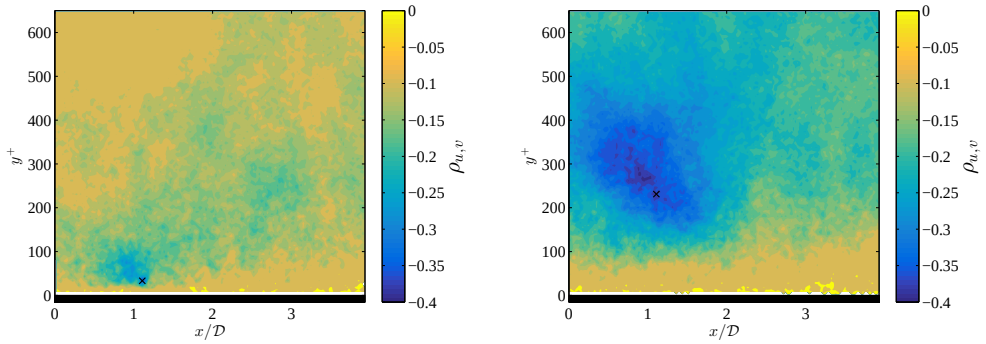

Figure 64. A comparison of $\rho_{u,v}$ at the near-wall (left) and log region (right) points are shown for the hard wall case.

The trends for $\rho_{v,u}$ and $\rho_{v,v}$ are included in Section C.1. The correlations are compared to several points for the liner resonance case at a phase angle of 0°. Four locations were chosen, one in front of the orifice, one in a region of inflow (upstream in orifice point), one in a region of outflow (downstream in orifice point), and downstream of the orifice. In a manner similar to the hard wall case, corresponding points in the log law are chosen to match the near wall points. The streamwise-streamwise correlation is shown in Figure 65 for the near wall points. The maximum correlation with axial station is inclined at a slightly higher angle for these cases, with the

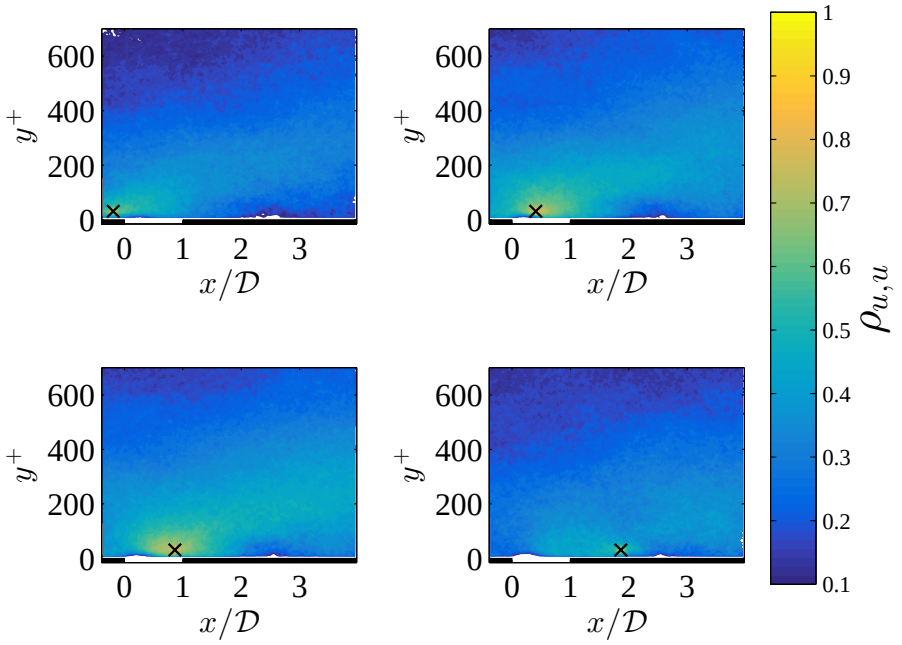

Figure 65. The correlation coefficient $\rho_{u,u}$ is shown for the four near-wall locations over the liner with acoustic forcing at the resonant frequency are shown for the phase of 0°.

two upstream points resulting in angles of 15° while the two downstream points are closer to 20°. This is indicative in changes to the near wall turbulent structure. The region of strong correlation is much smaller for the point downstream of the orifice, indicating a decreased presence of well correlated turbulent structure. Figure 66 shows the streamwise-streamwise correlation at the higher wall-normal locations. The overall pattern of correlation appears to be similar to the hard wall case, and the angle of inclination of the line of maximum correlation matches the hard wall values. However, there is still a significant reduction in the area over which strong correlation exists. Using a threshold of 0.6, the area of the well correlated region is only 50% of the area above the threshold for the hard wall case. This high of a threshold level was chosen to mitigate the effects of cutting off regions of strong correlation for points near the boundary.

The correlation plot for the wall-normal velocity fluctuation at the selected points with the streamwise fluctuation for the field, shown in Figure 67, illustrates the pronounced effect of the jetting on the boundary layer, with the magnitude of the correlation greater than 0.15 for 60% of the field and greater than 0.1 for 95% of the field. Conversely, there is almost no correlation across the field for the downstream location, with only 1% of the field having $|\rho_{v,u}| > 0.1$. Figure 68 provides a good illustration of the penetration height of the jet, although this could be conservative as the maximum outflow does not occur at this phase.

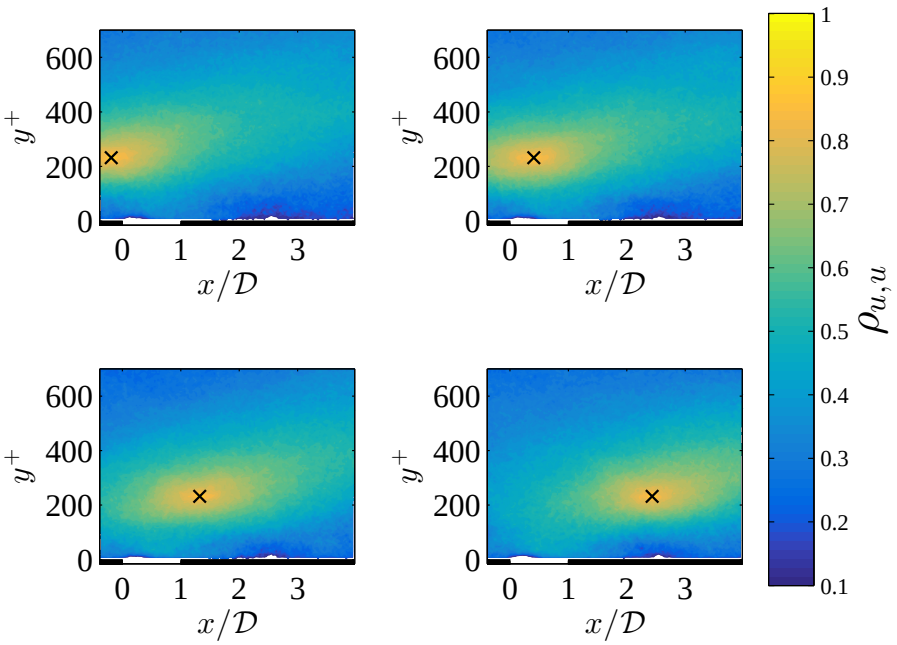

Figure 66. The correlation coefficient $\rho_{u,u}$ is shown for the four locations in the log region over the liner with acoustic forcing at the resonant frequency are shown for the phase of 0°.

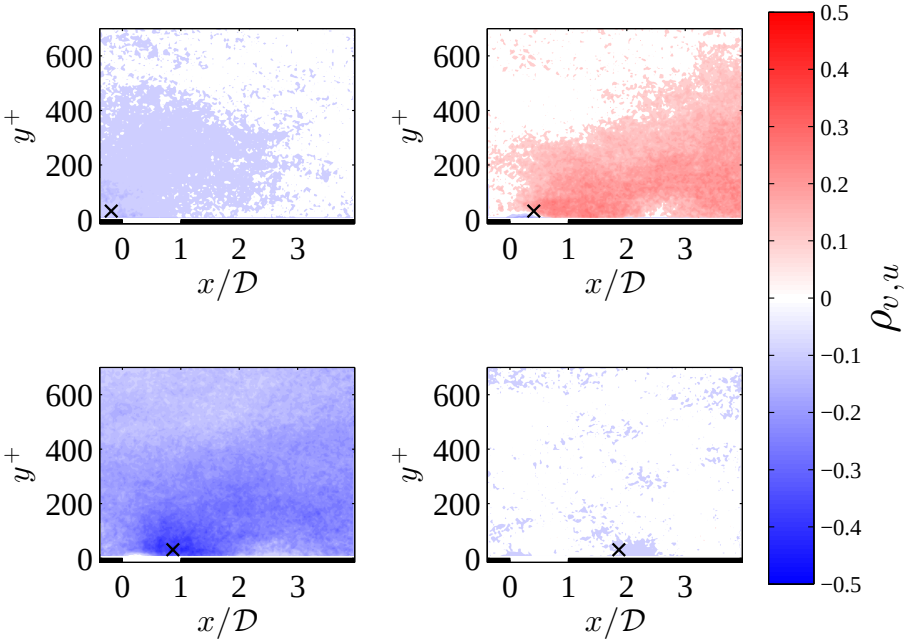

Figure 67. The correlation coefficient $\rho_{v,u}$ is shown for the four near-wall locations over the liner with acoustic forcing at the resonant frequency are shown for the phase of 0°.

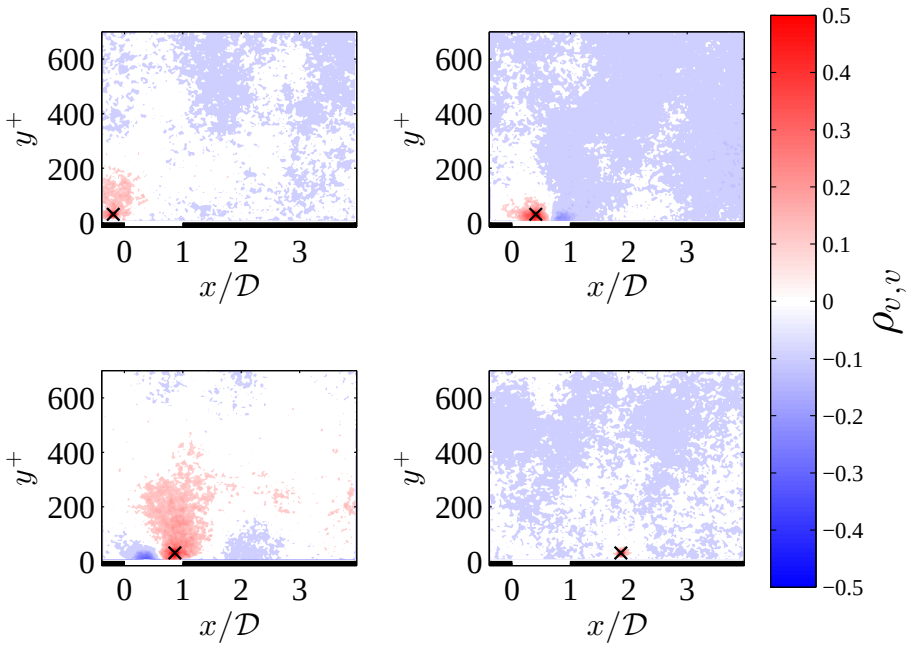

Figure 68. The correlation coefficient $\rho_{v,v}$ is shown for the four near-wall locations over the liner with acoustic forcing at the resonant frequency are shown for the phase of 0°.

6.10 Vorticity Maps

The spanwise vorticity, defined as

$$\omega_z = \frac{\partial v}{\partial x} - \frac{\partial u}{\partial y}, \tag{43}$$

is dominated by the gradient of the streamwise velocity in the wall-normal direction for the hard wall case. Figure 69 shows the mean vorticity for the hard wall case, normalized by wall units. For the lined case, the streamwise gradient of the wall-normal velocity should produce positive vorticity at the upstream lip when there is injection and negative vorticity at the downstream lip. Figure 70 shows the vorticity field for both the baseline and broadband cases. The overall levels of vorticity are lower for the lined cases, due to the softer velocity gradient off the wall, which is the main contributor to the vorticity. In the mean sense, there is not strong injection or suction for either of these cases, and consequently there is not significant impact on the vorticity over the orifice. Figure 71 shows the mean vorticity as a function of phase for the resonance case. As the orifice moves toward 90°, a region of strong negative vorticity is pushed upward. The vorticity is then shed and convected downstream. However, this trend is obscured by the contribution from the wall normal velocity gradient. If the vorticity due to the periodic fluctuating component is plotted, as in Figure 72, a train of shed vortices with alternating sign is visible. Again, it is stressed that the apparent stretching of the vortex in the wall normal direction is an artifact of the plot scale. The upward limit of the diffusion of this vorticity corresponds well with the peak in the Reynolds stresses.

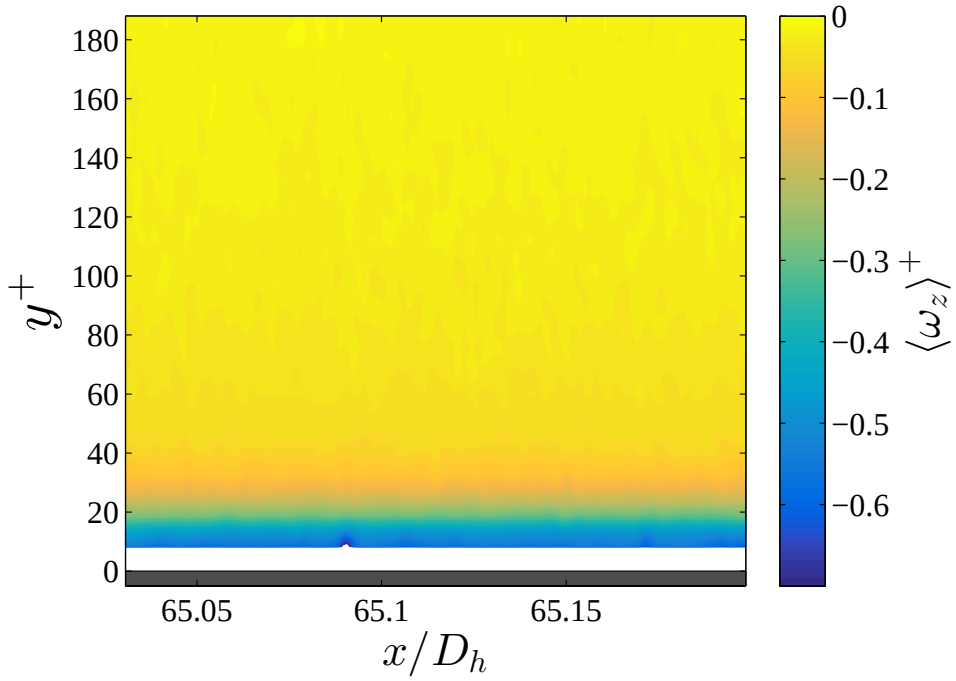

Figure 69. The spanwise vorticity field is shown for the hard wall case.

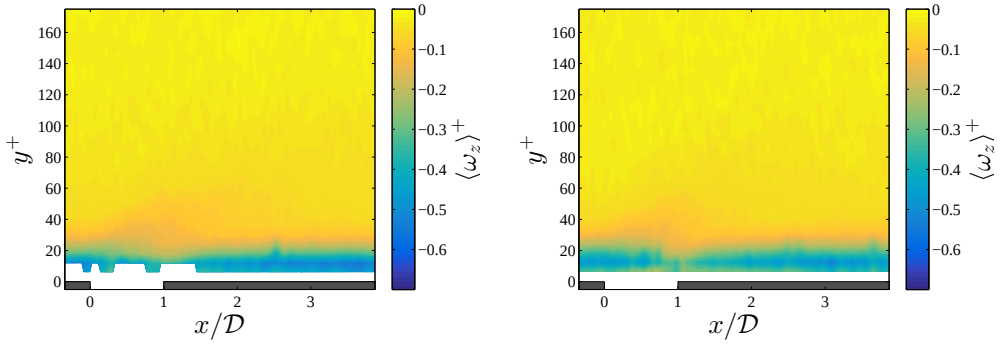

Figure 70. The mean spanwise vorticity field for the baseline (left) and broadband (right) liner cases.

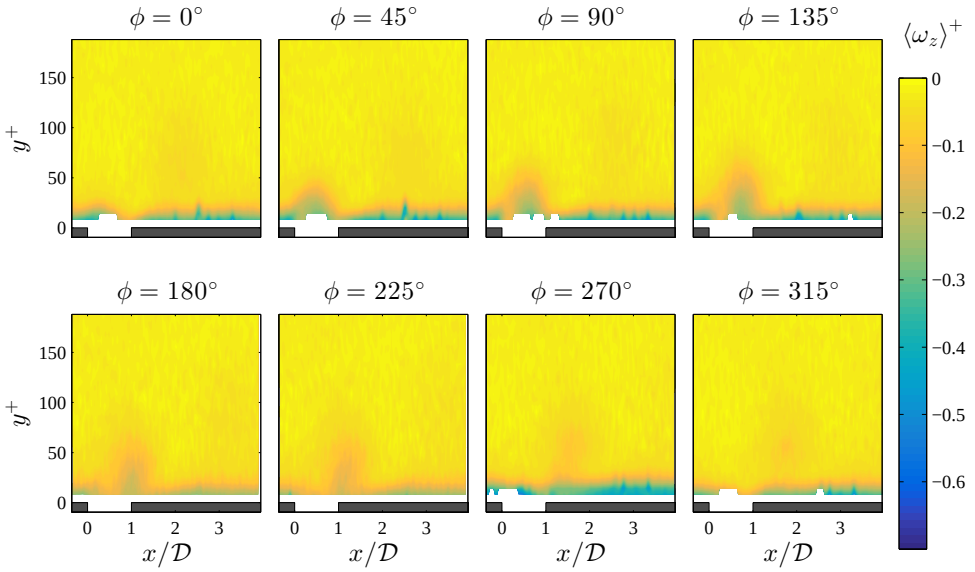

Figure 71. The spanwise vorticity field is shown for the phase averaged mean component of velocity at each phase.

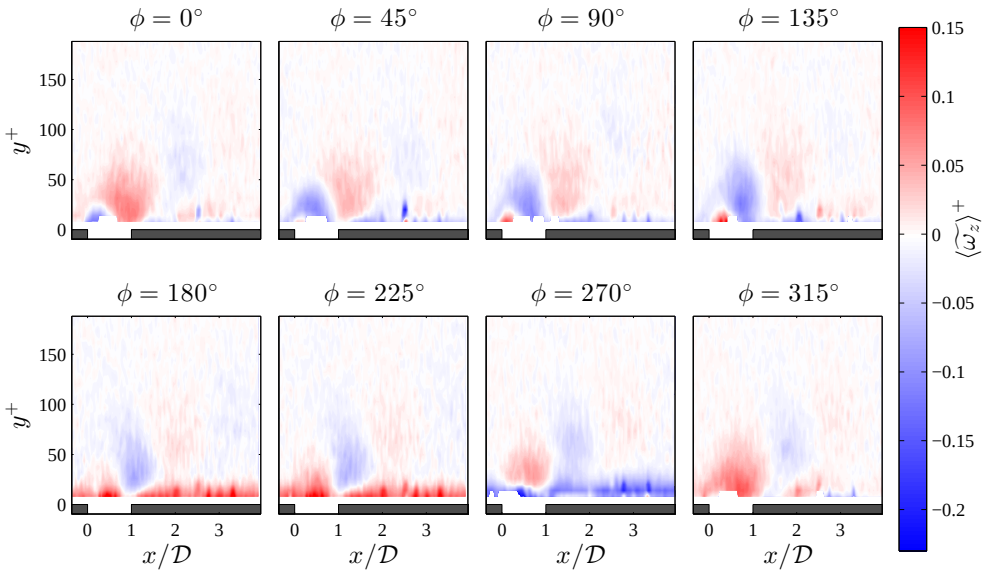

Figure 72. The spanwise vorticity field due to the phase averaged fluctuating component of velocity is shown for each phase.

6.11 Conclusions

The results of the velocity field analysis yield some insight into the near wall flow behavior. For all of the liner cases, a layer at $y^+ \approx 100$ of high wall normal Reynolds stress is present, with a peak in the streamwise normal and in-plane shear Reynolds stresses located farther from the wall at $300 < y^+ < 500$. As the location of the layer does not move farther away from the wall for the resonance case, where the jetting is much stronger than the other cases, it is not clear whether this is due to the transport of turbulent momentum upward by the fluctuating component of the velocity over the orifice. The fluctuating wall-normal velocity was shown to only have significant contributions to the total fluctuating rms levels in the localized region directly above the orifice. The large increase in the rms fluctuations seen in the resonance case over the hard walled section is almost entirely due to the Reynolds stress.

Analysis of the two point velocity correlation function indicated a lifting of the near wall turbulent structure as it passes over the orifice. This is consistent with Park and Choi [22] who indicate that the reduction in skin friction downstream of an orifice is due to lifting of streamwise aligned vortices. Following the lifting of these structures, the correlations in the region behind the orifice exhibits a significant reduction in the size of a well correlated region. This region also has a train of spanwise vortices of alternating sign. Kim [21] noted that the presence the spanwise vorticity was related to the area of lowered shear stress.

Apart from the near wall flow behavior, errors due to common assumptions used in the control volume method are assessed for the resonance case. It is shown that there are large biases which the flow can present to the analysis so that the skin friction can be obscured by changes in the flow profile or the influx of momentum from the orifices.

The intrusiveness of the CWSSS measurement over the liner was also determined under tonal and broadband acoustic forcing. While the results are likely to depend on the liner, or more specifically the orifice geometry and spacing, there is only a difference between the patch and liner PIV curve fit cases on the order of 5% for the current liner. This provides some evidence that the CWSSS package is compact enough to be representative of the region behind an acoustic liner, rather than a smooth patch interrupting the the flow over an acoustic liner.

7 Shear Stress Measurement Comparisons

The wall shear stress has been measured under a range of acoustic and flow conditions via multiple methods: curve-fit velocity profiles, mean axial pressure gradient, and the CWSSS. In Table 8, a list of identifiers for particular cases is presented in order to facilitate reading of the plots in the following section. The prefixes for the case identifiers are the same abbreviations used for the PIV cases in Table 7. For the hard wall cases, the suffix of F or A indicates that the fiberglass or anechoic diffuser was used, respectively. For all lined cases, the anechoic diffuser was utilized. As mentioned previously in Section 6.1, for all of the cases of acoustic excitation,

Table 8. Listing of Cases and Associated Parameters.

Case	Acoustic Excitation	M_b Range	M_b Increment
HWF	None	$[0.07, 0.30]$	0.01
HWA	None	$[0.07, 0.30]$	0.01
L1B	None	$[0.08, 0.30]$	0.02
L1BB	Broadband	$[0.08, 0.30]$	0.02
L1R	Resonance	$[0.10, 0.30]$	0.02
L2B	None	$[0.091, 0.26]$	–
L2A	Maximum Attenuation	$[0.091, 0.26]$	–
L2BB	Broadband	$[0.091, 0.26]$	–
L2R	Resonance	$[0.091, 0.26]$	–

the rms pressure fluctuations are set to 140 dB and spread over the applicable frequency range. For the broadband case, this is 140 dB OASPL spread over 0.5–3kHz, while the resonance and maximum attenuation cases are 140 dB SPL tones at a single frequency. The Mach number range is set at the lower end by the estimated Mach number where fully developed flow is present, determined from Figure 23. The variations in the number of samples taken for the pressure gradient method, 500–5000, were due to increased fluctuations noted in the broadband cases at low Mach number. This increased fluctuation level is limited to excitation in the low frequency range as the increased levels of pressure fluctuations were not present for the resonance or attenuation cases. The number of samples taken by the CWSSS, between 5400–9000, was chosen as a balance between a long enough time to average out fluctuations while still being short enough to avoid significant amounts of sensor drift.

7.1 Curve-Fit Velocity Profiles

The velocity profile from the PIV results are used to determine the friction velocity based on a least squares fit of the data to Equation 12. In order to limit errors due to the deviation of the velocity profile in the liner cases from the log law, only points within $100\,y^+$ were used. Table 9 shows the values of the friction velocity and corresponding value of wall shear stress for each of the cases. The reader is again

referred to Table 7 for a key describing the case descriptors. There were significant reductions in the calculated friction velocities for the lined cases compared to the hard wall cases. The resonance case shows the highest reduction in skin friction of all the cases, with a reduction of roughly 30% compared to the hard wall cases. However, the reduction in skin friction indicated by the PIV results is not necessarily indicative of a global reduction of wall shear stress, even if this is true along the centerline. Jabbal and Zhong [51], noted a reduction in wall shear stress along the center of the orifice of a single synthetic jet in a zero pressure gradient laminar boundary layer, which was flanked on either side by regions of high wall shear stress, as shown in Figure 73. Further, the Spalding composite profile used for curve fitting

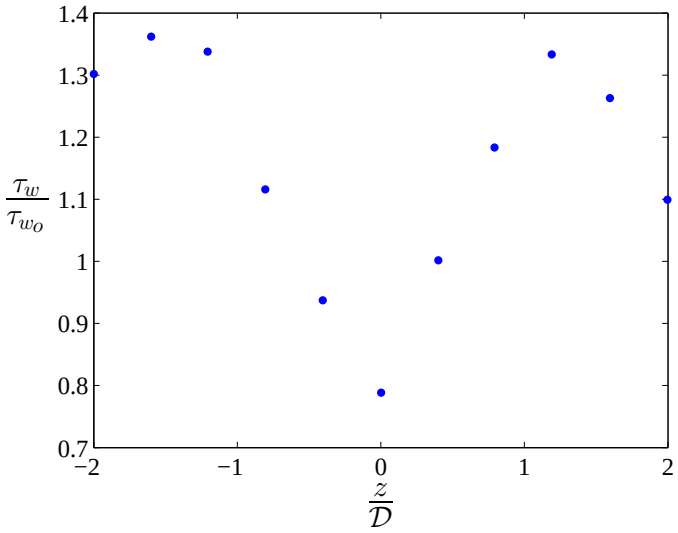

Figure 73. The spanwise wall shear stress distribution located twenty four orifice diameters downstream of synthetic jet actuator. The wall shear stress is normalized by the values corresponding to an undisturbed boundary layer. Adapted from Jabbal and Zhong [51].

assumes a two dimensional boundary layer, which is not the case for an acoustic liner. In sum, it is important to stress that the values obtained from curve fitting PIV data only show a local reduction of wall shear stress along the plane aligned with the center of the orifice. The quantitative results of these measurements do not account for the bias of assuming a two dimensional boundary layer, although the qualitative trends of decreased boundary layer 'fullness' are consistent with a reduction of the shear stress at the wall.

7.2 Baseline Flow Comparison

This section focuses on measurements of the hard-walled case in an effort to validate the measurement techniques in a more fundamental flow. However, as has been noted previously, the effects of secondary flow on the perimeter averaged wall shear stress are not directly addressed in the channel flow or pipe flow models. The first

Table 9. Least Squares Curve-Fit Wall Shear Stress.

Case	u_τ $[\frac{m}{s}]$	τ_w $[Pa]$
HWU	1.36	2.23
HWD	1.38	2.34
HWT	1.41	2.41
L2B	1.31	2.06
L2BB	1.20	1.74
L2R	1.14	1.57
L2A	1.24	1.85
P2B	1.32	2.09
P2BB	1.24	1.85
P2R	1.13	1.53

comparison presented is between the anechoic and fiberglass diffusers. This is an effort to quantify whether or not there are significant differences due to configuration effects.

The fiberglass diffuser was used during PIV testing to avoid the accumulation of seed particles in the anechoic diffuser. The anechoic diffuser was used for all other testing, The perimeter averaged wall shear stress determined through the control volume approach is shown in Figure 74 with comparison to the curve fits from Section 1.2. On average, the difference in the average measured shear between the two tunnel configurations is one percent, which is likely due to small differences in Mach number between different tests and the measurement uncertainty. The 95% confidence intervals for the Reynolds number are obtained via sensitivity analysis and 95% coverage intervals for the shear stress are obtained using a Monte Carlo simulation. For the remainder of this document, the term coverage interval will imply that the results were generated using a Monte Carlo simulation, while the term confidence interval will refer to those results which come from a sensitivity analysis. The details of the Monte Carlo simulations can be found in Appendix A, and the sensitivity analysis is outlined in Appendix B.

There appears to be relatively good agreement when comparing the wall shear stress to the expected values, although this is partially due to the scale of the plot. The estimated shear stress is typically about 15-20% higher than the measured shear stress at low Reynolds numbers. When the friction factor is plotted instead, as in Figure 75 the differences between the measured data and the models appear more clearly. The uncertainty in the friction factor is also determined through Monte Carlo simulation. For all the uncertainty ranges calculated, the bias error originating from the pressure sensors used to calculate the bulk Mach number is the dominant source. The only exception to this is the shear stress, which is a function only of the differential pressure measured by the pressure scanner.

Although variations are within the measured uncertainty range, the friction factor appears to be increasing with Reynolds number, which is nonphysical behavior. The friction factor should continue to decrease with increasing Reynolds number until roughness effects arise, at which point the friction factor will asymptote. If

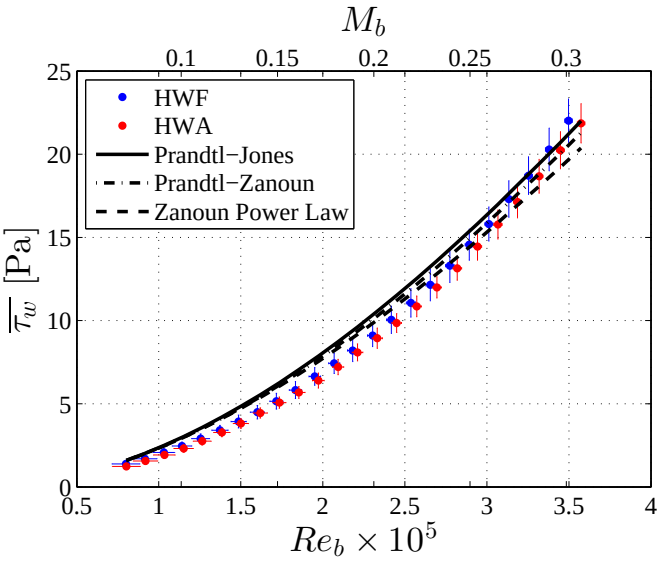

Figure 74. The perimeter averaged wall shear stress is determined using the mean axial pressure gradient over a range of bulk Reynolds numbers and Mach numbers for both diffusers. The wall shear stress is compared to some curve fits from literature.

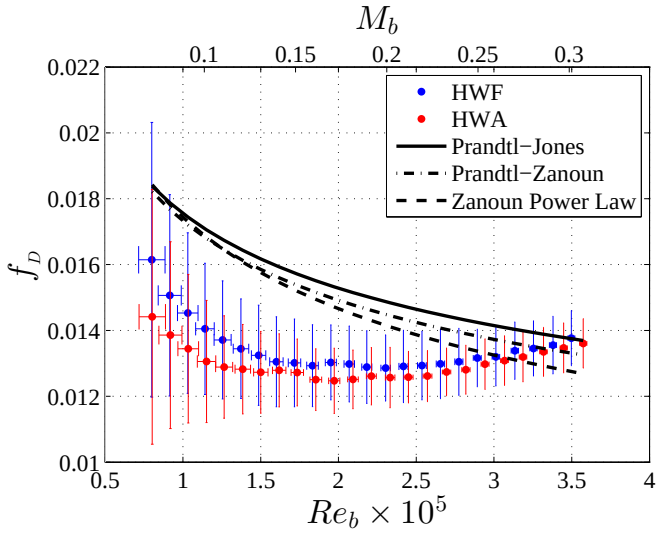

Figure 75. The friction factor based on the mean axial pressure gradient over a range of bulk Reynolds numbers and Mach numbers for both diffusers. The friction factor is compared to some curve fits from literature.

instead the corrected Mach number determined by Equation 25 is used, as in Figure 76, the tail up at higher Mach numbers is curbed and the mean values appear to reach a constant value of approximately 0.012.

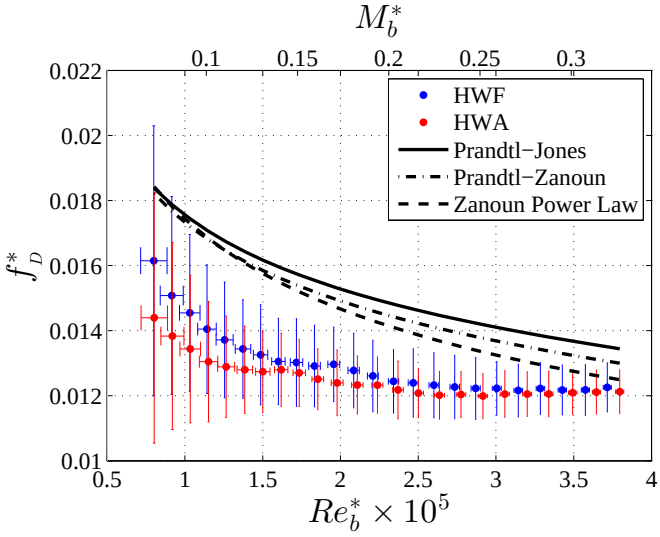

Figure 76. The friction factor based on the mean axial pressure gradient over a range of bulk Reynolds numbers and Mach numbers for both diffusers. The bulk Mach number is altered to match the expected ratio of centerline to bulk velocity in fully developed channel flow.

Secondarily, the hard wall tests provided a means of checking the dc calibration of the CWSSS. In order to do this, pressure gradient data was taken simultaneously with the CWSSS over a range of flow speeds. Using the dc voltage change from the no flow to flow conditions and the measured pressure gradient, an estimate of the sensitivity of the CWSSS can be made under the assumption that the perimeter averaged shear stress is equal to the centerline shear stress. This is not completely without merit, as work by Joung [52] shows that for bulk Reynolds numbers between 4400–65,000, the shear stress distribution in a square duct tends toward a uniform profile with increasing Reynolds number. The profile is centered around the perimeter averaged shear value, except in the corners, where the shear stress falls precipitously. Work done by Gessner [53] at Reynolds numbers commiserate with those considered here shows the distribution of shear stress in the duct, determined using Preston tubes in Figure 77. The integrated shear stress profile using the Preston tubes indicates that the perimeter averaged value is only 5% less than the centerline value. However, the perimeter averaged shear stress measured through the pressure gradient was 20% less than the centerline Preston tube value. Gessner suggests this might be due to the limited sample size of the pressure measurement as well as the short region over which the pressure gradient measurements were taken.

Figure 78 shows the collected CWSSS dc voltage for $M_b = 0.091$. The differential pressure is typically measured as the average of the no flow conditions prior to

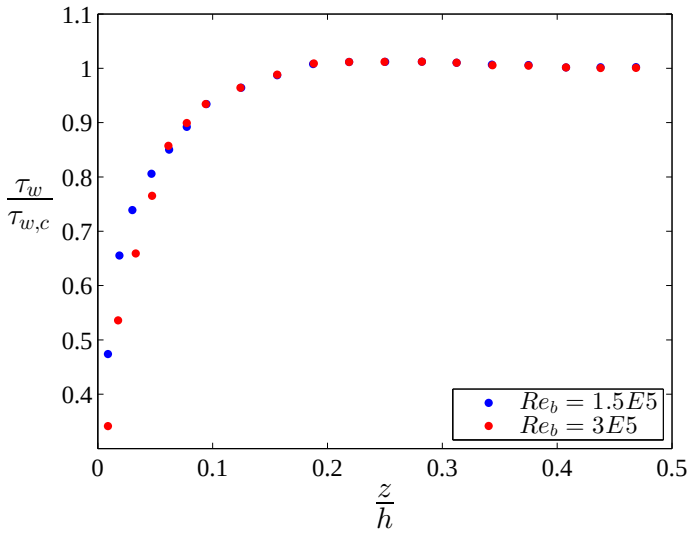

Figure 77. The figure, adapted from Gessner [53] shows the distribution of the wall shear stress normalized by the centerline shear stress over half of the duct.

and after the test run subtracted from the average value for the test condition. However, from the figure, it is occasionally more appropriate to choose only one no flow condition to base the differential measurement. An example of this is for Test 4, where the no flow average prior to the test is used. The large jump toward the end of Test 4 is likely an issue with the sensor grounding. In all of the tests, some drift can be seen, and a majority of data fails tests for stationarity, even in the presence of stationary flow conditions. The remainder of the dc voltages for all of the flow conditions can be found in Appendix C.2.

Returning to the dc calibration, the data is presented in Figure 79 along with the least squares linear fit. The test is carried out by increasing the bulk Mach number from 0.091 to 0.3, and comparing the perimeter averaged wall shear stress obtained with the control volume method with the mean voltage shift of the CWSSS. The sensitivity is determined to be 1.0875 $\frac{mV}{Pa}$, with $R^2 = 0.99$. The intercept of the line does not pass through zero, leaving a shear stress of 0.58 Pa for zero voltage shift, indicating that there will be large error for low shear stresses. It was decided not to artificially force the data through the origin in order to get an estimate of the bias error present in the calibration procedure.

7.3 Liner Flow Comparisons

A similar analysis to the hard wall case is carried out with liner L1 and L2. As liner L1 does not have a CWSSS insert, only the control volume technique was used to determine the perimeter averaged shear stress over the liner at several Mach numbers. The broadband acoustic excitation for the data shown here is 140 dB OASPL over the frequency range 0.5 – 3 kHz. The acoustic excitation for the resonance case is 140 dB SPL at the expected resonant frequency of the liner. This

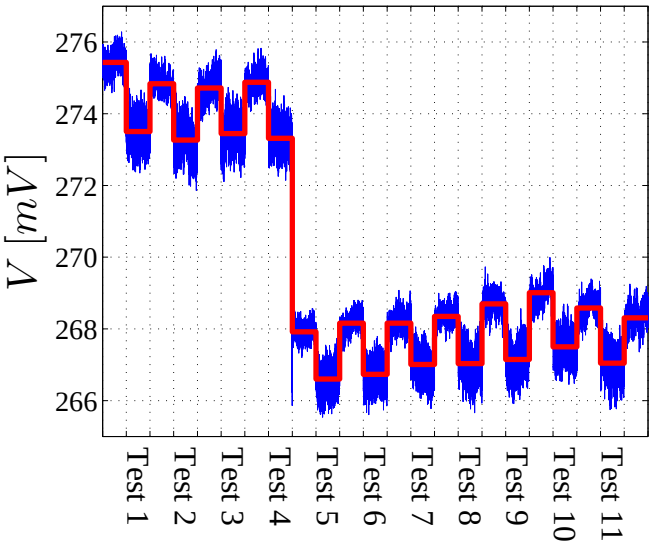

Figure 78. The dc voltage measured with the CWSSS is plotted for the number of tests taken. The high voltage corresponds to the no flow condition while the lower voltage corresponds to the test condition. The mean voltage is presented as the red line, while the raw data is blue.

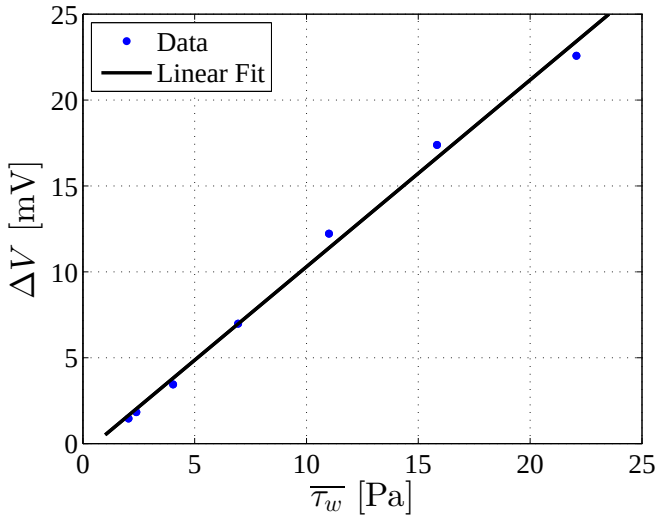

Figure 79. The dc voltage differential measured with the CWSSS is plotted against the perimeter averaged wall shear stress.

is assumed to vary linearly over the range of bulk Mach numbers of 0.1 to 0.3, from 1.675 kHz to 1.8 kHz, which are the values using the values given in Table 5. This assumption is supported by the estimated resonant frequencies calculated using the two parameter model over the Mach number range for the L1 liner geometry. Liner L2 is tested only at the two Mach numbers where acoustic impedance spectra are available, which were presented in Section 5.2.2. Due to mechanical issues with the CWSSS, only the hard wall and baseline liner cases are available.

Figure 80 shows the wall averaged shear stress as a function of Reynolds number under a variety of acoustic conditions as well as the corresponding hard wall data. Comparison to the duct shear models is also shown as a guide, and the 95% coverage intervals are shown for the shear stress, along with the 95% confidence intervals for the Reynolds number. The difference between the liner and the hard wall is masked somewhat by the spatial averaging over three hard walls and a single lined wall. To

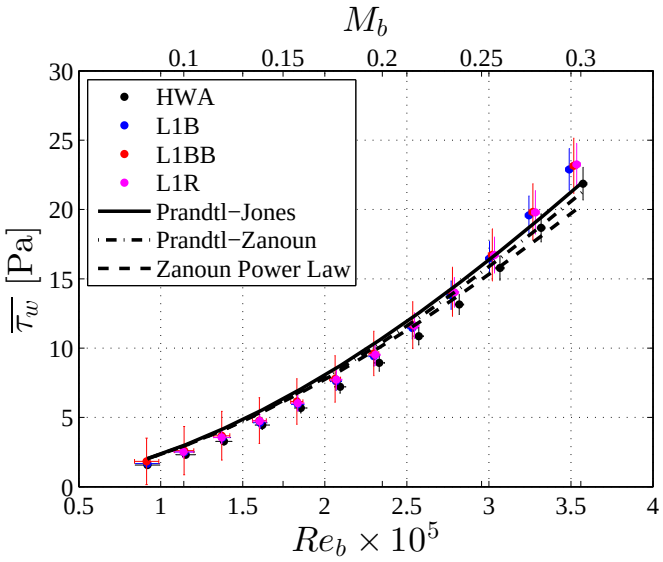

Figure 80. The wall shear stress is presented for all the different cases taken over liner L1 as a function of the bulk Reynolds number. The values for the L1 cases are averaged over the entire duct perimeter, with contributions from three hard walls and a single lined wall.

that end, it is desired to attempt to separate the shear stress of the liner from the hard wall. The contribution from the liner is calculated using the ratio of the lined area to total area and the difference between the shear stress measured with the liner and hard wall cases. The liner shear stress, shown in Figure 81, is calculated as four times the value determined via the pressure gradient with the liner in place minus three times the hard wall value of shear at the corresponding Mach number condition. Separating the liner contribution from the hard wall contribution to the wall shear stress has the unfortunate effect of greatly increasing the span of the 95% coverage interval, so that it is difficult to discern any trends. This can be overcome by installation of the liner on multiple walls, although this change in

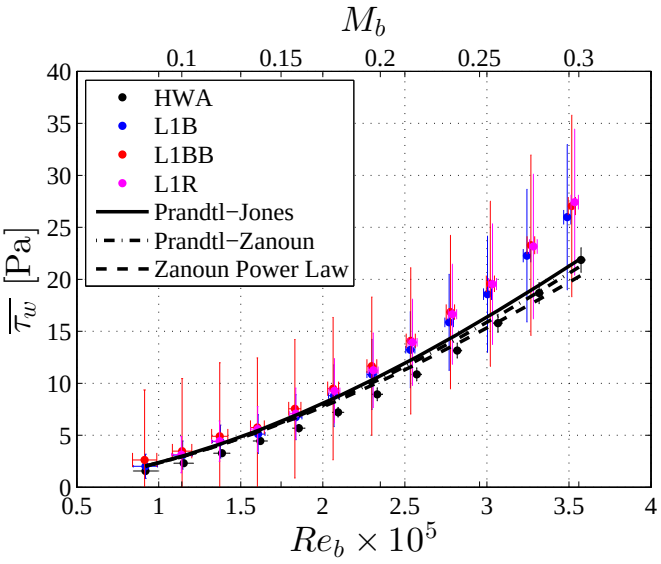

Figure 81. The wall shear stress is presented for all the different cases taken over liner L1 as a function of the bulk Reynolds number. The values for the L1 cases are compensated to be the best estimate of a the lined wall.

boundary condition will also change the nature of the acoustic field over the liner. The normalized plots of the wall shear stress as a function of Reynolds number are provided in Figure 82, showing the friction factor for the average of the entire duct, and Figure 83, showing the friction factor corrected on the basis of area ratio, in an effort to isolate the average shear stress of the L1 liner.

In all the cases above, the large coverage intervals inhibit comparison between the cases. The bulk of the coverage interval for the coefficient of friction is due to large bias error in the dynamic pressure normalization, which can be traced back to the pressure transducers. Bias errors will ideally be similar across all of the test conditions, so that if the bias could be corrected, the data would simply shift up or down. It should be cautioned that as the values of the shear stress and to some degree, the dynamic pressure, varies between tests, this will change the sensitivities to the bias error. This, in turn, means that the systematic error will not cancel completely between two similar tests [54]. While the data cannot be used to draw quantitative results, qualitative relationships between the data should be intact despite the presence of bias. Figure 84 shows the duct averaged friction factor with the corrected Mach number as a function of the Reynolds number. All of the liner cases have an increased friction factor, and the resonance case appears to lead to the highest increase in friction factor out of the tested excitation types. As the Mach number increases, the effect of the acoustic excitation appears to converge on the liner baseline case. This is expected, as the relative strength of the acoustic velocity at the orifice decreases compared to the grazing flow.

The results of the shear stress test for the liner L2 are summarized in Table 10. It is important to note that the coverage interval listed in the table only accounts

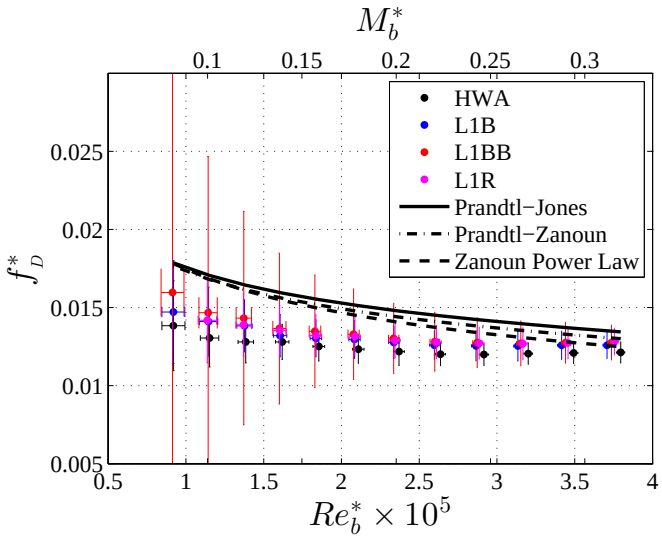

Figure 82. The friction factor is presented for all the different cases taken over liner L1 as a function of the corrected bulk Reynolds number. The values for the L1 cases are averaged over three hard walls and a single lined wall.

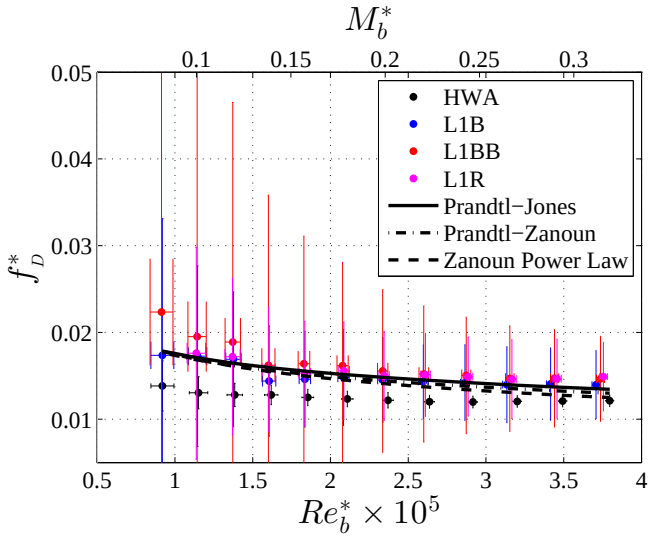

Figure 83. The friction factor is presented for all the different cases taken over liner L1 as a function of the corrected bulk Reynolds number. The values for the L1 cases are compensated to be the best estimate of the lined wall.

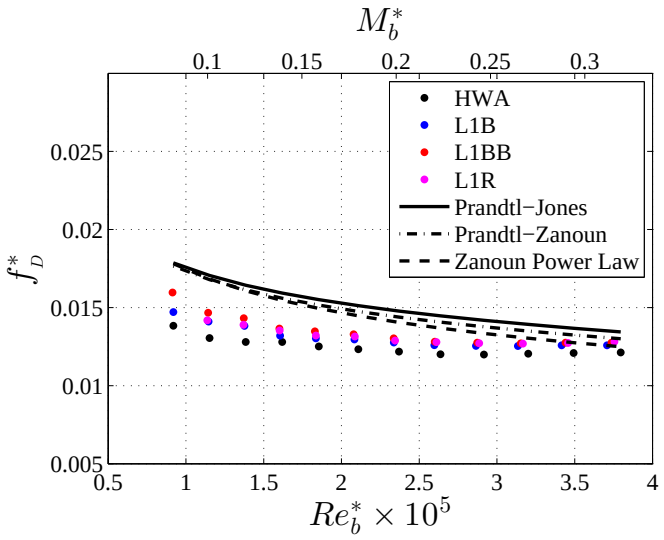

Figure 84. The friction factor is presented for all the different cases taken over liner L1 as a function of the corrected bulk Reynolds number. The values for the L1 cases are averaged over three hard walls and a single lined wall.

for the random and bias errors of the static pressure measurements. It does not include the bias errors that are implicit in the fully developed assumption of the control volume method, which was shown to be significant in Section 6.8. For the pressure gradient measured shear stress, the increase in shear stress for the L2 cases compared to the hard wall is about twice as large as the increase in shear stress for the L1 cases. This is in agreement with trends seen in other authors' tests where liners with larger diameter holes and higher porosities tend to lead to increases in the shear stress. The CWSSS measurements at the lower Mach number condition are consistent with the PIV curve fit results showing a decrease in the wall shear stress for the lined case. Again, this decrease is a local, single point measurement located directly downstream of the center of the orifice, and not indicative of the integrated shear values over the entire acoustic liner. During testing over the acoustic liner, the sensor suffered a mechanical failure which precluded usable data to be collected for the excitation cases.

7.4 CWSSS ac Measurements

One of the expected advantages of using a shear sensing technique with a large bandwidth is that it can highlight differences in the fluctuating content of the wall shear stress, while other techniques are only able to determine the dc content. In this section the power spectrum of the shear stress is presented, first for the hard wall cases at several Mach numbers, and second for the L2 liner under a variety of acoustic conditions. The sensitivity of the CWSSS used to convert the voltage to stress units is different than the value used for the dc measurements. This is due to the frequency dependance of the CWSSS frequency response function. It is

Table 10. L2 Shear Table.

Case	M_b	$\tau_{w,dp/dx}$	$\tau_{w,dp/dx}$ 95% Coverage	$\Delta V\ [mV]$	$\tau_{w,CWSSS}$
HW	0.091	2.05	±0.033	1.46	1.34
L2B	0.091	2.16	±0.080	1.18	1.08
L2BB	0.091	2.33	±0.585	–	–
L2A	0.091	2.14	±0.084	–	–
L2R	0.091	2.25	±0.080	–	–
HW	0.260	15.84	±0.159	17.38	15.98
L2B	0.260	16.54	±0.324	17.77	16.34
L2BB	0.260	16.79	±0.547	–	–
L2A	0.260	16.85	±0.327	–	–
L2R	0.260	16.85	±1.570	–	–

calculated using the PWT method outlined in Section 3.4.2, and is equal to $4.58\frac{mV}{Pa}$ at $1.128\,kHz$.

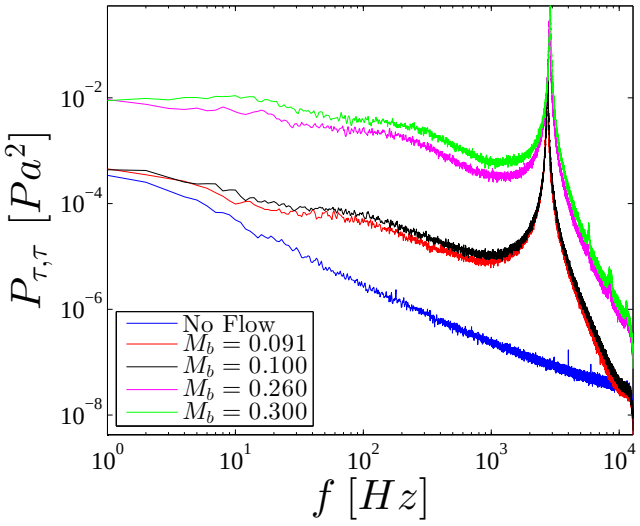

Figure 85. The ac shear stress power spectrum is plotted for a range of Mach numbers, 0.091, 0.1, 0.26, and 0.3.

The hard wall data is presented in Figure 85 for several Mach numbers. The general features of the spectra show a large flat energy containing region at low frequencies, and the start of a roll-off in the range of $200 - 300\,Hz$. However, the effects due to the nonlinear response of the sensor begin to take over at higher frequencies, with a peak in energy at the sensor resonance. The resonant frequency of the sensor, determined here by the frequency with the highest power ranges from 2.74–2.89kHz, increasing slightly as the Mach number increases.

Again, due to a sensor failure, the baseline case is the only L2 case available for comparison to the hard wall case, shown in Figure 86 for $M_b = 0.091$. There

are very few differences in the power spectrum apart from a slight decrease in shear content at low frequencies.

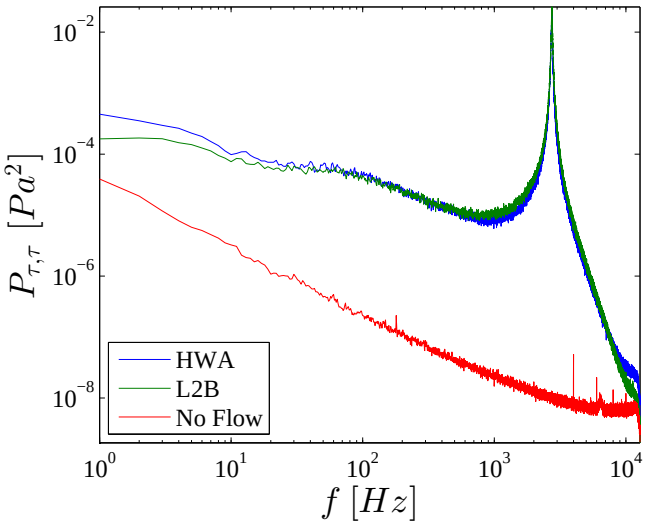

Figure 86. The ac shear stress power spectrum is plotted for several cases over the L2 liner at $M_b = 0.091$, along with a comparison to the hard wall case and no flow.

Finally, the ac content for the L2 liner at $M_b = 0.26$ is shown in Figure 87. The agreement between the spectra is quite good, and the differences, which may exist at low frequencies for the lower Mach number, are no longer evident. The ac content of the shear stress signal appears to be largely unchanged by the roughness posed by the orifices, suggesting that either the effects are local to the surface very near the orifice, or that the fluctuating shear stress content is not very sensitive to the roughness.

7.5 Conclusions

The wall shear stress has been determined for a wide range of flow and acoustic forcing conditions. The hard wall tests showed a linear response between the voltage change for the CWSSS and the pressure gradient over the test section. The average shear stress determined from the pressure gradient for the $M_c = 0.1$ hard wall case is 10–15% lower than the value determined using the centerline PIV curve fitting method, which is similar to the results of Gessner [53], which showed a 20% disparity between the centerline shear stress measured with a Preston tube and the shear stress from the pressure gradient.

With respect to the results over the liner, there is disagreement between the three shear stress measurements. The curve-fit velocity profiles indicate that the skin friction decreases for the liner cases, while the pressure gradient method shows an increase for the liner cases. The CWSSS consistently underpredicts the wall shear stress, but based on the two PIV cases taken at the same conditions, appears to follow the trends of the velocity profile curve fits. The low values at the smaller Mach

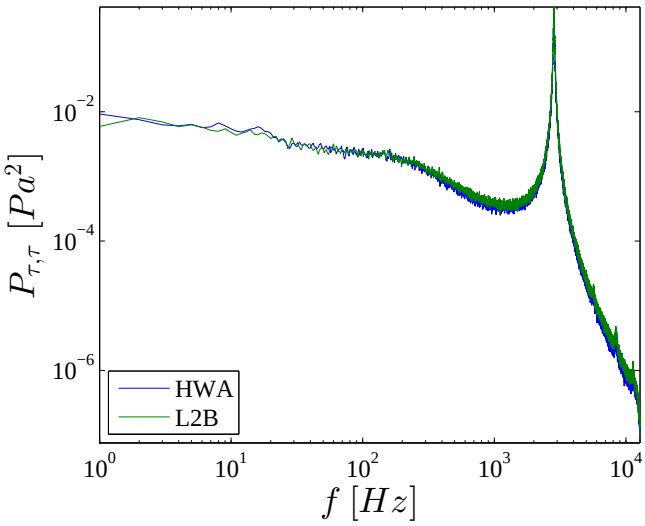

Figure 87. The ac shear stress power spectrum is plotted for several cases over the L2 liner at $M_b = 0.260$, along with a comparison to the hard wall case.

number could be due to uncertainty in the dc sensitivity. The procedure outlined in Section 3.4.2 has shown that the sensor is capable of accurately resolving shear stresses on the order of 1–2 Pa in the flow cell. However, the range of the calibration performed in the GFID was on the order of 2–20 Pa. Consequently, small changes in the slope result in large changes in the shear stress for the lower end of the calibrated range.

Returning to the disparity between the pressure gradient method and the curve fit, recall that in Section 6.8 the pressure gradient method was expected to overpredict the true value by 54% for the resonance case. The measured values show that the pressure gradient method is higher than the curve fit wall shear stress for the resonance case by 43%. This high variability in the results illustrates the gross errors present in either the curve fit or pressure gradient methods due to poor assumptions, or that there are large errors in both.

8 Conclusions

The work herein has shown that the facility is capable of accurately educing the impedance of an acoustic liner, and that the flow is consistent with other square duct facility data at similar Reynolds numbers. The wall shear stress has been measured using two indirect methods and one direct method. The control volume method of determining the wall shear stress is shown to exhibit large sources of error when the assumption of a fully developed flow is made. To reduce the error by taking velocity profile surveys upstream and downstream of the liner, the advantage of this method to quickly provide a measurement is mitigated. For this reason, it is suggested that a drag balance be used for engineering based measurements of acoustic liner wall shear stress. Further, the drag balance should be placed in a nominally fully developed flow so that spatial averaging of the wall shear stress in the streamwise direction does not bias the results, as well as allowing for corroboration of results in other facilities.

For physical based measurements over acoustic liners, there is still a usefulness to single point measurements to build a better understanding of the underlying flow mechanisms. The CWSSS showed some promise as a means of measuring the local mean and fluctuating wall shear stress. The wall shear stress over the liner patch compared to the PIV curvefit values was limited to a 5% difference, indicating that moderately accurate single point measurements can be quickly made using the CWSSS. The CWSSS also had a linear response for the range of hard wall cases tested. With continued improvements in dc stability, the CWSSS could be an additional technique which provides insight into the dynamics of a variety of applications.

Investigation of the flow field over the liner showed a region of increased wall normal Reynolds stress at $y^+ \approx 100$ while the in-plane Reynolds shear stress and axial normal Reynolds stress had peaks at higher values of y^+. The two point velocity correlation function showed an increase in the angle of inclination, consistent with lifting the near-wall turbulent structures away from the wall. Downstream of the orifice, a region of low wall shear stress was characterized as having shorter correlation length structures. For the resonance case, a train of streamwise vortices of alternating sign was produced over the orifice and convected downstream. Finally, the velocity profile emanating from the orifice was not consistent with the model of a slug flow profile.

References

1. White, F. M.: *Viscous Fluid Flow*. McGraw-Hill, Boston, third ed., 2006.

2. Prandtl, L.: The mechanics of viscous fluids. 1935.

3. Chung, D.; Marusic, I.; Monty, J. P.; Vallikivi, M.; and Smits, A. J.: On the universality of inertial energy in the log layer of turbulent boundary layer and pipe flows. *Experiments in Fluids*, vol. 56, no. 7, 2015, p. 141.

4. Jones, O. C.: An Improvement in the Calculation of Turbulent Friction in Rectangular Ducts. *Journal of Fluids Engineering*, vol. 98, no. 2, 1976, pp. 173–181.

5. Brundrett, E.; and Baines, W.: The production and diffusion of vorticity in duct flow. *Journal of Fluid Mechanics*, vol. 19, no. 3, 1964, pp. 375–394.

6. Zanoun, E.; Durst, F.; and Nagib, H. M.: Evaluating the law of the wall in two-dimensional fully developed turbulent channel flows. *Physics of Fluids*, vol. 15, no. 10, 2003.

7. Zanoun, E.; Nagib, H. M.; and Durst, F.: Refined cf relation for turbulent channels and consequences for high-Re experiments. *Fluid Dynmaics Research*, vol. 41, no. 2, 2009.

8. Roberts, D.: Equivalent sand-grain roughness of perforated plate acoustic linings. *AIAA 15th Aerospace Sciences Meeting*, AIAA P77-104, 1977.

9. Drouin, M.; Gallman, J.; and Olsen, R. F.: Sound Level Effect on Perforated Panel Boundary Layer Growth. *AIAA*, 2006-2411, 2006.

10. Boldman, D. R.; and Brinich, P. F.: Skin Friction on a Flat Perforated Acoustic Liner. *AIAA Journal*, vol. 14, no. 11, 1976, pp. 1656–1659.

11. Kong, F.; and Schetz, J.: Turbulent boundary layer over solid and porous surfaces with small roughness. *AIAA, Aerospace Sciences Meeting*, AIAA 81-0418, 1981.

12. Wolter, J. D.: Drag Measurements of Porous Plate Acoustic Liners. *AIAA 43rd Aerospace Sciences Meeting*, AIAA 2005-0803, 2005.

13. Hwang, D. P.: Experimental Study of Characteristics of Micro-Hole Porous Skins for Turbulent Skin Friction Reduction. *23rd Congress of International Council of the Aeronautical Sciences*, 2002, pp. 1–7.

14. Howerton, B. M.; and Jones, M. G.: Acoustic Liner Drag : A Parametric Study of Conventional Configurations. *21st AIAA/CEAS Aeroacoustics Conference*, AIAA 2015-2230, 2015.

15. Tillman, T.; and Hwang, D.: Drag reduction on a large scale nacelle using a micro-blowing technique. *37th AIAA Aerospace Sciences Meeting*, AIAA 99-0130, 1999.

16. Winter, K.: An outline of the techniques available for the measurement of skin friction in turbulent boundary layers. *Progress in Aerospace Sciences*, vol. 18, 1979, pp. 1–57.

17. Blackwelder, R. F.; and Haritonidis, J. H.: Scaling of the bursting frequency in turbulent boundary layers. *Journal of Fluid Mechanics*, vol. 132, 1983, pp. 87–103.

18. Gerhold, C. H.; Brown, M. C.; and Jasinski, C. M.: Evaluation of Skin Friction Drag for Liner Applications in Aircraft. *54th AIAA Aerospace Sciences Meeting*, AIAA 2016-1267, 2016, pp. 1–17.

19. Howerton, B. M.; and Jones, M. G.: Acoustic Liner Drag: Measurements on Novel Facesheet Perforate Geometries. *22nd AIAA/CEAS Aeroacoustics Conference*, AIAA 2016-2979, 2016.

20. Spalding, D. B.: A single formula for the "law of the wall". *Journal of Applied Mechanics*, vol. 28, no. 3, 1961, pp. 455–458.

21. Kim, K.; and Sung, H. J.: Effects of Periodic Blowing from Spanwise Slot. *AIAA Journal*, vol. 41, no. 10, 2003, pp. 1916–1924.

22. Park, J.; and Choi, H.: Effects of uniform blowing or suction from a spanwise slot on a turbulent boundary layer flow. *Physics of Fluids*, vol. 11, no. 10, 1999, pp. 3095–3105.

23. Chandrasekharan, V.; Sells, J.; Meloy, J.; Arnold, D. P.; and Sheplak, M.: A Microscale Differential Capacitive Direct Wall-Shear-Stress Sensor. *Journal of Microelectromechanical Systems*, vol. 20, no. 3, 2011, pp. 622–635.

24. Bertolucci, B.: An experimental investigation of the grazing flow impedance duct at the University of Florida for acoustic liner applications. Doctoral dissertation, University of Florida, 2012.

25. Williams, M. D.; Griffin, B. a.; Reagan, T. N.; Underbrink, J. R.; and Sheplak, M.: An AlN MEMS Piezoelectric Microphone for Aeroacoustic Applications. *Journal of Microelectromechanical Systems*, vol. 21, no. 2, 2012, pp. 270–283.

26. Brüel & Kjær: Product Data, Sound Calibrator Type 4231. 2016.

27. Westerweel, J.; and Scarano, F.: Universal outlier detection for PIV data. *Experiments in Fluids*, vol. 39, no. 6, aug 2005, pp. 1096–1100.

28. Griffin, J.; Schultz, T.; Holman, R.; Ukeiley, L. S.; and Cattafesta, L. N.: Application of multivariate outlier detection to fluid velocity measurements. *Experiments in Fluids*, vol. 49, no. 1, apr 2010, pp. 305–317.

29. Barnard, C. A.; Mills, D.; Meloy, J.; and Sheplak, M.: Development of a hydraulically smooth wall shear stress sensor utilizing through silicon vias. *Solid-State Sensors, Actuators, and Microsystems Workshop, Hilton Head SC*, 2016, pp. 234–237.

30. Meloy, J.; Sells, J.; Chandrasekharan, V.; Griffin, J.; Cattafesta, L.; Arnold, D.; and Sheplak, M.: Experimental verification of a capacitive shear stress sensor for low-speed wind tunnel applications. *Solid-State Sensors, Actuators, and Microsystems Workshop, Hilton Head SC*, 2012, pp. 303–306.

31. Sheplak, M.; Padmanabhan, A.; Schmidt, M. A.; and Breuer, K. S.: Dynamic Calibration of a Shear-Stress Sensor Using Stokes-Layer Excitation Introduction. *AIAA Journal*, vol. 39, no. 5, 2001, pp. 819–823.

32. Melling, A.; and Whitelaw, J. H.: Turbulent flow in a rectangular duct. *J. Fluid Mech*, vol. 78, no. 2, 1976, pp. 289–315.

33. Doherty, J.; Ngan, P.; Monty, J.; and Chong, M.: The development of turbulent pipe flow. *16th Australasian Fluid Mechanics Conference*, 2007, pp. 266–270.

34. Anselmet, F.; Ternat, F.; Amielh, M.; Boiron, O.; Boyer, P.; and Pietri, L.: Axial development of the mean flow in the entrance region of turbulent pipe and duct flows. *Comptes Rendus Mécanique*, vol. 337, no. 8, 2009, pp. 573–584.

35. Gessner, F.; Po, J.; and Emery, A.: Measurements of developing turbulent flow in a square duct. *Turbulent Shear Flows I*, Springer Verlag, Berlin, 1979, pp. 119–136.

36. Barlow, J. B.; Rae, W. H.; and Pope, A.: *Low speed wind tunnel testing*. John Wiley, New York, NY, third ed., 1999.

37. Pressure Systems Inc.: NetScanner 9116 Product Data. 2009.

38. Pope, S. B.: *Turbulent Flows*. Cambridge University Press, Cambridge, 2000.

39. Comte-Bellot, G.: Turbulent flow between two parallel walls. Ph.D. Thesis, University of Grenoble, 1963.

40. ASTM E1050-12: Standard test method for impedance and absorption of acoustical materials using a tube, two microphones and a digital frequency analysis system. *ASTM International*, 2012.

41. Motsinger, R. E.; and Kraft, R.: Design and Performance of Duct Acoustic Treatment. *Aeroacoustics of Flight Vehicles: Theory and Practice Volume 1*, H. H. Hubbard, ed., Acoustical Society of America, Woodbury, NY, 14, 1995, pp. 165–205.

42. Parrott, T. L.; and Jones, M. G.: Uncertainty in Acoustic Liner Impedance Measurement and Prediction. *Assessment of NASA's Aircraft Noise Prediction Capability TP 2012-215653*, M. Dahl, ed., NASA, Cleveland, OH, 6, 2012, pp. 157–204.

43. Kumaresan, R.; and Tufts, D.: Estimating the parameters of exponentially damped sinusoids and pole-zero modeling in noise. *IEEE Transactions on Acoustics, Speech and Signal Processing*, vol. 30, no. 6, 1982, pp. 833–840.

44. Rice, E.: A model for the acoustic impedance of a perforated plate liner with multiple frequency excitation. *NASA TM X-67950*, 1971.

45. Wieneke, B.: PIV uncertainty quantification from correlation statistics. *Measurement Science and Technology*, vol. 26, no. 7, 2015, pp. 1–10.

46. Hutchins, N.; Nickels, T. B.; Marusic, I.; and Chong, M. S.: Hot-wire spatial resolution issues in wall-bounded turbulence. *Journal of Fluid Mechanics*, vol. 635, sep 2009, p. 103.

47. Panton, R. L.: Scaling turbulent wall layers. *Journal of Fluids Engineering*, vol. 112, 1990, pp. 425–432.

48. Zagarola, M. V.; and Smits, A. J.: Mean-flow scaling of turbulent pipe flow. *Journal of Fluid Mechanics*, vol. 373, 1998, pp. 33–79.

49. Stevenson, T. N.: A law of the wall for turbulent boundary layers with suction or injection. 166, The College of Aeronautics, Cranfield, 1963.

50. Park, S. H.; Lee, I.; and Sung, H. J.: Effect of local forcing on a turbulent boundary layer. *Experiments in Fluids*, vol. 31, 2001, pp. 384–393.

51. Jabbal, M.; and Zhong, S.: Particle image velocimetry measurements of the interaction of synthetic jets with a zero-pressure gradient laminar boundary layer. *Physics of Fluids*, vol. 22, no. 6, 2010, pp. 1–17.

52. Joung, Y.; Choi, S.-U.; and Choi, J.-I.: Direct numerical simulation of turbulent flow in a square duct: analysis of secondary flows. *Journal of Engineering Mechanics*, vol. 133, no. 2, 2007, pp. 213–221.

53. Gessner, F. B.: Turbulence and mean-flow characteristics of fully-developed flow in rectangular channels. Ph.D. Thesis, Purdue University, 1964.

54. Coleman, H. W.; and Steele, W. G.: *Experimentation, Validation, and Uncertainty Analysis for Engineers*. John Wiley, third edition ed., 2009.

Appendix A

Monte Carlo Simulation

Monte Carlo simulations were performed in order to compute coverage factors for the Darcy friction factor, as well as the impedance using the SMM and KT-Prony methods. Only the process for the wall shear stress and friction factor is detailed here, as the methodology is the same for the impedance eduction Monte Carlo simulations.

Figure A1 shows the overall data flow and procedure. First, the relevant data is collected, and both bias and random errors are tabulated to use as inputs to the simulation. Next, the variables are checked for any correlation that may alter the bounds of the coverage factor if not included. It was found that only the static pressures measured in the test section were correlated to each other, and that the tunnel parameters had a correlation coefficient less than 0.1. Therefore, only the correlation effects between the static pressures are included in the simulation. Figure A2 shows the relationship between data taken at adjacent ports, P_3 and P_5. The data is plotted along with the simulated population to ensure that the expected distribution is achieved. The correlation coefficient calculated using the experimental data is 0.91, and is used to fit the mean trend between the two distributions. It should be noted that although only two ports are shown in the plot for the sake of visualization, all of the ports are well correlated. The `mvnrnd` function in MATLAB is used to produce the multivariate Gaussian distribution.

Following the generation of the sample populations, each realization is used to calculate a distribution of the output variables, in this case, the wall shear stress and the Darcy friction factor. The number of realizations required to produce a converged set is established by setting a threshold of acceptable variation and checking the running values against the final value of the converging quantity. Figures A3 and A4 show the convergence of mean wall shear stress and friction factor to $\pm 1\%$ within 500–1000 samples. However, the standard deviation of the output variables, shown in Figures A5 and A6 takes much longer to converge. Setting the number of samples to 10000 produces the desired range of convergence for all of the relevant statistics.

In order to justify the claim that no higher order statistics are necessary, sample probability density functions (pdfs) are shown in Figures A7 and A8. The pdfs show excellent agreement with the fitted Gaussian profiles, and a chi-squared distribution test fails to reject the hypothesis that the distributions are normal at the 5% significance level. This result is to be expected due to the central limit theorem and the absence of any strong nonlinearities which might skew the distribution [54].

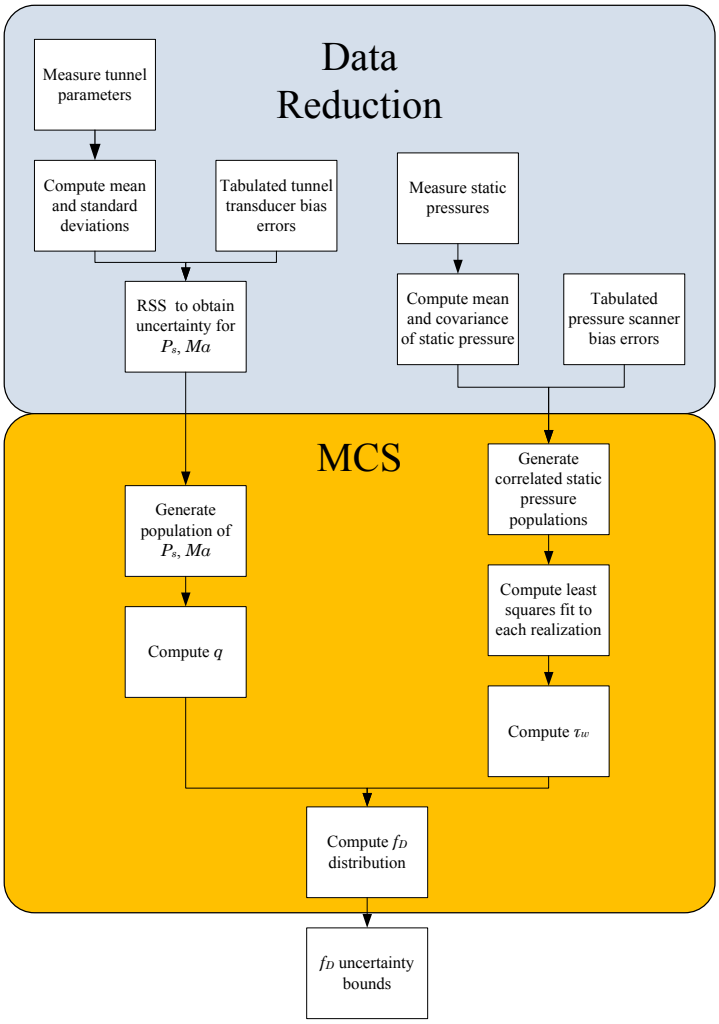

Figure A1. The figure above outlines the general procedure used for performing the Monte-Carlo simulation using the measured variables as inputs.

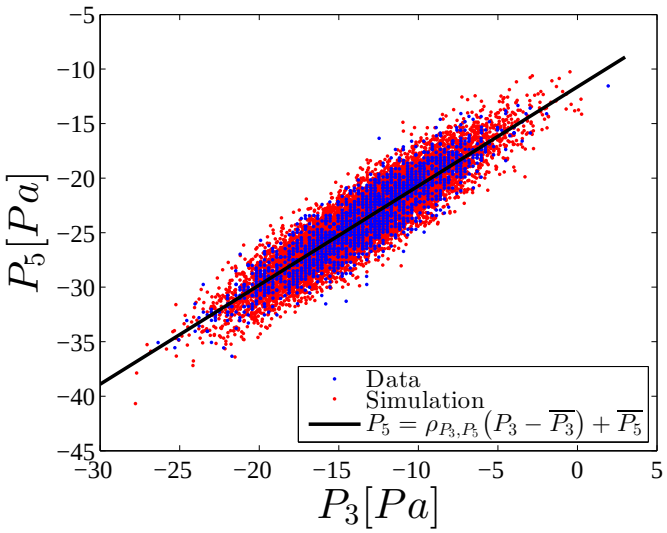

Figure A2. The figure above shows the correlation between pressure samples taken at ports P_3 and P_5, along with the simulated pressure distribution, mean correlation relationship between the two pressure populations.

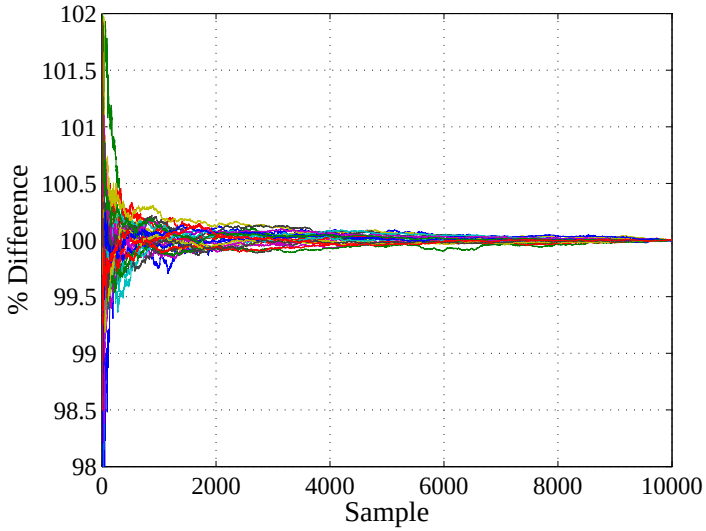

Figure A3. A plot showing the convergence of the mean shear stress determined using the MCS.

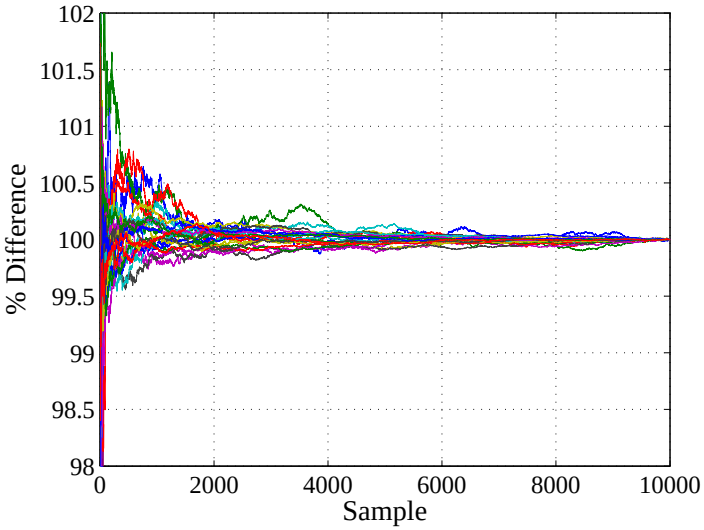

Figure A4. A plot showing the convergence of the friction factor determined using the MCS.

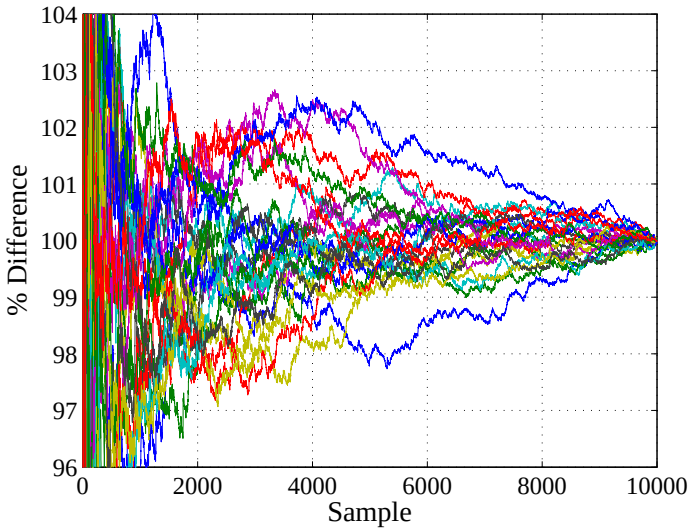

Figure A5. A plot showing the convergence of the shear stress standard deviation determined using the MCS.

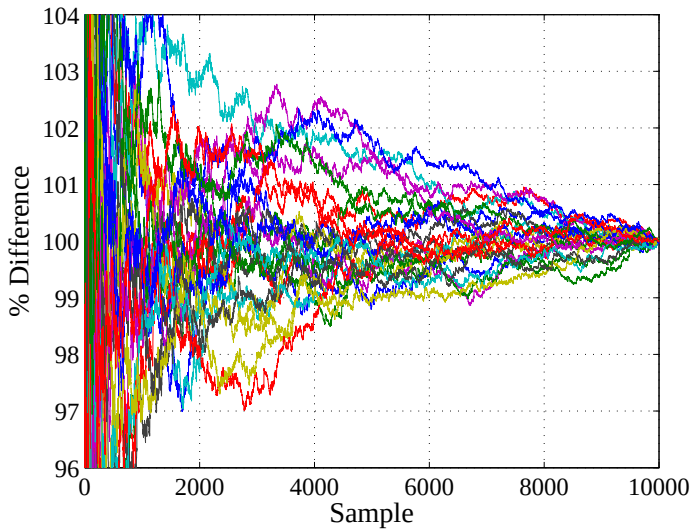

Figure A6. A plot showing the convergence of the friction factor standard deviation determined using the MCS.

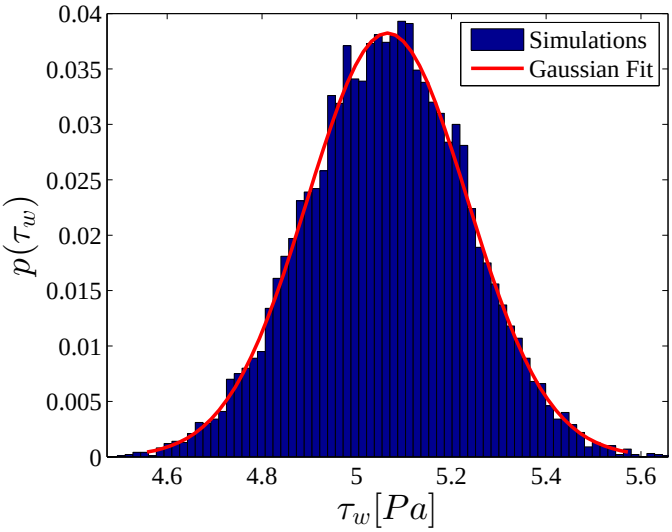

Figure A7. A plot showing the pdf of the shear stress determined using the MCS.

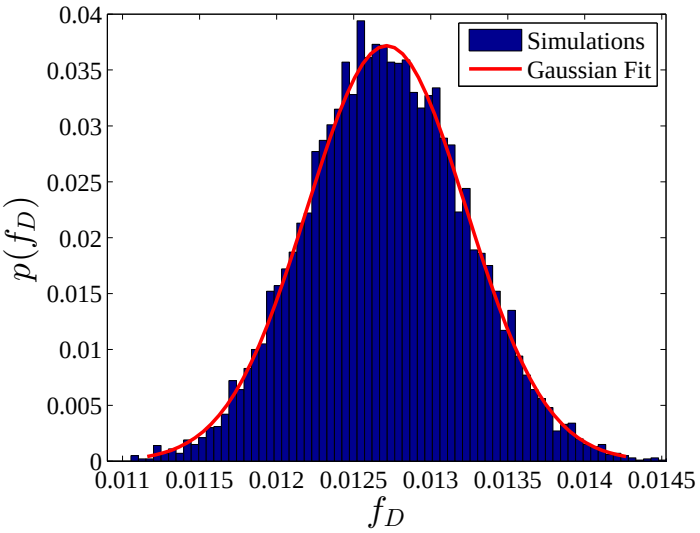

Figure A8. A plot showing the pdf of the friction factor determined using the MCS.

Appendix B

Pitot Sensitivity Analysis

In order to estimate the uncertainty in some derived quantities, a sensitivity analysis was carried out. This consisted of gathering the uncertainties of the measured pressures and temperature and propagating those uncertainties through the necessary equations to determine the uncertainty in the desired output variables. Error sources can come from either systematic deviations or random errors. The random error for each of the variables is determined through the sample standard deviation. Systematic or bias errors come from calibration errors or deviations of a transducer from linearity. Table B1 shows the uncertainties of each transducer. The pitot geometry bias error stems from flow disturbances at the pressure ports due to placement of the stem, as well as pressure recovery over the hemispherical nose. This appendix contains the sensitivity analysis performed for the both the bulk and centerline Mach numbers, the Reynolds number, velocity ratio, and dynamic pressure.

Table B1. Transducer Bias Errors.

Transducer	Uncertainty
Pressure Scanner (10" H_2O Range)	$\pm 2.5\,[Pa]$
Pressure Scanner (1 psi Range)	$\pm 6.9\,[Pa]$
Stagnation Pressure	$\pm 25.9\,[Pa]$
Static Pressure	$\pm 27.6\,[Pa]$
Atmospheric Pressure	$\pm 25.3\,[Pa]$
Stagnation Temperature	$\pm 0.34\,[K]$
Pitot Geometry	$+0.01q\,[Pa]$

B.1 Mach Number Uncertainty

This section outlines the procedure used to calculate the uncertainty in the measured pitot Mach number as well as the nozzle Mach number. It is useful to define the pressure ratio,

$$P_r = \frac{P_s}{P_0},$$

as an intermediate variable to keep the equations for the sensitivities compact. The Mach number in terms of the pressure ratio is

$$M = \sqrt{\frac{2}{\gamma - 1}\left(P_r^{\frac{1-\gamma}{\gamma}} - 1\right)}. \tag{B1}$$

The sensitivity of the Mach number to the pressure ratio is

$$\frac{\partial M}{\partial P_r} = \frac{-1}{\gamma} P_r^{\frac{1-2\gamma}{\gamma}} \left[\frac{2}{\gamma - 1}\left(P_r^{\frac{1-\gamma}{\gamma}} - 1\right)\right]^{-\frac{1}{2}}. \tag{B2}$$

The sensitivities of the pressure ratio to the static pressure and stagnation pressure are needed to complete the chain rule for determining the Mach number uncertainty in terms of measured quantities. These are

$$\frac{\partial P_r}{\partial P_s} = \frac{1}{P_0} \tag{B3a}$$

and

$$\frac{\partial P_r}{\partial P_0} = \frac{-P_s}{P_0^2}. \tag{B3b}$$

The compressible form of the dynamic pressure is

$$q = \frac{\gamma}{2} P_s M^2, \tag{B4}$$

and the dependence of the Mach number on the dynamic pressure is

$$\frac{\partial M}{\partial q} = \frac{1}{2}\sqrt{\frac{1}{2\gamma P_s q}}. \tag{B5}$$

This is used to account for the bias error in the Mach number due to bias in the dynamic pressure due to the geometry of the pitot tube [36].

Now that all of the sensitivities have been determined to link the measured values with the Mach number, the uncertainties of each of the individual input variables can be addressed. The uncertainty in the stagnation pressure is

$$\mathcal{U}_{P_0} = \pm\sqrt{B_{P_0}^2 + \left(\frac{1.96 S_{P_0}}{\sqrt{N}}\right)^2}, \tag{B6}$$

where B_{P_0} is the appropriate bias error for the pressure measurement, S_{P_0} is the standard deviation of the stagnation pressure, and N is the number of samples. The factor of 1.96 accounts for the 95% confidence interval of a Gaussian population. Similarly, the uncertainty in the static pressure is

$$\mathcal{U}_{P_s} = \pm\sqrt{B_{P_s}^2 + \left(\frac{1.96 S_{P_s}}{\sqrt{N}}\right)^2}. \tag{B7}$$

Finally, the uncertainty in the Mach number measured by the pitot tube is

$$\mathcal{U}_M = \pm\sqrt{\left(\frac{\partial M}{\partial q} B_q^2 + \left(\frac{\partial M}{\partial P_0}\mathcal{U}_{P_0}\right)^2 + \left(\frac{\partial M}{\partial P_s}\mathcal{U}_{P_s}\right)^2}, \tag{B8}$$

For the calculation of the nozzle Mach number, there is assumed to be no geometry related bias error as there is for the centerline Mach number. The stagnation pressure is measured in the stagnation chamber, and the static pressure is measured by the analog average of four tubulations placed at the throat of the nozzle. This essentially is an assumption that the static pressure ports are free of burrs, which

might disturb the flow and affect the pressure measurement. Without this bias error, the uncertainty is

$$\mathcal{U}_M = \pm\sqrt{\left(\frac{\partial M}{\partial P_0}\mathcal{U}_{P_0}\right)^2 + \left(\frac{\partial M}{\partial P_s}\mathcal{U}_{P_s}\right)^2}. \tag{B9}$$

In both the nozzle and centerline Mach numbers, the uncertainty due to bias errors is at least an order of magnitude larger than the uncertainty due to random errors. The contribution of error to the nozzle Mach number is evenly split between the static and stagnation pressures. For the centerline Mach number, the static and stagnation pressure uncertainties are dominant at low Mach numbers, and the dynamic pressure bias is larger at high Mach numbers, with the error being approximately on the same order at $M = 0.17$.

B.2 Reynolds Number Uncertainty

The Reynolds number based on the bulk Mach number can be written as

$$Re_b = \frac{\gamma P_s h M}{c\mu}. \tag{B10}$$

The uncertainty in the static pressure and Mach number have been presented in the previous section. The speed of sound is

$$c = \sqrt{\gamma R T_s}, \tag{B11}$$

and the sensitivity of the speed of sound to the static temperature is

$$\frac{\partial c}{\partial T_s} = \sqrt{\frac{\gamma R}{T_s}}. \tag{B12}$$

The static temperature is a function of the stagnation temperature and Mach number by the isentropic relationship

$$T_s = T_0\left(1 + \frac{\gamma - 1}{2}M^2\right)^{-1}. \tag{B13}$$

The sensitivities of the static pressure to the stagnation temperature and Mach number are

$$\frac{\partial T_s}{\partial T_0} = \frac{1}{1 + \frac{\gamma-1}{2}M^2} \tag{B14a}$$

and

$$\frac{\partial T_s}{\partial M} = -T_0\frac{(\gamma - 1)M}{\left(1 + \frac{\gamma-1}{2}M^2\right)^2}. \tag{B14b}$$

Again, the uncertainty in the stagnation temperature can be calculated from

$$\mathcal{U}_{T_0} = \pm\sqrt{B_{T_0}^2 + \left(\frac{1.96 S_{T_0}}{\sqrt{N}}\right)^2}. \tag{B15}$$

Likewise, the uncertainty in the speed of sound is

$$\mathcal{U}_c = \pm\sqrt{\left(\frac{\partial c}{\partial T_0}\mathcal{U}_{T_0}\right)^2 + \left(\frac{\partial c}{\partial M}\mathcal{U}_M\right)^2}. \tag{B16}$$

Turning our attention to the dynamic viscosity, the local value can be determined through Sutherland's equation

$$\mu = \mu_r\left(\frac{T_s}{T_r}\right)^{\frac{3}{2}}\frac{T_r + S}{T_s + S} \tag{B17}$$

where the reference temperature, $T_r = 273.15\,K$, viscosity, $\mu_r = 1.716 \times 10^{-5}\,\frac{kg}{m \cdot s}$, and Sutherland's constant $S = 110.4\,K$. The sensitivity to static temperature is

$$\frac{\partial \mu}{\partial T_s} = \mu_r\left(\frac{T_s}{T_r}\right)^{\frac{3}{2}}\frac{T_r + S}{T_s + S}\left[\frac{3}{2T_s} + \frac{1}{T_s + S}\right] \tag{B18}$$

The uncertainty in the Reynolds number is

$$\mathcal{U}_{Re} = \pm\sqrt{\left(\frac{\partial Re}{\partial P_s}\mathcal{U}_{P_s}\right)^2 + \left(\frac{\partial Re}{\partial M}\mathcal{U}_M\right)^2 + \left(\frac{\partial Re}{\partial c}\mathcal{U}_c\right)^2 + \left(\frac{\partial Re}{\partial \mu}\mathcal{U}_\mu\right)^2}. \tag{B19}$$

The main source of uncertainty enters through the sensitivity to the Mach number. This in turn ties back to the bias errors in the stagnation pressure and static pressure.

B.3 Ratio of Velocities

The ratio of centerline to bulk velocity is a parameter used when comparing the flow in the square duct to that of a channel flow. By definition it is

$$U_r = \frac{U_c}{U_b}. \tag{B20}$$

The velocity ratio is plotted for the incompressible and compressible cases. In the incompressible case, the centerline velocity for incompressible flow is

$$U_c = \sqrt{\frac{2\Delta p}{\rho_0}}. \tag{B21}$$

The sensitivities of the centerline velocity to dynamic pressure and stagnation density are

$$\frac{\partial U_c}{\partial \Delta p} = \frac{1}{2}\sqrt{\frac{2}{\rho_0 \Delta p}} \tag{B22a}$$

and

$$\frac{\partial U_c}{\partial \rho_0} = -\frac{1}{2}\sqrt{\frac{2\Delta p}{\rho_0^3}}. \tag{B22b}$$

The uncertainty in the dynamic pressure is

$$\mathcal{U}_{\Delta p} = \pm\sqrt{B_{\Delta p}^2 + \left(\frac{1.96 S_{\Delta p}}{\sqrt{N}}\right)^2}, \tag{B23}$$

where $B_{\Delta p}$ is the systematic error in the pressure drop, which is twice the value of the scanner being used for a given Mach number. The stagnation density is calculated from the ideal gas law

$$\rho_0 = \frac{P_0}{RT_0}. \tag{B24}$$

This leads to sensitivities of the stagnation density to the stagnation pressure and temperature,

$$\frac{\partial \rho_0}{\partial P_0} = \frac{1}{RT_0} \tag{B25a}$$

and

$$\frac{\partial \rho_0}{\partial T_0} = -\frac{P_0}{RT_0^2} \tag{B25b}$$

The uncertainty then, in the centerline velocity is

$$\mathcal{U}_{U_c} = \pm\sqrt{\left(\frac{\partial U_c}{\partial \Delta p}\mathcal{U}_{\Delta p}\right)^2 + \left(\frac{\partial U_c}{\partial \rho_0}\mathcal{U}_{\rho_0}\right)^2}. \tag{B26}$$

The bulk velocity is calculated from the definition of the Mach number

$$U_b = M_b c. \tag{B27}$$

As the elemental uncertainties of the Mach number and speed of sound have previously been quantified, the uncertainty in the bulk velocity is

$$\mathcal{U}_{U_b} = \pm\sqrt{\left(\frac{\partial U_b}{\partial M}\mathcal{U}_M\right)^2 + \left(\frac{\partial U_b}{\partial c}\mathcal{U}_c\right)^2}. \tag{B28}$$

Finally, the uncertainty in the velocity ratio is

$$\mathcal{U}_{U_r} = \pm\sqrt{\left(\frac{\partial U_r}{\partial U_b}\mathcal{U}_{U_b}\right)^2 + \left(\frac{\partial U_r}{\partial U_c}\mathcal{U}_{U_c}\right)^2}. \tag{B29}$$

In the compressible case, the centerline velocity is calculated from the definition of the Mach number as well, and the uncertainty analysis is identical to that of the bulk velocity. The error in determining the ratio of velocities is, unsurprisingly, dominated by the bias uncertainty in the nozzle Mach number. For the compressible case, the relative uncertainty between the centerline and nozzle velocity increases so that by the highest Mach number they are of equal magnitude. For the incompressible case, the same trend is present but the centerline velocity uncertainty is still only a third as large as the nozzle velocity uncertainty. Each of the measured velocities is in turn, dominated by their constituent pressure biases. The exception to this is in the incompressible case, where the random error in computing the pressure drop is sporadically on the same order as the bias from the pressure scanner.

B.4 Dynamic Pressure Uncertainty

The last quantity of interest is the uncertainty in the dynamic pressure, which is used in normalizing the wall shear stress. The sensitivities of the dynamic pressure are

$$\frac{\partial q}{\partial P_s} = \frac{\gamma}{2} M^2 \tag{B30a}$$

and

$$\frac{\partial q}{\partial M} = \gamma P_s M. \tag{B30b}$$

The uncertainty in the dynamic pressure is

$$\mathcal{U}_q = \pm \sqrt{\left(\frac{\partial q}{\partial M}\mathcal{U}_M\right)^2 + \left(\frac{\partial q}{\partial P_s}\mathcal{U}_{P_s}\right)^2}. \tag{B31}$$

As in all of the other cases, the uncertainty is dominated by the Mach number bias error.

Appendix C

Additional Plots

This appendix contains ancillary plots related to the work done within the main body of the report. Correlation plots for two PIV cases are shown first, followed by the raw voltage output time history for all of the CWSSS tests, and conclude with some plots of the friction factor of the L1 liner.

C.1 Hard Wall and Resonance Correlation Plots

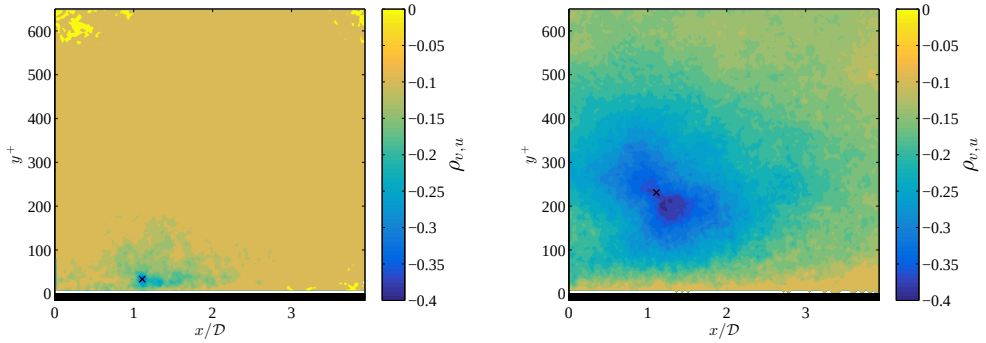

Figure C1. A comparison of $\rho_{v,u}$ at the near-wall and log region points are shown for the hard wall case.

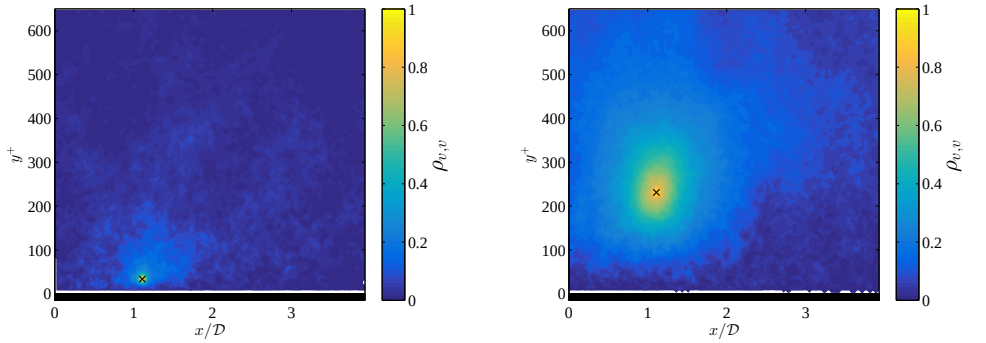

Figure C2. A comparison of $\rho_{v,v}$ at the near-wall and log region points are shown for the hard wall case.

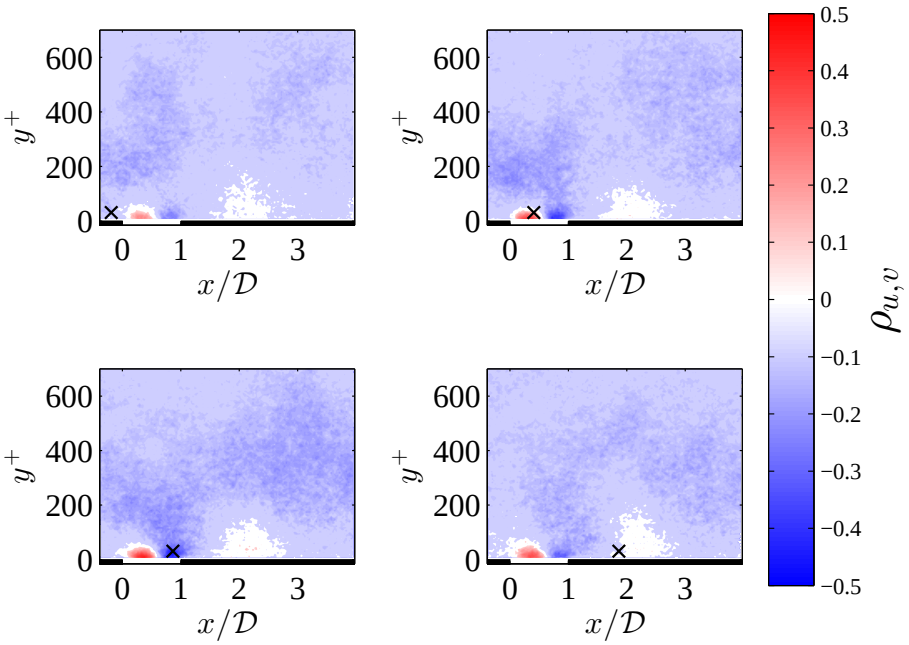

Figure C3. The correlation coefficient $\rho_{u,v}$ is shown for the four near-wall locations over the liner with acoustic forcing at the resonant frequency are shown for the phase of 0°.

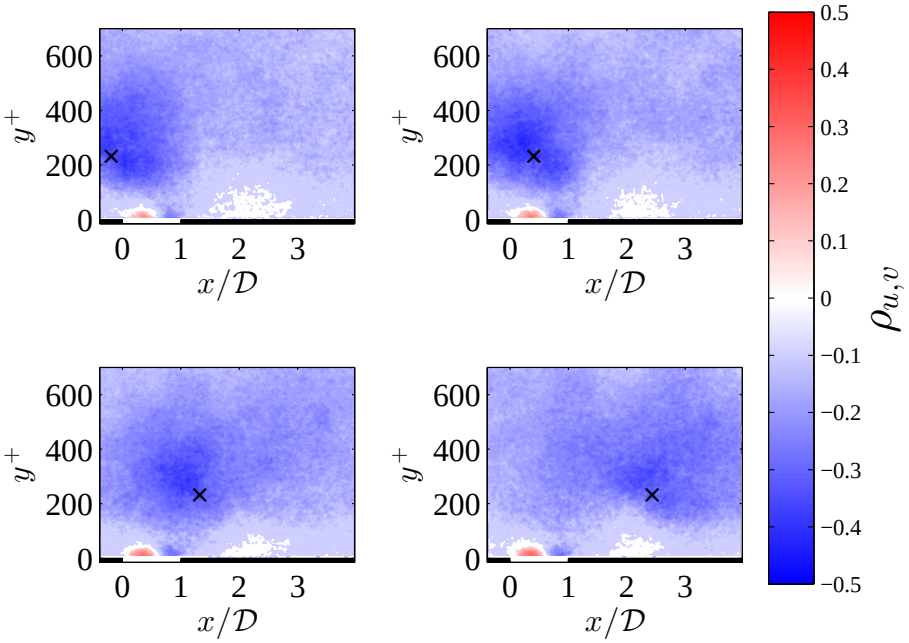

Figure C4. The correlation coefficient $\rho_{u,v}$ is shown for the four locations in the log region over the liner with acoustic forcing at the resonant frequency are shown for the phase of 0°.

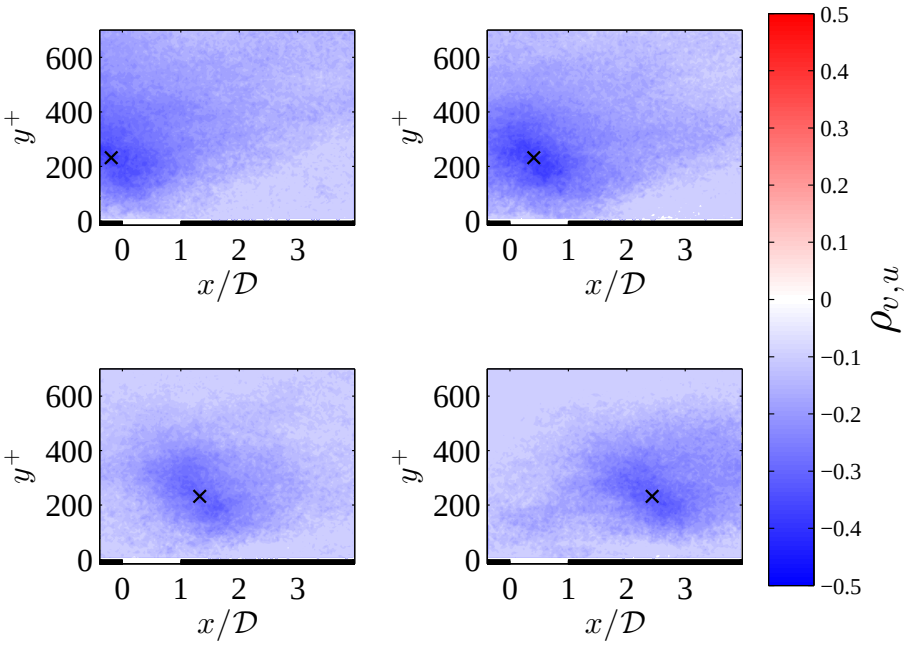

Figure C5. The correlation coefficient $\rho_{v,u}$ is shown for the four locations in the log region over the liner with acoustic forcing at the resonant frequency are shown for the phase of 0°.

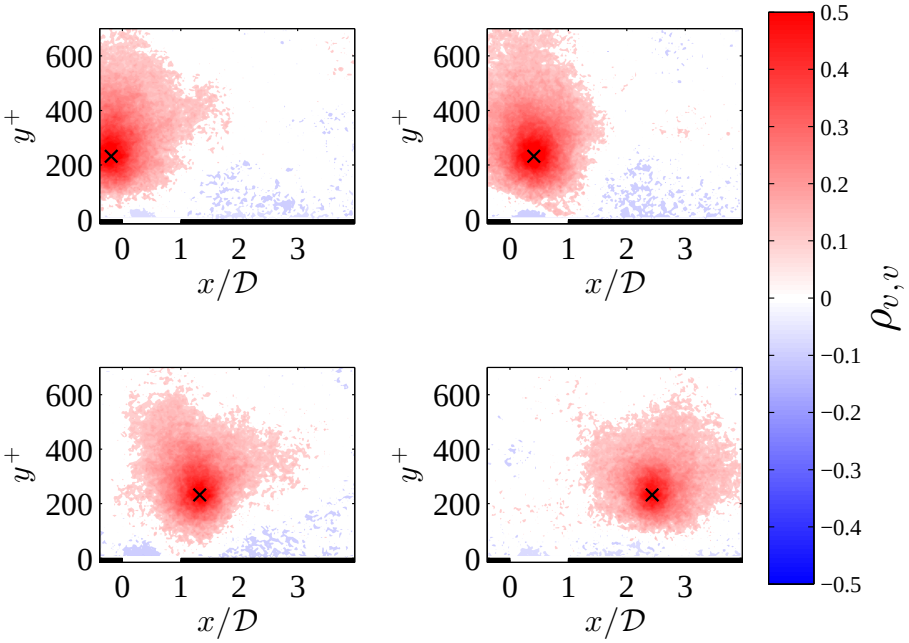

Figure C6. The correlation coefficient $\rho_{v,u}$ is shown for the four locations in the log region over the liner with acoustic forcing at the resonant frequency are shown for the phase of 0°.

C.2 HW CWSSS Voltage Plots

Figures C7–C12 show the time trace of the dc voltage measured using the CWSSS for several flow conditions. The dc voltage differential is calculated using the mean test condition voltage, and the average of the mean no flow voltages prior to and after each test. In Figure C11, there is evidence of a shift in the voltage at no flow, to which the flow condition is referenced, e.g. Test 2. As mentioned previously, there is typically one more likely reference point which is used to calculate the differential. In the case of Test 2 for $M_b = 0.26$, this would be the no flow voltage obtained after the test.

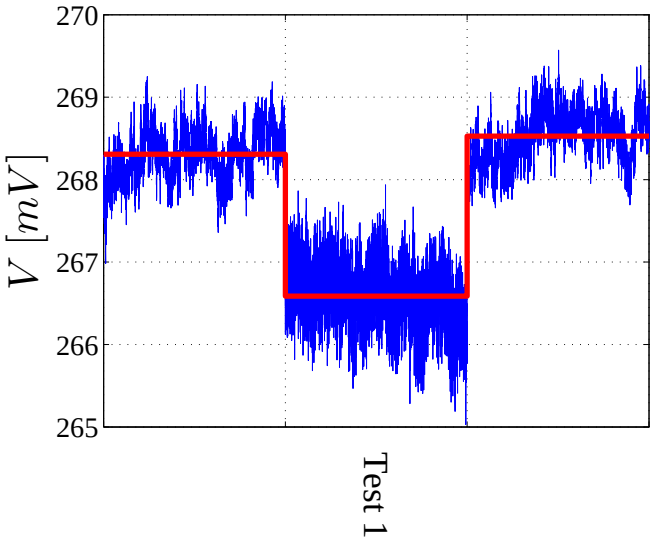

Figure C7. The dc voltage measured with the CWSSS over a hard wall at $Ma_b = 0.100$ is plotted for the number of tests taken. The high voltage corresponds to the no flow condition while the lower voltage corresponds to the test condition. The mean voltage is presented as the red line, while the raw data is blue.

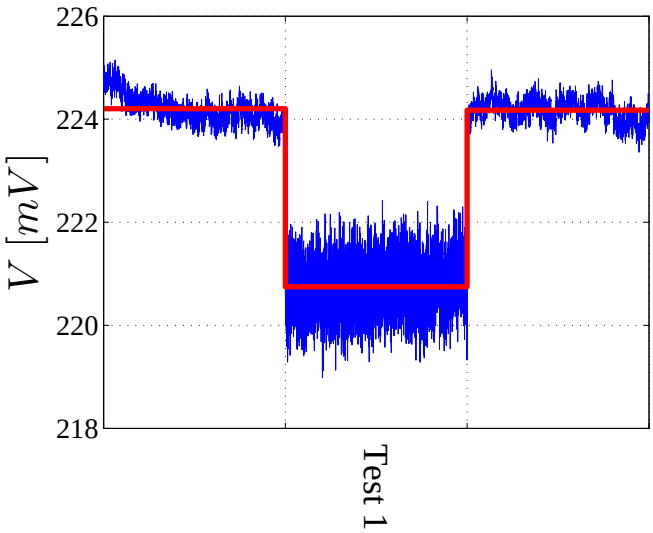

Figure C8. The dc voltage measured with the CWSSS over a hard wall at $M_b = 0.133$ is plotted for the number of tests taken. The high voltage corresponds to the no flow condition while the lower voltage corresponds to the test condition. The mean voltage is presented as the red line, while the raw data is blue.

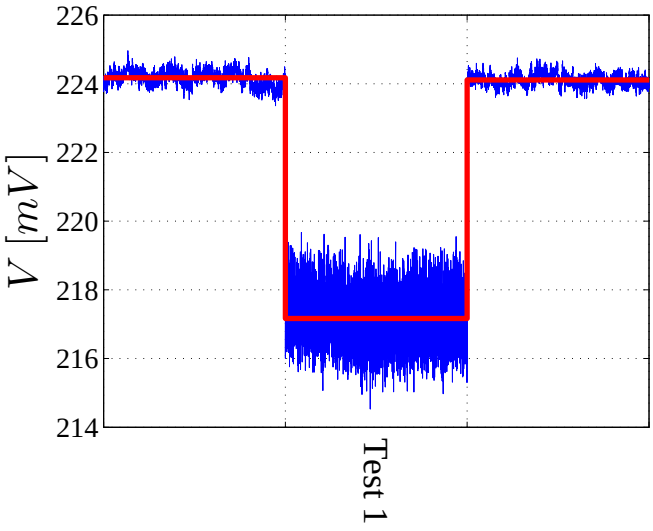

Figure C9. The dc voltage measured with the CWSSS over a hard wall at $M_b = 0.176$ is plotted for the number of tests taken. The high voltage corresponds to the no flow condition while the lower voltage corresponds to the test condition. The mean voltage is presented as the red line, while the raw data is blue.

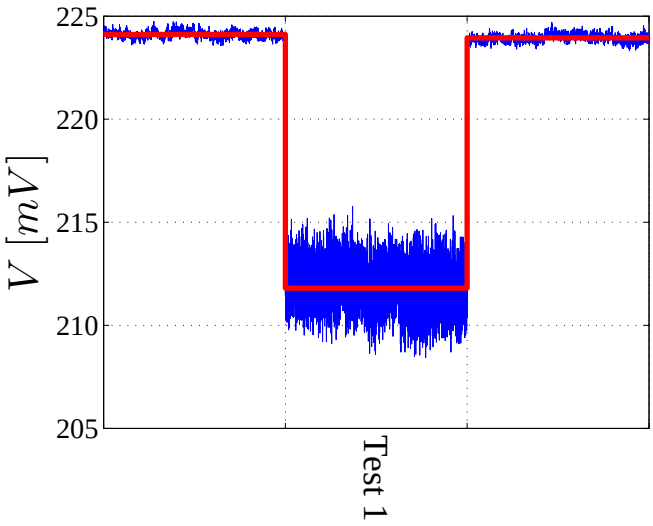

Figure C10. The dc voltage measured with the CWSSS over a hard wall at $M_b = 0.220$ is plotted for the number of tests taken. The high voltage corresponds to the no flow condition while the lower voltage corresponds to the test condition. The mean voltage is presented as the red line, while the raw data is blue.

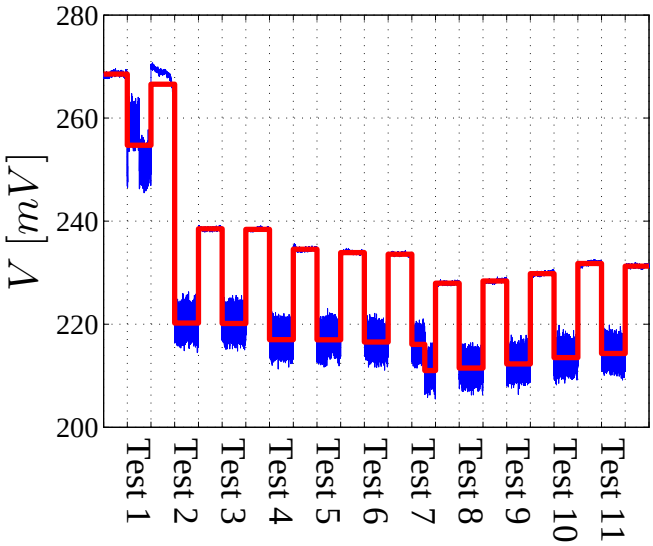

Figure C11. The dc voltage measured with the CWSSS over a hard wall is at $M_b = 0.260$ plotted for the number of tests taken. The high voltage corresponds to the no flow condition while the lower voltage corresponds to the test condition. The mean voltage is presented as the red line, while the raw data is blue.

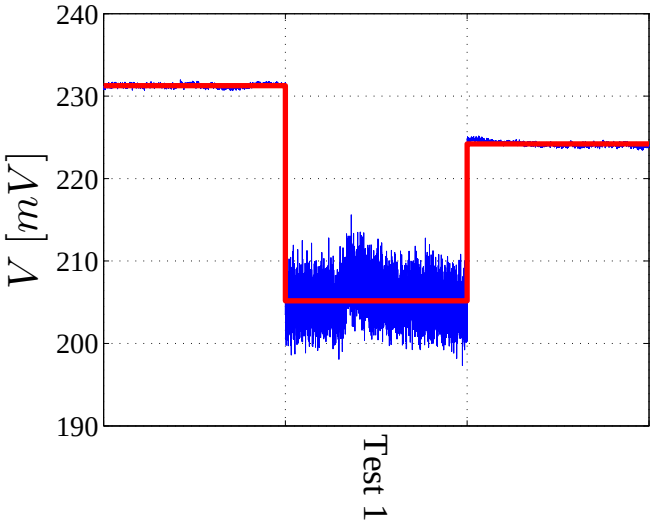

Figure C12. The dc voltage measured with the CWSSS over a hard wall at $M_b = 0.300$ is plotted for the number of tests taken. The high voltage corresponds to the no flow condition while the lower voltage corresponds to the test condition. The mean voltage is presented as the red line, while the raw data is blue.

C.3 L2 CWSSS Voltage Plots

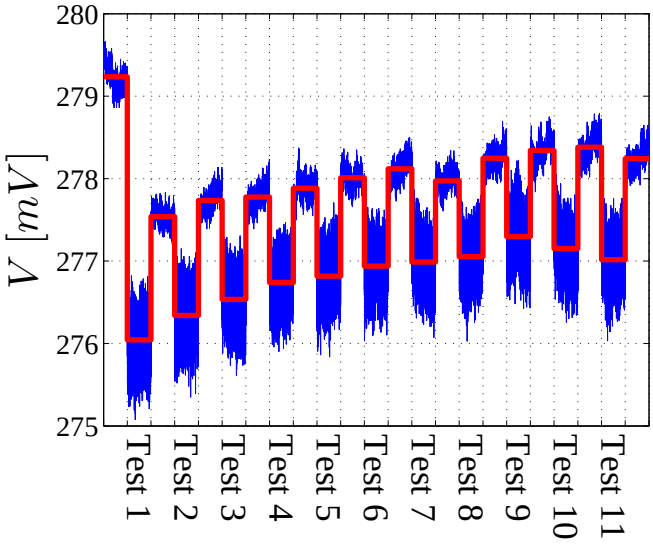

Figure C13. The dc voltage measured with the CWSSS over the L2 liner at $M_b = 0.091$ with no acoustic excitation is plotted for the number of tests taken. The high voltage corresponds to the no flow condition while the lower voltage corresponds to the test condition. The mean voltage is presented as the red line, while the raw data is blue.

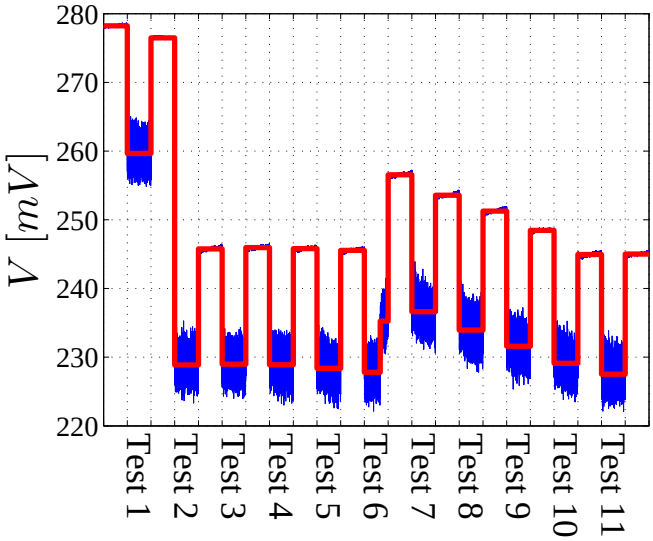

Figure C14. The dc voltage measured with the CWSSS over the L2 liner at $M_b = 0.26$ with no acoustic excitation is plotted for the number of tests taken. The high voltage corresponds to the no flow condition while the lower voltage corresponds to the test condition. The mean voltage is presented as the red line, while the raw data is blue.

C.4 L1 Friction Factor Plots

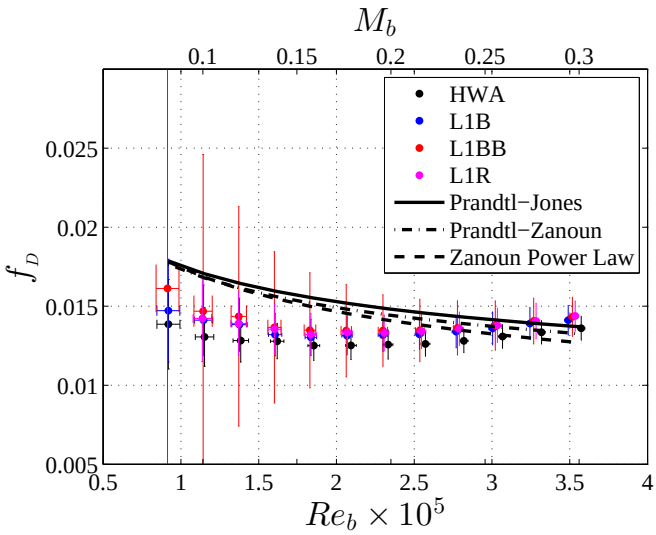

Figure C15. The Darcy friction factor is presented for all the different cases taken over liner L1 as a function of the bulk Reynolds number. The values for the L1 cases are the average of three hard walls and a liner.

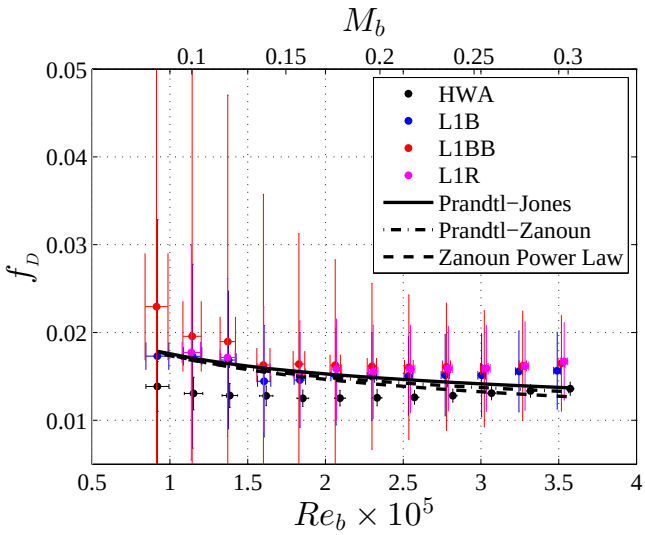

Figure C16. The Darcy friction factor is presented for all the different cases taken over liner L1 as a function of the bulk Reynolds number. The values for the L1 cases compensated so that that they are the best estimate of the friction factor of the liner.

REPORT DOCUMENTATION PAGE	Form Approved OMB No. 0704–0188

1. REPORT DATE *(DD-MM-YYYY)*	2. REPORT TYPE	3. DATES COVERED *(From - To)*
01-07-2017	Contractor Report	

4. TITLE AND SUBTITLE
Diagnostic Techniques to Elucidate the Aerodynamic Performance of Acoustic Liners

5a. CONTRACT NUMBER

5b. GRANT NUMBER
NNH10ZEA001N, Topic A.2.8

5c. PROGRAM ELEMENT NUMBER

6. AUTHOR(S)
June, Jason; Bertolucci, Brandon; Ukeiley, Lawrence; Cattafesta, Louis N.; Sheplak, Mark

5d. PROJECT NUMBER

5e. TASK NUMBER

5f. WORK UNIT NUMBER
081876.02.07.50.03.01

7. PERFORMING ORGANIZATION NAME(S) AND ADDRESS(ES)
NASA Langley Research Center
Hampton, Virginia 23681-2199

8. PERFORMING ORGANIZATION REPORT NUMBER
L–20807

9. SPONSORING/MONITORING AGENCY NAME(S) AND ADDRESS(ES)
National Aeronautics and Space Administration
Washington, DC 20546-0001

10. SPONSOR/MONITOR'S ACRONYM(S)
NASA

11. SPONSOR/MONITOR'S REPORT NUMBER(S)
NASA/CR–2017–219583

12. DISTRIBUTION/AVAILABILITY STATEMENT
Unclassified-Unlimited
Subject Category 71
Availability: NASA STI Program (757) 864-9658

13. SUPPLEMENTARY NOTES
An electronic version can be found at http://ntrs.nasa.gov.

14. ABSTRACT

In support of Topic A.2.8 of NASA NRA NNH10ZEA001N, the University of Florida (UF) has investigated the use of flow field optical diagnostic and micromachined sensor-based techniques for assessing the wall shear stress on an acoustic liner. Stereoscopic particle image velocimetry (sPIV) was used to study the velocity field over a liner in the Grazing Flow Impedance Duct (GFID). The results indicate that the use of a control volume based method to determine the wall shear stress is prone to significant error. The skin friction over the liner as measured using velocity curve fitting techniques was shown to be locally reduced behind an orifice, relative to the hard wall case in a streamwise plane centered on the orifice. The capacitive wall shear stress sensor exhibited a linear response for a range of shear stresses over a hard wall. PIV over the liner is consistent with lifting of the near wall turbulent structure as it passes over an orifice, followed by a region of low wall shear stress.

15. SUBJECT TERMS
acoustic liners, shear stress, skin friction drag, PIV

16. SECURITY CLASSIFICATION OF:			17. LIMITATION OF ABSTRACT	18. NUMBER OF PAGES	19a. NAME OF RESPONSIBLE PERSON
a. REPORT	b. ABSTRACT	c. THIS PAGE			STI Information Desk (help@sti.nasa.gov)
U	U	U	UU	124	19b. TELEPHONE NUMBER *(Include area code)* (757) 864-9658